Final Technical Report
Analysis of Digital Teleseismic Array Data Collected in South Central Siberia and Northern Mongolia, GSN SKS waves and S Waves from Lop Nor Nuclear Explosions

Paul M. Davis, Shangxing Gao and Laura Borton
Department of Earth and Space Sciences,
University of California, Los Angeles, CA90095

Contract No. F49620-94-1-0406

Sponsored by AFOSR

January 02 2001

REPORT DOCUMENTATION PAGE

AFRL-SR-BL-TR-01-

0047

1. REPORT DATE (DD-MM-YYYY)	2. REPORT TYPE	7-1-98 through 6-30-98
January 2, 2001	Final Technical Report	

4. TITLE AND SUBTITLE
AASERT-94 Analysis of Digital Teleseismic Array Data Collected

In South Central Siberia and Northern Mongolia

5a. CONTRACT NUMBER

5b. GRANT NUMBER
F49620-94-1-0406

5c. PROGRAM ELEMENT NUMBER

6. AUTHOR(S)
Dr. Paul M. Davis

5d. PROJECT NUMBER
3484/YS

5e. TASK NUMBER
3484/YS

5f. WORK UNIT NUMBER

7. PERFORMING ORGANIZATION NAME(S) AND ADDRESS(ES)

University of California, Los Angeles
Department of Earth and Space Sciences
UCLA, Los Angeles, CA 90095

8. PERFORMING ORGANIZATION REPORT NUMBER

Final Technical Report

9. SPONSORING / MONITORING AGENCY NAME(S) AND ADDRESS(ES)
AFOSR/NM
110 Duncan Avenue Room B115
Bolling AFB DC 20332-8050

10. SPONSOR/MONITOR'S ACRONYM(S)

11. SPONSOR/MONITOR'S REPORT NUMBER(S)

12. DISTRIBUTION / AVAILABILITY STATEMENT
Approved for public release, distribution unlimited

13. SUPPLEMENTARY NOTES

14. ABSTRACT
See attached

15. SUBJECT TERMS

16. SECURITY CLASSIFICATION OF: Unclassified			17. LIMITATION OF ABSTRACT	18. NUMBER OF PAGES	19a. NAME OF RESPONSIBLE PERSON Linda Lee, Manager OCGA
a. REPORT	b. ABSTRACT	c. THIS PAGE			19b. TELEPHONE NUMBER (include area code) (310) 794-0369

TABLE OF CONTENTS

ABSTRACT

Analysis of data we collected in south central Siberia and Northern Mongolia along with digital data from the Global Seismic Network have been analysed to identify effects on propagation of large scale heterogeneity in the mantle that need to be taken into account when using seismic arrays to monitor the Comprehensive Test Ban Treaty. We find that in the vicinity of the Baikal rift zone in Siberia, P and S waves exhibit anomalous delays and attenuation. S waves show clear evidence of anisotropy effects. This anomalous region that extends over several hundred km either side of he rift zone, and is presumed to extend along the 600 km of its axis, represents an attenuating and delaying mantle barrier to seismic phases. These findings can be used to infer properties of analogous tectonic regions world-wide (Basin and Range of North America, Northern Tibet, East African and Rio Grande rifts, Red Sea, Gulf of California). We have analysed all stations of the Global Seismic Network (GSN) for SKS splitting in the mantle. We compare SKS waveforms with normal mode synthetics modified by splitting by one or two layers of anisotropy in the mantle. Splitting is recognised as scattering of radial energy into tangential energy. We find that stations can be characterised by a single layer of splitting in their vicinity but for some arrivals scattering deeper in the mantle either due to a second layer of anisotropy or 3D scatterers gives anomalous tangential energy. This observation has led to development of a new method to identify deep mantle scatterers, by arrivals with anomalous tangential energy. We have examined P-S scattering from 12 Lop Nor nuclear explosions recorded at GSN stations in Asia. We have identified PcS and possible source generated S. Both show splitting effects that must be deconvolved before they can be confidently be interpreted as nuclear explosion P-S scattering. Lowering the threshold for discrimination and yield estimates of nuclear explosions requires that these effects on propagation of the generated phases are recognized, and be taken into account quantitatively.

INTRODUCTION

This report includes work performed by students supported by an AASERT award that supplemented our Contract F49620-94-1-0161. The bulk of the final report below corresponds to that of the original contract. However work completed subsequent to that submission is also included in the form of three new figures on the seismic tomography (Figure 7.1, 7.2) and receiver functions (Figure 8.1) from the Baikal rift zone region.

Most nuclear tests occur on continents. Continental geology can broadly be separated into stable shields and mobile belts. Deformation of mobile belts gives rise to orogenic zones and rift zones. Recently it has been recognized that large variations in the seismic properties of the upper mantle occur beneath the mobile belts of the continents and these need to be taken into account when using seismograms to discriminate explosions from earthquakes, to measure seismic yield and to locate events.

This report has three parts. Part one (sections 1-4) documents lateral variation in attenuation, anisotropy, and seismic velocity in a 1200x400 km area centred on the Baikal rift zone in Siberia, and the Mongolian fold belt, based on two portable array experiments we carried out with colleagues from University of Wisconsin and the Institute of the Earth's Crust, Irkutsk in the summers of 91 and 92. It includes new analyses of S-wave delays and recognition of lower mantle velocity anomalies in the data and possible slab effects in the source zone of the measured teleseisms. Part two (section 5) deals with application of normal mode synthetics to scattering in the mantle and SKS splitting and is a result of a collaboration with Prof. John Woodhouse (who has developed the synthetics code) while the PI was on sabbatical in Oxford. Part three is (section 6) reports on our (Laura Borton, AASSERT graduate student) attempts to recognise teleseismic S body waves from Lop Nor Nuclear explosions and what effects the anomalies that we have measured in the previous sections have on seismograms from nuclear explosions recorded by the GSN.

1. The Baikal Rift Zone Experiments

Analysis of the data from the Baikal rift zone experiment has revealed the distribution of attenuation and velocity anomalies beneath the rift zone which abuts the Siberian craton to the NW and the Mongolian fold belt to the SE. The attenuation analysis finds that relative t_p^* and t_s^* have a 0.2 and 5 second anomalies in the rift zone. Explosions detonated in this area would have reduced body wave amplitudes at arrays at teleseismic distances such as NORESS with a concomitant underestimate in yield. We have observed S wave splitting of on average 1 s at virtually every station, implying that significant anisotropy is present in the uppermost mantle. Though fast directions are spatially coherent in local regions there is significant variation region to region. P wave travel time delays show an unusual pattern of a central peak of about 1 sec surrounded by two troughs of about 0.5 secs resulting in anisotropic variation dependent on incidence and azimuth. We attribute the combination of low Q, anisotropy and travel

time anomalies to small scale convective upwelling beneath the rift zone. Comparison with similar experiments and the global Earth models is taken as evidence that these effects are present world-wide beneath extension zones on the continents and should be taken into account as part of any global seismic monitoring system. Our portable array spans two stations which will be used to monitor the CTBT: Talya, Siberia and Ulan Batur, Mongolia. Our characterisation of regional propagation effects in their vicinity will thus be useful for station calibration.

The data tapes from these experiments have been submitted to the IRIS data center and are available to any one who is interested in using them. The following sections introduce the Baikal rift 1991-92 experiment and briefly describes the major scientific findings obtained using the data set.

2. THE 1991 EXPERIMENT

The 1991 experiment took place between July 7 and October 5. Twenty-six seismic stations (10 PASSCAL Reftek and 16 U. Wisconsin recorders) were installed about Lake Baikal (Figure 2.1 and Table 2.1). The UCLA field trip team installed and operated the 10 Reftek stations. All the stations were equipped with 1 Hz 3-component sensors and five of the stations were co-sited with broadband (Guralp and STS2) seismometers. The seismographs synchronize internal clocks to signals from the Omega navigation system (locked to either Norway or Japan) which ensured that the timing error for most of the data was less than 20 ms.

Station Information

• **Recorders**– The 10 Reftek-72A recorders were lent to the experiment from the IRIS/PASSCAL Instrument Center at LDEO.

• **Seismometers**– 3 kinds of seismometers were deployed: 1) L4C Mark Products. These are 1 Hz 3 component sensors; 2) Four Guralp VBB CMG3 seismometers (vertical components only) with velocity response flat from 30 sec to 10 Hz at stations 01, 05, 07 and 10; 3) One Strekiesen STS-2 broad-band 3 component seismometer.

For all the 10 stations channel 1 to 3 recorded the L4C seismometers with the vertical on channel 1, north-south component on channel 2, and east-west component on channel 3. All the Guralps were recorded on channel 4. For the STS-2 station, channel 4 was recorded vertical component of STS-2, channel 5 north-south and channel 6 the east-west.

• **Station Locations**– All the station co-ordinates were determined by using

a GPS Pathfinder receiver (borrowed from UCLA's GPS group). The errors of the measurement on horizontal co-ordinates were less than 50 meters. Due to its poor accuracy on determining elevation, Russian 1:200,000 maps were used to obtain elevation instead of using the GPS measurement. Table 2.1 lists station co-ordinates and other information.

• **DAS Movement**– Some of the recorders (i.e., DAS, Reftek Data Acquisition System) were moved during the experiment for various reasons. The main reason for the movement was to replace a malfunctioning DAS with a better one so as to get some useful data from each site. Detailed information about DAS movement can be found in Table 2.2.

• **Station Performance and Problems**– Installation and servicing were carried out using a combination land vehicles, Aeroflot helicopters and boats on lake Baikal. Stations were serviced once every 20 days for 3 months. Extremely tricky roads and shortage of gasoline limited the frequency of services. Cloudy and rainy weather in the short summer of Siberia caused some recorder power failure. All of these conditions, together with the non-ideal performance of the Reftek's made a final rate of success 78% for the 10 stations.

Data Information

• **Recording Parameters**– For most of the stations we programmed a 10 samples per second (sps) continuous data stream to record teleseismic events; a 50 sps triggering stream to record high frequency local and regional events; and for those stations co-sited with broadband stations, another continuous data stream with sample rate 1 sps and 32 bits data words was programmed to record surface waves. It must be pointed out that at the beginning of the project, a shorter recording length and a higher trigger ratio for the triggered data stream were used rather than the 'standard parameters' as shown on Table 2.3. Detailed parameters can be found in the log files.

• **Data format**– Data dumped from the station disks were converted to SEGY format by using the REF2SEGY routine (Version 91.099) written by Early et al. at the PASSCAL Instrument center. The resultant SEGY format data can easily be converted to other formats such as SAC, AH, and SIERRA by using routines provided by the instrument center.

• **File name convention and data organisation**– Files were sorted into sub-directories according to the starting times and data stream that they belong to.

For instance, under sub-directory R188.02 are files in data stream 02 with starting time within Julian day 188.

File names contain the information about starting hour, minute, and second of the file, as well as DAS serial numbers and channel numbers. For instance, file 20.45.55.0369.2 under sub-directory R188.01 starts between 188:20:45:55.00 and 188:20:45:56.00 (the exact starting time of each file can be found in the header of the file); the file was recorded by DAS 369 which was station 01 (Table 2.2) on channel 2 (i.e. the north-south component).

Earthquake Information

• **Event Statistics**– According to the NOAA Earthquake Bulletin, 314 events with mb $\geq$ 5.0 occurred during July 7 and October 5, 1991 (Figure 2.2 and Table 2.4). 54 of them are larger than mb=5.5. The epicentral distances for 164 of these 314 events range from 30° to 85° to the center of the profile. As many as 111 events with mb $\geq$ 4.0 occurred in the area with delta distance less than 30°. Also recorded were 82 deep events with depth larger than 100 km.

Example of Seismograms

Figures 2.3 and 2.4 show some seismograms recorded by the profile. Figure 2.3 compares teleseisms and spectra from a Northern California event from the 4 Guralp stations. Figure 2.4 is a seismic section from a teleseismic event from 1 Hz vertical sensors, on data stream 1, i.e. the continuous stream.

Participating Personnel

Personnel involved in the installation and operation of the 10 stations include:

• **UCLA**: P.M. Davis, C. Davis, S. Gao, H.Liu, and P.D. Slack

• **Institute of Earth's Crust, Irkutsk**: Yu. A. Zorin, A. Masalski, V.M. Kozhevnikov, V.V. Mordvinova, and T. Perepelova. Academician N.A.Logatchev, director of the Institute, performed excellent leadership to the entire project.

• **Institute of Physics of the earth, Moscow**: M. Kogan, S. Panasyuk, and M. Karpechov.

• **PASSCAL Instrument Center, LDGO**: R.W.Busby

In addition, our colleagues from U.of Wisconsin, Madison led by Prof. R.P. Meyer helped in the operation of the 10 stations that were primary responsibility of the UCLA

team.

3. THE 1992 EXPERIMENT

During June 11 and October 5, 1992 the second phase of the experiment was conducted. The UCLA field trip team installed and operated the twenty-eight Reftek stations and two UW recorder stations (Figure 3.1). All the stations were equipped with 3-component short period sensors with central frequencies range from 0.5 to 2 Hz and eleven of the stations were co-sited with broadband (Guralp and STS2) seismometers.

Station Information

• **Recorders**– The Reftek-72A recorders were lent to the experiment from the IRIS/PASSCAL Equipment Center at LDEO.

• **Seismometers**– Six kinds of seismometers were deployed: 1) Thirteen L4C 1 Hz three separate component sensors. 2) Eleven S13 1HZ three separate component sensors from the IRIS/PASSCAL. 3) Four L22 2HZ three component sensors from the IRIS/PASSCAL. 4) Four Guralp VBB CMG3s (vertical components only) with velocity response flat from 30 sec to 10 Hz at stations 06, 15, 80, 84 and 87 (Table 3.1 and Figure 3.1). 5) Five Strekiesen STS-2 broad-band 3-component sensors co-occupied with short period sensors at stations 00, 01, 11, 16, 81 and 90. 6) Two UW recorders along with two HS10 1Hz sensors from UW were installed at station 08 and 10.

For all the stations with short period sensors the vertical component was on channel 1, north-south component on channel 2, and east-west component on channel3. All the Guralps were recorded on channel 4. For the STS-2 stations, channel 4 was recorded vertical component, channel 5 north-south and channel 6 east-west.

• **Station Locations**– The same method as what was used in the 1991 experiment was used to determine station locations.

• **DAS Movement**– Detailed information about DAS movement can be found in Table 3.2.

• **Station Performance and Problems**– Stations were serviced once about every 20 days for about 4 months. The rate of success is 89% for the 30 stations.

Data Information

• **Recording Parameters**– For most of the stations we programmed a 10 sps

continuous data stream to record teleseismic events; a 25 sps (for STS2 stations) or 50 sps triggering stream to record high frequency local and regional events; and for those stations co-sited with broadband stations, another continuous data stream with sample rate 1 sps and 32 bit data words was programmed to record surface waves with wide dynamic range. See Table 3.3 for the "standard parameters". Detailed parameters can be found in the log files.

- **Data format**– The same as in the 1991 experiment.
- **File name convention and data organisation**– The same as in the 1991 experiment.

Earthquake Information

- **Event Statistics**– According to the NOAA Earthquake Bulletin, 464 events with mb $\geq$ 5.0 occurred during June 11 and October 5, 1992 (Figure 3.2). 113 of them are larger than mb=5.5. The epicentral distances for 217 of these 464 events ranges from 30° to 85° to the center of the profile. As many as 191 events with mb $\geq$ 4.0 occurred in the area with delta distance less than 30°. Also recorded were 81 deep events with depth larger than 100 km.

Example of Seismograms

Figures 3.3 shows a typical record section.

Participating Personnel

Personnel involved in the installation and operation of the 30 stations include:

- **UCLA**: P.M. Davis, S. Gao, H. Liu, P.D. Slack, M. Benthien, and Don Daniels
- **Institute of Earth's Crust, Irkutsk**: Yu.A. Zorin, A. Masalski, V.M. Kozhevnikov, V.V. Mordvinova, and T. Perepelova.
- **PASSCAL Instrument Center, LDGO**: R.W. Busby.

4. DATA ANALYSIS AND RESULTS

Using the unique data set we investigated various properties of the upper mantle beneath the Baikal rift zone. These include 1). travel time residuals; 2). seismic anisotropy; and 3) seismic anelasticity. Detailed descriptions of these studies are in several published papers and manuscripts in preparation. In this section we only briefly

introduce some major results.

P-wave travel time residuals for the 1991 array

Upper mantle velocity structure is crucial for phase identification and location for regional and teleseismic events. A three dimensional downward projection inversion method is used to invert the P-wave velocity structure with constraints from deep seismic sounding data. Our results using the 1991 data set suggest that [Gao et al., 1994a] (1) the lithosphere-asthenosphere transition upwarps beneath the rift zone. (2) the upwarp has an asymmetric shape; (3) the velocity contrast is -4.9% in the asthenosphere; (4) the density contrast is -0.57%.

For the inversion we used 638 travel times from 66 teleseismic events at 22 stations (10 UCLA and 12 UW) and a polynomial up to the 6th order to represent the lithosphere-asthenosphere transition. The square root of the unmodeled variance is 0.11 seconds, which is larger than the observational error range but is presumed to arise from over-simplification of the structure as a single undulating boundary separating two regions of constant but different velocity (Figure 4.1a). The uncertainty in the depth of the boundary corresponding to the travel time misfit is $\pm$17 km. The results of the inversion are shown in Figures 4.1a and 4.1b. The depth of the interface ranges from 93 km at 300 km west of the lake, beneath the craton, 34 km beneath the lake, and back to 49 km at 200 km east of the lake, beneath the fold belt. The upwarp is asymmetrical in terms of the difference between the slopes of the western and eastern flanks. The western edge is steeper. The asymmetrical shape is consistent with the results of gravity (Figure 4.1b) and magnetotelluric studies [*Zorin*, 1971; *Popov*, 1990]. The highest point of the lithosphere-asthenosphere boundary as constrained by DSS data, reaches 34 km near the east shore of the lake, in a region of hot springs.

P- and S-wave travel time residuals from 1992 long line array

The data from the array of Figure 3.1 consist of 2128 P-wave travel times from 155 teleseismic events, corrected by subtracting theoretical arrival times [from the IASPEI 1991 Earth model, Kennett and Engdahl, 1991]. Relative residuals were formed for each event by subtracting the event's mean residual from the raw residuals and detrended to isolate velocity anomalies having wavelengths less than the array length (1260 km).

To examine the event location dependence of the relative travel time residuals, we group the events into 26 groups by azimuth (ϕ) and epicentral distance (Δ) of the

sources. This gave 517 mean travel time residuals from 26 groups which were then used in an inversion for structure.

Most of the event clusters recorded by the 1992 profile (Figure 3.1 and 4.2a) display a peak in their travel time residual curves approximately in the region -30 km $< x <$ 60 km with valleys on either side. The peaks are interpreted to arise from upwarped low-velocity structure associated with convective upwelling in the mantle. The relatively uniform distance between the valleys, and the large shift in their location as a function of incoming azimuth are interpreted to be caused by two high velocity structures located about $\pm$200 km deep.

We used an isotropic mantle model to interpret the travel time data [Gao, 1995]. The model has a curved lithosphere/asthenosphere boundary that upwarps beneath the rift and downwarps on the flanks. At the center the asthenosphere upwarps from 200 km to about 45 km. The magnitudes of the downwarps are about 120 km in the west and 40 km in the east. The velocity contrast between the lithosphere and the asthenosphere is about -2.4% (Figure 4.2b).

Figure 4.2c shows mean S-wave relative travel time residuals from 4 events from the South. A peak-to-peak anomaly of about 4 s is observed. The location of the maximum anomaly shifts about 70 km towards the NW from the center of Lake Baikal.

Seismic anisotropy and mantle flow

Flow in the mantle is thought to orient olivine crystals, resulting in anisotropy in seismic velocities [*Babuska and Cara*, 1991; *Silver and Chan*, 1991; *Vinnik et al.*, 1992; *Makeyeva et al.*, 1992] with the fast direction oriented in the direction of flow. Horizontal anisotropy has been measured on the axis of the Rio Grande rift [*Sandvol et al.*, 1992] but at present measurements have not been made on its flanks. Twenty-eight digital seismic stations and 35 analog stations were used. We find that, like the mid-ocean ridges, away from the rift axis the fast direction is horizontal and normal to the rift axis (Figure 4.3). The final results show that [Gao et al., 1994b; Gao, 1995]:

1) Beneath the rift zone and Siberian platform, most of the fast directions are northwest- southeast, i.e. orthogonal to the strike of the rift, and parallel to the extensional stress direction [*Zoback*, 1992].

2) At the transition to the fold belt in northern Mongolia, the fast direction changes to nearly east-west, i.e. parallel to the faulting and fold axis.

3) The transition takes place between stations 20 and 22, over a distance of 100 km.

4) The splitting ranges from 0.3 to 2.1 seconds which is consistent with a layer of 30 to 170 km thick characterised by 4% anisotropy.

5) Fast directions in the inner region of the Baikal rift zone are distributed in two orthogonal directions, NE and NW, approximately parallel and perpendicular to the NE strike of the rift.

As suggested in Gao et al. [1994b; 1997], the observed rift-orthogonal orientations of the anisotropy could be the result of uppermost mantle flow associated with recent tectonics. The southern results can be explained by the shear field associated with the collision of India and Asia. The northern results parallel the opening of lake Baikal. From the travel time anomalies we have inferred that the asthenosphere upwarps in a broad region extending either side of Lake Baikal, reaching the base of the crust at the lake itself. The inferred flow responsible for the upwarp is expected to anneal out ancient anisotropy. Like the oceanic case, away from the rift, the fast direction is normal to the rift axis. The rift-parallel fast directions near the rift axes can be interpreted by oriented magmatic cracks in the mantle or small scale mantle convection with rift-parallel flow. The agreement between stress estimates and corresponding crack orientations lends some weight to the suggestion that the rift-parallel fast directions are caused by oriented magmatic cracks.

Seismic P- and S-wave attenuation

We applied a common spectrum method [Halderman and Davis, 1991] to P wave and S wave data from Baikal to obtain relative t* values. The stations analysed were located along the 1280 km long profile traversing the Siberian platform, the BRZ, and the Mongolian fold belt; and in a 300 by 300 km cluster around the southern part of Lake Baikal.

We used 37 events for P-wave attenuation studies, and 5 for S-wave studies. For the calculation of both δt_p^* and δt_s^*, a time window of 12.8 s was taken starting approximately 6 s before the onset of the signal, and was tapered and Fourier transformed. A noise window of the same length was also selected before the signal window and Fourier transformed. The noise spectrum was subtracted from the signal spectrum.

The number of measurements for δt_p^* and δt_s^* is 596 and 82, respectively. The mean values at each station and their standard deviations are shown in Figure 4.4. The solid curves in Figure 4.4 are obtained by averaging the measurements in a window of 200

km in width and moving at 10 km each step. The peak to peak anomaly of 0.2 s for δt_p^*, and 0.8 s for δt_s^* is observed in the smoothed mean curves. The mean and standard deviation for δt_p^* is 0.06± 0.03 s, and for δt_s^* is 0.14±0.08 s. The δt_p^* and δt_s^* anomalies associated with the BRZ are about 6 times the standard deviation. For δt_p^*, the peak values are located in the area of ±200 km about Lake Baikal, for δt_s^*, the peak is located at -160 km (i.e., to the Northwest). Because all the events for δt_s^* were from the south and with an S-wave angle of incidence of about 35°, the northward shift may indicate that the depth of the center of the low-Q body is located at about 240 km.

Given that most of the lateral variation of shear wave velocities are found in the top 300 km of the Earth (e.g. Woodhouse and Dziewonski, 1984), we assume that the upper-most 300 km of the Earth beneath the array is responsible for the observed δt_p^* and δt_s^*. Under the assumption that the mean Q_p is 400 beneath the Siberian platform, the 0.2 s in δt_p^* results in a Q_p of 130 beneath the BRZ, and the 0.8 s in δt_s^* yields a Q_s of 60 beneath the BRZ if a Q_s of 200 is assumed beneath the Siberian platform.

Figure 4.5 shows the relation between the smoothed δt_p^* and δt_s^*. The best fitting relation is $\delta t_s^* = (3.15 \pm 0.18)\delta t_p^* - (0.11 \pm 0.01)$. The cross correlation coefficient between the two is 0.83. This ratio indicates that the observed δt^* is the result of difference in purely intrinsic attenuation rather than difference in scattering (Walsh, 1969; Solomon and Toksoz, 1970; Richards and Menke, 1983).

Possible lower mantle velocity anomalies and slab effects

High quality short-period data recorded by the 1280 km long, 50+ station Baikal network from 4 deep earthquakes located in the south-west Pacific area (Figures 4.6) are used to identify lower mantle velocity anomalies and possible slab effects [Gao et al., 1996]. The optimal differential travel times and t* between ScS and S, PcP and P, and ScP and P are obtained by cross-correlating one phase with the waveform of the other one. In total 183 differential travel time residuals were used, including 96 ScS-S, 47 PcP-P, and 40 ScP-P residuals. Measurements from Event 1 are shown in Figure 4.7. The combined PcP-P, ScP-P, and ScS-S differential travel time residuals are shown in Figure 4.8. All the differential travel times have a positive slope toward the source direction.

Some of the possible explanations for the observations include:

1). Source mislocation The largest mismatch between the ISC and CMT catalogs is about 15 km for the events used. The depths from the CMT catalog are always larger

than those from the ISC catalog and this results in a positive slope on the travel time residuals toward the source. However, the slope caused by this effect is small. For instance, for an event with a depth of 515 km, a mislocation in depth of 15 km would result in an error on ScS-S residuals of about 0.9 s at $\Delta = 40°$; and at $\Delta = 55°$, it would be about 0.5 s. Therefore, the contribution to the ScS-S slope in Figure 4.8 would be about -0.053 s/deg, which is about 1/8 of the total observed slope.

2). Deep slab effects such as multipathing [Silver and Chan, 1986] and slab diffraction [Vidale, 1987]. The amount of waveform distortion and travel time anomalies depends on many currently unknown facts, such as the depth extension of the slabs, their dip angle and geometry, velocity distribution inside and outside the slabs, and the location of the earthquakes relative to the slabs. At this stage the influence of these effects on the measured residuals cannot be quantitatively estimated.

3). Lower mantle velocity anomalies. A previous study by Wysession et al. [1994] indicates that beneath South China the D" shear wave velocity is high to the north and low to the south. At the north end of the array of bounce points (Figure 4.8) ScS-S residuals are about -4 s while those of ScP-P are about -0.3 s, implying that the high shear wave velocity anomaly is located in the cS branch of the ScS ray path. The large ScS-S negative residuals (-4 s) and small PcP-P negative residuals (-0.3 s) may imply a decrease of the Poisson's ratio in the lower mantle high shear wave velocity zone.

5. GLOBAL SKS ANISOTROPY AND SKS SCATTERING

Currently used seismic discriminants and yield estimates rely on teleseismic P wave amplitude, Lg and P/Lg ratios. Teleseismic P waves are affected by scattering and attenuation in the crust and mantle. A nuclear explosion generates primarily a teleseismic P wave. However multiple scattering from interfaces generate S waves as well as P waves. In order to understand scattering and identify P-S scattered energy from major interfaces in the mantle it is necessary to evaluate the role of anisotropy in the mantle in the scattering process. One effect of anisotropy on S waves such as SKS involves scattering of radially polarised energy into the tangential component as well as changing the relative phase. For SKS splitting by a single layer the tangential amplitudes are proportional to the derivative of the radial amplitudes. However for more complex layering the relationship is more involved. We examined SKS splitting at about 150 stations of the global network for the years 1998-1995.

Data Analysis

A filter was written to extract all long period SKS SKKS seismograms from the Oxford juke box data base at all GEOSCOPE and GSN stations for the period Jan 1988 - May 1995 corresponding to the following: magnitude greater than 6; epicentral distance greater than 90 degrees, for a time interval SKS/SKKS-20 to SKS/SKKS+40 seconds. This resulted in approximately 100 seismograms per station per year. Normal mode synthetics were computed for each seismogram using Harvard moment tensors for source parameters. The normal mode program (Woodhouse 1988) computes seismograms for periods up to 6 seconds. Seismograms and synthetics were rotated into radial and tangential components, and in order to extract good signal to noise ratio events, only those for which the cross-correlation between the observed (phase shifted if necessary) and synthetic radial components was greater than 0.75 were retained for further analysis. This resulted in reducing the number of useful seismograms by a factor of about 10 for a given station, but was necessary because SKS arrivals are weak and often contaminated by microseismic noise of similar frequencies.

Standard 1-layer SKS splitting was performed on the resulting seismograms. Seismograms were rotated into fast and slow directions and the slow component advanced in phase, before rotating back into radial and tangential directions. A grid search of candidate fast and slow directions was made to find the pair that gave minimal tangential energy. Because the long period data is sampled at 1 second intervals we perform phase shifting in the frequency domain which allows continuous phase shifting compared to discrete shifts at the digitization interval in the time domain. After identifying optimal parameters from the grid search a non-linear least squares inversion was carried out using the identified parameters as starting values. Final values had formal errors of several percent for well-determined minima. Splitting parameters were determined for each event at station, but variability in the results and the means, depending on how the results from individual stations were stacked prompted us to make a further detailed analysis.

We have, so far, examined in detail seismograms from GSN stations PAS and ANMO. It appears that the variability in splitting parameters could be attributed to several causes: (1) incident polarisation lying along or within 5 degrees of the fast direction or the direction orthogonal to it (the null-directions) gives rise to insufficient tangential energy to be observable above the background noise (2) scattering effects or anisotropy effects not taken into account in a single layer analysis caused unmodeled fluctuations and (3) noise of unknown origin. We thus restricted our examination to

seismograms for which the tangential/radial energy ratio was high, (greater than 0.3 to avoid the null-direction problem) and for which the cross correlation between the fast and slow components was high (greater than 0.8 to avoid those with significant scattered energy). We found that most such seismograms could be explained by a single layer of azimuthal anisotropy lying beneath the station. Of the 64 seismograms from ANMO, 19 are fit well by a single layer.

Having thus determined the splitting parameters for this layer (50 degrees, 1.6 sec. which compares well with previous estimates of 40 degrees and 1.5 sec.) we searched for effects of a second layer. We modified the normal mode synthetics by passing them through a single layer or double layer of anisotropy and compared them with the radial and azimuthal seismograms. Figure 5.1 shows the comparison of observed radial (dotted curve) and synthetic (smooth curve) seismograms on the left, azimuthal components for the one layer model on the right and those for a candidate two layer model in the centre. Event number, azimuth, first and second layer splitting parameters and CMT name are listed on the extreme right of the figure. Events 23,24,29 and 30 are well-described by a single layer model. Event 27 is better described by the two layer model.

Figure 5.2 shows those events at ANMO that are better described by 2 layers of anisotropy and for which the 1 layer model gives a significant misfit. Because the second layer parameters differ greatly from event to event and because 19 events are well explained by a single layer, some of which have similar incident paths to these events, we conclude that the second layers can not lie beneath ANMO. Otherwise all incident splitting would require inclusion of this layer and one second layer would explain all the data. Anisotropy deep in the mantle, perhaps in the D" region could explain these apparent second layer effects.

We are not yet certain that the apparent second layer effects are from another layer of splitting. The fundamental observation is that a single layer does not suffice and certainly a second layer does a better job, but is this due to more parameterization that allows a phase shift and amplitude change, but maybe is just fitting scattered energy. In either case this is an important effect which is in the data at every station and must be taken into account in comparing observed S waves with synthetics. Extension of this analysis to PAS reveals similar behaviour: a single layer explains most clearly well-split arrivals, but a significant number require a second layer or significant modification of the single layer results.

6. S PHASES FROM LOP NOR NUCLEAR EXPLOSIONS

Introduction

Nuclear explosions differ from earthquakes in that they typically do not produce shear waves, thereby providing a discriminant. However, a series of nuclear explosions detonated in Lop Nor, China reveal possible S waves. These waves could be the result of heterogeneity in the source region, tectonic strain release, or cavity collapse. They could also be P-to-S conversions at the Moho beneath the test site.

Data

The times, locations, and magnitudes of many of the nuclear explosions were obtained from Levshin and Ritzwoller (1995). Events occurring more recently came from IRIS (Incorporated Research Institutions for Seismology) by specifying parameters typical of explosions set off around Lop Nor: a latitude range of 40-43 degrees, a longitude range of 87-92 degrees, and a depth of 0-5 km from January 1, 1970 through September 5, 1996. Table 6.1 lists the twelve explosions. Seismograms from stations with an epicentral range of 20-100 degrees were studied to determine if the Lop Nor explosions generated any shear waves. No shear waves are produced at distances larger than 100 degrees, and crustal structure interferes with body waves less than 20 degrees. The signals were recorded by the Global Seismic Network on three-component (North-South, East-West, and Vertical) broadband seismometers and retrieved from IRIS. The data was not archived at all the stations nor on all the components; thus each explosion contains a different number of records.

The seismograms in the vicinity of the expected S-wave arrival time were viewed using SAC (Seismic Analysis Code). For each event, the three components were plotted together for each individual station. They were quite noisy and were filtered to improve the signal. First, the mean was removed from each seismogram and high-pass filtered with a corner frequency of 0.5 Hz. The trace was cut to +/- 100 s of the expected S wave to detect any amplitude or frequency changes indicative of an S arrival. Only one explosion produced any obvious arrivals, and it was recorded on only one station (discussed later). A variety of different filters were applied to the seismograms to improve the possibility of detecting any S phases. A band-pass filter with corner frequencies at 0.01 Hz and 0.1 Hz gave the best results. By removing any frequencies with periods greater than 100 s, the long period effects of the seismometer were

eliminated. These were plotted using SAC in the same manner as the high-pass filter seismograms. Next, the components were aligned according to the expected S arrival for each explosion. The GMT (General Mapping Tool) was used to plot the components versus epicentral distance. The 1988 event was recorded at only one station. From the GMT plots, a frequency and amplitude variation can be seen for a few stations on most components of the 8-16-90, 5-21-92, 5-15-95, and 6-8-96 events (Figs. 6.1-6.12) at the expected S wave arrival at 100 s.

Discussion

The 1990 event had only one visible S arrival at the expected time–on the east component of station ARU (Arti, Russia). The 1992 event had several possible S waves. They were seen on all components at stations MAJO (Matsushiro, Japan) and OBN (Obninsk, Russia), on the north and vertical components at KIV (Kislovodsk, Russia), on the north and east components at KONO (Kongsberg, Norway), and on the east component of COL (College Outpost, Alaska). Possible S wave arrivals are seen on all components of the 1995 explosion at stations ABKT (Alibek, Turkmenistan), CHTO (Chiang Mai, China), and ARU. There also appears to be a disturbance at KONO. However, it is doubtful it is an S wave due to the duration of the signal. There also appears to be a phase arrival at TLY (Talaya, Russia). This is most likely due to source effects. This station is out of the epicentral limit set for S wave arrivals and was only included because of its close proximity to Lop Nor. Lastly, the most recent event produced possible S waves at ANTO (Ankara, Turkey), CHTO and ARU on the north component.

Analysis

Because the 1992 event is the largest in magnitude ($M_b = 6.5$), it was chosen as the explosion to analyse further. At MAJO, the band-pass filter produces a large arrival on all three components (Fig. 6.13). However, the PcS phase arrives only 7.3 s after the S wave, and the filter may have combined the two phases. The original seismogram was studied to determine if the phases can be seen separately. They are not discernible in the original data, but they are very apparent on the high-pass filtered signal with a corner frequency of 2 Hz and rotated into radial and transverse components (Fig. 6.14). There are several puzzling aspects to this record. Firstly, if the phases are indeed S and PcS, then the S wave is about 15 seconds early. Secondly, at an epicentral distance of almost 40 degrees, there should be very little vertical S phase energy. Lastly, the PcS phase should be almost completely radial. The substantial amount of energy on the tangential

component (even more than on the radial component!) at the expected arrival time of PcS requires explanation. The arrivals are not surface wave Love or Raleigh phases since these waves arrive around 100s and 200s after the expected S wave, respectively.

The records at OBN also show significant energy on all three components (Fig. 6.15). The band- pass filter was narrowed to 0.04 Hz and 0.1 Hz in order to remove long period effects completely. Again, the PcS phase arrives fairly soon (30 s) after the S wave, and the filter may have combined the two phases. The original seismogram on rotated co-ordinates shows the two separate phases (Fig. 16). Again there is substantial energy on the tangential component for the PcS wave. In order to determine if the transverse energy is the result of anisotropy, the seismogram was cut into two plots 5 s long containing the S wave and the PcS wave separately, and the north- south/east-west particle motion was plotted (Figs. 6.17-6.18). For waves passing through a single layer azimuthally anisotropic medium, these plots would be elliptical. Fig. 18 does show some elliptical motion, but Fig. 17 does not. A possible explanation for this is that the PcS wave passes through an anisotropic medium beneath the station. The S wave, on the other hand, may pass through anisotropic material beneath the test site and the station resulting in two or more layer anisotropy effects which as we showed in the previous section can give complicated tangential motion. Alternatively the tangential motion could be a combination of anisotropy and scattering The possible anisotropy and its parameters beneath OBN are currently being analysed.

The anisotropy study that is being done for OBN will be repeated for MAJO. If there are anisotropy effects, it could explain the PcS tangential motion. Further analysis of PcS waves at KIV, COL, and KONO needs to be done before it can be determined whether the study can be undertaken at these stations also.

It is still too early to determine the origins of the arrivals in the data set and more work is required to confirm that they are indeed S waves. The vertical energy must be explained. In addition, the transverse energy seen at many stations for the four explosions needs to be explained. The anisotropy study can be repeated for any station that shows PcS waves. With these PcS phases, the anisotropy beneath the station can be determined easily and compared with that of the previous section which relies on using SKS phases from multiple earthquakes. Then it would be possible to recover the anisotropy beneath the test site. Such steps are necessary in order to recover the physical mechanism giving rise to teleseismic S from nuclear explosions.

7. Tomographic inversion of P-wave travel time residuals

We use the tomograpic inverion scheme of Zhao et al., 1992 to invert the P wave residuals along the line of Figure 3.1. The inversion used three dimensional ray tracing based on the pseusdo bending method (Zhao at al., 1992). Figure 7.1 shows color tomograms along the line at depth intervals of 10 km down to a maximum depth of 180 km. A low velocity zone about 200 km is centered on the lake and persists though all layers. It has a relative contrast of about -3% compared to the surroundings. It is flanked by two high velocity zones either side. Figure 7.2 shows a cross section along the line to a depth of 190 km. Contours are in % Pwave velocity contrast relative to a standard PREM earth model.

8. Stacked receiver function analysis for crustal depth

Figure 8.1 shows stacked receiver functions along the Baikal seismic line of Figure 3.1. The method used is described in Deuker and Sheehan, 1998. An average Moho depth is chosen and a hyperbolic moveout is applied for events arrivng from different azimuths dependent on the velocity model and the location of the piercing point. For each location, on average, arrivals for thirty events have been stacked (upper panel Figure 8.1). The resulting stacks show a clear P_dS phase which is presumed to correspond to the Moho. Depths were based on the conversion of the delay time of the P_dS phase relative to P and using our P-wave model for P velocity and a Poisson's ratio of 0.25 for the S-wave velocity. In the Mongolian fold belt and right up to the rift zone the crustal thickness is 45 km. However northwest of the rift zone and into the Siberian craton the crust appears to be thinner decreasing to 37 km 150 km NW of the rift axis.

9. CONCLUSIONS AND RELEVANCE TO MONITORING THE COMPREHENSIVE TEST BAN TREATY

In sections 1-4 we described the Baikal rift zone experiment and the use of teleseismic body waves to determine that the asthenosphere uplifts in broad region hundreds of km wide. The upwarp is associated with P wave and S waves delays the latter being three times the former. It is also associated with strong attenuation of high frequencies. We suspect this mantle anomaly has resulted from small scale convective motion in which hot material has upwelled beneath the rift. Pervasive anisotropy is

observed a phenomenon expected to accompany finite shearing of convecting mantle material. In section 5 we compared normal mode synthetics with SKS waves and find that nearly every station of the GSN is underlain by anisotropic mantle. Detailed study of ANMO and PAS reveals that about one third of the arrivals have more complicated waveforms than expected from a single anisotropic layer and are better explained by a second layer of anisotropy. However the second layer lies remote from the station perhaps at the core-mantle boundary and varies from event to event. Alternatively these waveform complications could be due to scattering.

In section 6 we study S waves generated from Nuclear explosions at Lop Nor. Nuclear explosions are not normally associated with S waves. However Lop Nor nuclear explosions generate observable arrivals at the times of teleseismic S that could have been generated at the source by cavity collapse, tectonic stress release, or P-S conversions. P-S conversions at the core-mantle interface, PcS, can explain some of the arrivals. Elliptical particle motion of these arrivals is explicable as a result of receiver-side anisotropy. S-waves generated at the source would be affected both by receiver-side anisotropy as well as source-side anisotropy. Recognition of such effects is needed to reconstruct the original S wave polarisation and thereby compare the various candidate mechanisms of generation of nuclear explosion S. The ultimate objective is to ascertain if the particle motion is aligned in the direction of inferred tectonic stress release, or corresponds to P-S conversions that would be radially directed.

Most teleseismic location schemes assume the Earth is laterally homogeneous. However in the Baikal rift zone a localised delay of 1 second occurs flanked by early arrivals of 0.3 seconds either side. These delays are dependent on azimuth and so will effect event location in this area. Similar delays and structures have been observed in the Rio Grande Rift, and the Basin and Range rift province of North America and on the plateau uplift surrounding the east African rift. All these regions correspond to negative Bouguer anomalies and near-normal crustal thicknesses, except in the rift zones themselves where crustal thinning of about 10 km is observed. Thus the delaying structures are probably in the mantle and this is corroborated by parallax shifts in the patterns of residuals as a function of incident direction. We presume such mantle anomalies exist beneath many other continental regions throughout the world and this work suggests a strategy to use gravity in conjunction with known crustal thickness for their identification.

Probably the greatest implication of low Q low velocity mantle under continental

tectonic zones are the effects of attenuation. Ringdal et al., (1992) find that the yield Y in k.t. for nuclear explosions at the Shagan River test site, Russia, is related to body wave magnitude by

$$m_b = 0.75 \log Y + 4.43$$

for body waves in the 2-4 Hz frequency range. We can estimate the underestimate of yield for regions of such as a rift zone owing to upper mantle attenuation. Let the contrast in t^* be δt^* then the ratio of yields in the two zones is given by,

$$Y_1/Y_2 = e^{(-\pi f \delta t^*/0.75)}$$

For example a δt^* of 0.1 results in a reduction of estimated yield of 0.28 of the value had the explosion been detonated outside of the rift assuming body waves of 3 Hz are used in the estimate. This places extra requirements on techniques to monitor suspected nuclear tests in continental rift zones or regions above upwelling hot mantle.

Convection in the mantle beneath continents brings hot material from depth which has the effect of lowering P and S wave velocities as well as Q, and inducing anisotropy. As a result, estimates of yield based on body waves could be as much as a factor of three too low for events detonated above such an upwelling current. Global tomography maps (Woodhouse, 1995 in Press, personal communication) indicate such low velocity regions are common beneath orogenic and rift zones on the continents. Accurate location of nuclear events will have to take both lateral heterogeneity in velocity from such thermal effects as well as that from anisotropy induced by the flow. Seismic anisotropy can result in converted phases, and has strong effect on surface waves.

Our work indicates that modelling of seismic waves using standard Earth models such as PREM requires the following corrections to fit the data.

1. Inclusion of localised S and P wave travel time anomalies.
2. Recognition of localised attenuation of high frequency P and S.
3. Removal of single layer splitting of S waves.
4. Corrections for deep mantle second layer splitting or scattering from lateral heterogeneity.

This work provides a strategy for extension to other orogenic tectonically active continental regions where global models have insufficient resolution, but geophysical signatures such as gravity, topography, heat flow as well as tectonic history could be used to infer lateral variations in the upper mantle, thereby extending the global

models. The resulting model of the continents would then serve as a basis for inverting seismograms from potential test sites for location and yield, when monitoring a CTBT.

References

Babuska, V., and M. Cara, *Seismic anisotropy in the Earth*, Kluwer Academic Publishers, 1991.

Deiker, K.G., A.F. Sheehan, Mantle discontinuity beneath the Colorado Rocky Mountains and High Plains, *J. Geophys. Res. 103*, 7153-7169, 1978.

Gao, S., P.M. Davis, H. Liu, P.D. Slack, Yu.A. Zorin, N.A. Logatchev, M. Kogan, P. Burkholder, R.P. Meyer, Asymmetric upwarp of the Asthenosphere beneath the Baikal Rift zone, Siberia, *J. Geophys. Res. 99*, 15,319-15,330, 1994a.

Gao, S., P. M. Davis, H. Liu, P. D. Slack, Yu. A. Zorin, V. V. Mordvinova, V. M. Kozhevnikov, and R. P. Meyer, Seismic Anisotropy and Mantle Flow beneath the Baikal Rift Zone, *Nature, 371*, 149-151, 1994b.

Gao, S., Seismic evidence for Small-scale mantle convection under the Baikal rift zone, Siberia, *PhD thesis*, University of California, Los Angeles, 221 pp., 1995.

Gao, S., P. M. Davis, H. Liu, R. P. Meyer, and Yu. A. Zorin, A lower mantle high shear-wave velocity anomaly inferred from ScS-S, PcP-P, and ScP-P differential travel time residuals, *EOS, Trans. Am. Geophys. Union, 77,* (abstract), 1996.

Gao, S., P. M. Davis, H. Liu, P. D. Slack, A. W. Rigor, Yu. A. Zorin, V. V. Mordvinova, V. M. Kozhevnikov, and N. A. Logatchev, SKS Splitting beneath Continental Rift Zones, *J. Geophys. Res., (submitted)*, 1997.

Halderman, T. P., and P. M. Davis, Q_p beneath the Rio Grande and east African rift zones, *J. Geophys. Res., 96,* 10,113-10,128, 1991.

Levshin, A.L. and M.H. Ritzwoller, Characteristics of surface waves generated by events on and near the Chinese nuclear test site, *Geophys. J. Int.*, 123, 131-148, 1995.

Makeyeva, L. I., L. P. Vinnik, and S. W. Roecker., Shear-wave splitting and small-scale convection in the continental upper mantle, *Nature, 358,* 144-147, 1992.

Popov, A. M., A deep geophysical study in the Baikal region, *Pure Appl. Geophys., 134*, 575-587, 1990.

Richards, P. G., and W. Menke, The apparent attenuation of a scattering medium, *Bull. Seismol. Soc. Am., 73,* 1005-1021, 1983.

Ringdal, F., Marshall, P.D., and Alewine, R. W., Seismic yield determination of Soviet underground unclear explosions at the Shagan River test site, *Geophys. J. Int., 109,* 65-77, 1992.

Sandvol, E., J. Ni, S. Ozalaybey, and J. Schlue, Shear-wave splitting in the Rio Grande

rift, *Geophys. Res. Lett., 19*, 2337-2340, 1992.

Silver, P. G., and W. W. Chan, Observations of body wave multipathing from broadband seismograms; evidence for lower mantle slab penetration beneath the Sea of Okhotsk, *J. Geophys. Res. 91,* 13,787-13,802, 1986.

Silver, P. G., and W. W. Chan, Shear wave splitting and subcontinental mantle deformation, *J. Geophys. Res. 96,* 16,429-16,454, 1991.

Solomon, S.C., and M.N. Toksoz, Lateral variation of attenuation of P and S waves beneath the United States, *Bull. Seismol. Soc. Am., 60,* 819-838, 1970.

Vidale, J.E., Waveform effects of a high-velocity, subducted slab, *Geophys. Res. Lett., 14*, 542-545, 1987.

Vinnik, L. P., L. I. Makeyeva, A. Milev, and A. Yu. Usenko, Global patterns of azimuthal anisotropy and deformations in the continental mantle, *Geophys. J. Int., 111,* 433-447, 1992.

Walsh, J. B., New analysis of attenuation in partially melted rock, *J. Geophys. Res., 74*, 4333-4337, 1969.

Woodhouse, J. H., and A. M. Dziewonski, Mapping the upper mantle: Three-dimensional modelling of earth structure by inversion of seismic waveforms, *J. Geophys. Res., 89*, 5953-5986, 1984.

Woodhouse, J.H., The calculation of eigenfrequencies and eigenfunctions of the free oscillations of the Earth and the Sun., in Seismological Algorithms, *Academic Press Limited*, 321- 370, 1988.

Wysession, M.E., L. Bartko, and J.B. Wilson, Mapping the lowermost mantle using core-reflected shear waves, *J. Geophys. Res., 99*, 13,667-13,684, 1994.

Zhao, D., A. Hasegawa and S. Horiuchi (1992) Tomographic Imaging of P and S wave velocity structure beneath northeastern Japan, *J. Geophys. Res., 97*, 19909-19928.

Zoback, M. L., First- and second-order patterns of stress in the lithosphere; the World Stress Map Project, *J. Geophys. Res., 97,* 11,703-11,728, 1992.

Zorin, Y. A., *Recent Structure and Isostasy of the Baikal Rift Zone and Adjacent Territories,* (in Russian), 168 pp., Nauka, Moscow, 1971.

9. FIGURE CAPTIONS

Figure 2.1: USA-USSR Baikal 1991 Seismic Array Study UCLA station Locations.

Figure 2.2: Geographic location of earthquakes with mb $\geq$ 5.0 occurred during July 7 and Oct 5, 1991 (Source: NOAA).

Figure 2.3: Comparison of teleseisms and spectra from a Northern California event from the 4 broadband stations.

Figure 2.4: A seismic section from a teleseism from 1 Hz vertical sensors, on data stream 1, i.e. the continuous stream.

Figure 3.1: USA-USSR Baikal 1992 seismic array study UCLA station locations.

Figure 3.2: Geographic location of earthquakes with mb $\geq$ 5.0 recorded by UCLA stations during June 11 and Oct 5, 1992. (Source: NOAA)

Figure 3.3: Seismograms for teleseismic events recorded at profile stations.

Figure 4.1a: Polynomial surface determined by downward projection of the residual patterns of Figure 3. The X axis is taken along the line connecting the two stations at the end of the profile, and the Y axis is perpendicular to X and pointing to the Northeast. The origin of the co-ordinate system is at the middle point of the lake, along the profile. The contours on the top and bottom planes are depth of the asthenosphere in kilometres. The shaded area on the top plane represents Lake Baikal. The uncertainty of the depth of the polynomial surface is $\pm$17 km.

Figure 4.1b: Regional Bouguer gravity anomaly and cross section of Figure 4.1 along the profile. Crustal thicknesses are taken from deep seismic sounding. The averaged misfit between the calculated gravity anomaly (solid line in Figure à) from our deep structure (Figure b) and measured regional anomaly (circles in Figure a) is about 1.0 mGal. The best fitting asthenosphere/lithosphere density contrast is -0.6%.

Figure 4.2a: Mean travel time residual curves from the 1992 array event groups. Each vertical unit represents one second. Each horizontal grid line is the zero line of a group, with group name written on the right side of the diagram. The two vertical curves connect the location of the two minima on the residual curves. The insert on the right shows average arrival direction of each event group.

Figure 4.2b: Isotropic velocity model determined from Bayesian non-linear inversion of the travel time residuals using a polynomial to represent the undulations of the lithosphere/asthenosphere boundary that best explains the travel time variation.

Figure 4.2c: Mean S-wave travel time residuals from 4 events from the South relative to the IASP91 earth model.

Figure 4.3a: Map showing the region with the stations of the seismic array extending from the Siberian platform across the Baikal rift zone into Mongolia and results of SKS splitting measurements.. Stations with well-defined measurements are represented by single circles with size proportional to the splitting. The line drawn through each circle gives the fast polarisation direction. Those with 2 inconsistent results are plotted as double circles. The shorter and longer line indicates the fast direction of the smaller and larger circle, respectively. Stations represented by squares are those on which anisotropy effects cannot be clearly observed.

Figure 4.3b: Normalised rose diagrams of SKS fast polarisation directions for each of the 6 areas in the BRZ and adjacent areas. Null measurements were excluded in the rose diagrams. The sector width of the rose diagrams is 20°.

Figure 4.4: Results of δt^* measurements. The dots are averaged values over all the events for δt_p^* (Figure A) and δt_s^* (Figure B), and the solid lines are the results of spatial averaging in windows of 200 km wide, moving at steps of 10 km. The thickness of the shaded area is 2 times of the standard error of the mean.

Figure 4.5: Relations between δt_p^* and δt_s^*. Note that the values used are from spatial averaging of the mean values (the solid curves in Figure 4.5). The best fitting results and the cross correlation coefficient are shown in the figure.

Figure 4.6: A Lambert projection map showing locations of events (numbered dots) used in lower mantle structure study, stations (open triangles), and ScS or PcP bounce points (filled triangles).

Figure 4.7: Results of travel time residual measurements for Event 1 plotted against latitudes of ScS bounce points.

Figure 4.8: PcP-P, ScP-P, and ScS-S residuals for events 1, 2, and 3 plotted at latitudes of ScS bounce points.

Figure 5.1: SKS waveforms (dotted lines) for GSN station ANMO compared to normal mode synthetics (smooth curves, Woodhouse, 1988). Radial seismograms are on the left. Azimuthal components modelled as a double layer of anisotropy are in the centre and as a single layer on the right. On the far right numbers give; event number, azimuth, fast directions (anticlockwise from north), and delay in seconds for the upper and lower layers, and CMT event name. Note events 21,23,24,29 and 30 are adequately described by a single layer of splitting. However event 27 and possibly 28 are better described by the double layer.

Figure 5.2: SKS waveforms from the 64 analysed at ANMO for which a 2 layer anisotropy is a good or better fit than one layer. The fact that the second layer parameters are different and incident rays close to these from other events did not exhibit second layer effects leads us to believe these effects are coming from deep in the mantle; quite possibly in the D" region of the lowermost mantle.

Figure 6.1 - 6.12: East, north and vertical components of Lop Nuclear Explosions plotted as a function of epicentral distance, and centred on the expected time of teleseismic S were it generated by the explosions.

Figure 6.13: Possible S wave arrivals at MAJO. Interference between the S and PcS waves gives the apparent long period structure of the filtered seismograms.

Figure 6.14: High pass filtered version of the record shown in Figure 6.13, showing candidate S and PcS arrivals.

Figure 6.15: Possible S wave arrivals at OBN. Interference between the S and PcS waves gives the apparent long period structure of the filtered seismograms.

Figure 6.16: High pass filtered version of the record shown in Figure 6.15, showing candidate S and PcS arrivals

Figure 6.17: Particle motion of the S motion at OBN showing complicated polarisation effects that may be due to a combination of source side and receiver side anisotropy and/or scattering.

Figure 6.18: Particle motion of the PcS wave at OBN. The simple shape is consistent with receiver-side scattering.

Figure 7.1: Tomograms from Lake Baikal P wave travel time residuals. Perturbations are in % P-wave velocity contrast. Low velocities are associated with the location of Lake Baikal but are flanked by high velocity zones either side.

Figure 7.2: Cross-section of the velocity perturbations of Figure 7.1 The uppermost mantle beneath lake Baikal has a velocity contrast of -1% to -2 %, but is flanked by a velocity increase of about 2%.

Figure 8.1: Stacked receiver functions from the Lake Baikal data. The top panel gives the number of events in each stack. The numbers in square boxes are station numbers. Those beginning with a 1 refer to 1991 array and those beginning with a 2 refer to the 1992 array. The lower panel shows the stacked receiver functions with large arrivals corresponding to the depth of the Moho. Thick crust is seen in the Mongolian fold belt, whereas NW of Lake baikal (0 km) the crust thins on the cratonic side. Presumably the thickened crust is related to past tectonics

related to the fold event and the present tectonics have not thinned it appreciably in spite of the rifting.

Received _____

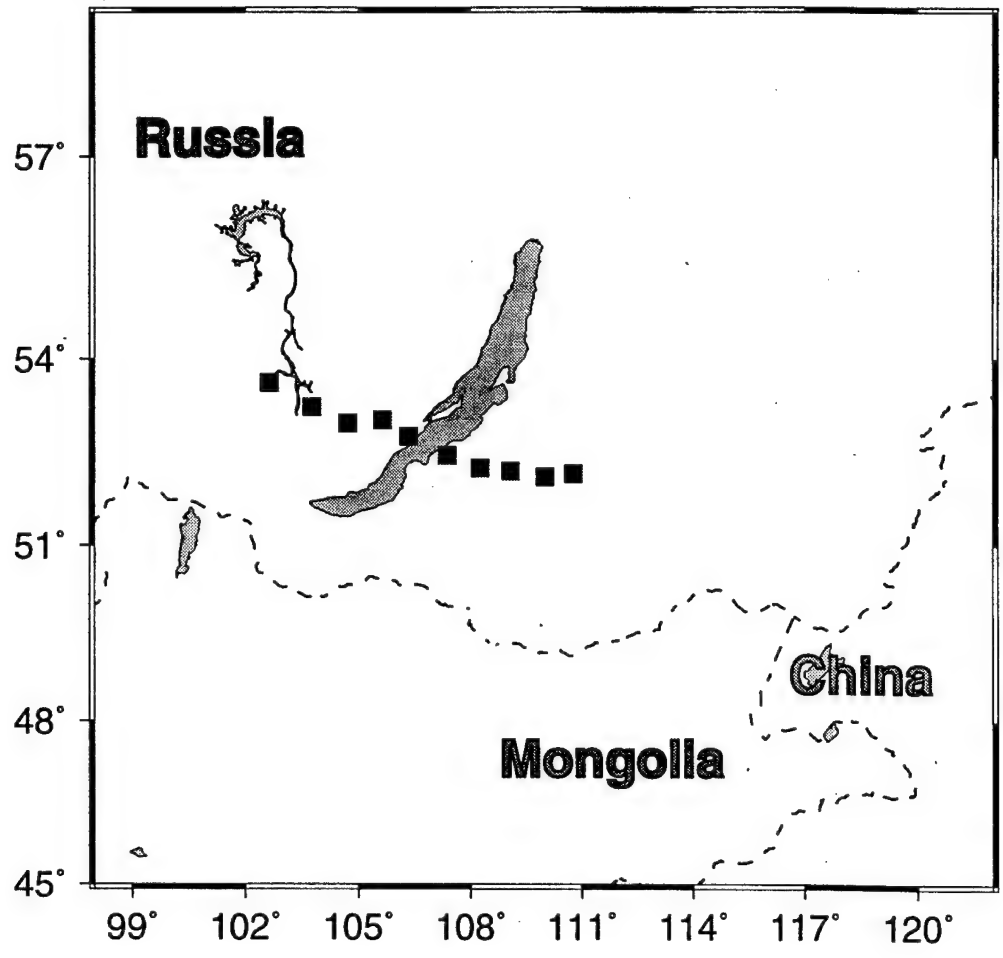
Russia
57°
54°
51°
48°
45°
99°
102°
105°
108°
111°
114°
117°
120°
China
Mongolia

Figure 2.1

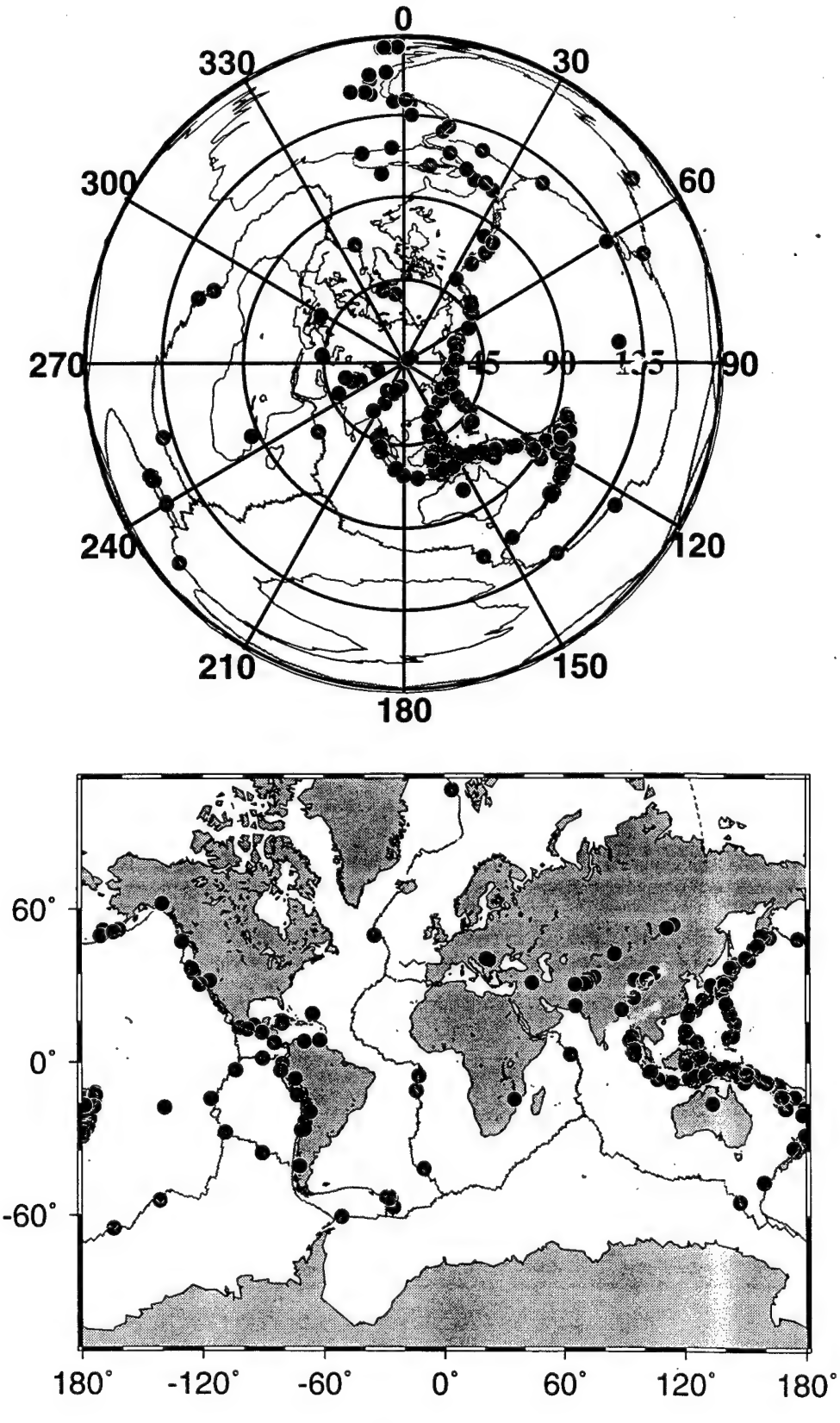
0
30
60
90
120
150
180
210
240
270
300
330
45
90
135
60°
0°
-60°
180°
-120°
-60°
0°
60°
120°
180°

Figure 2.2

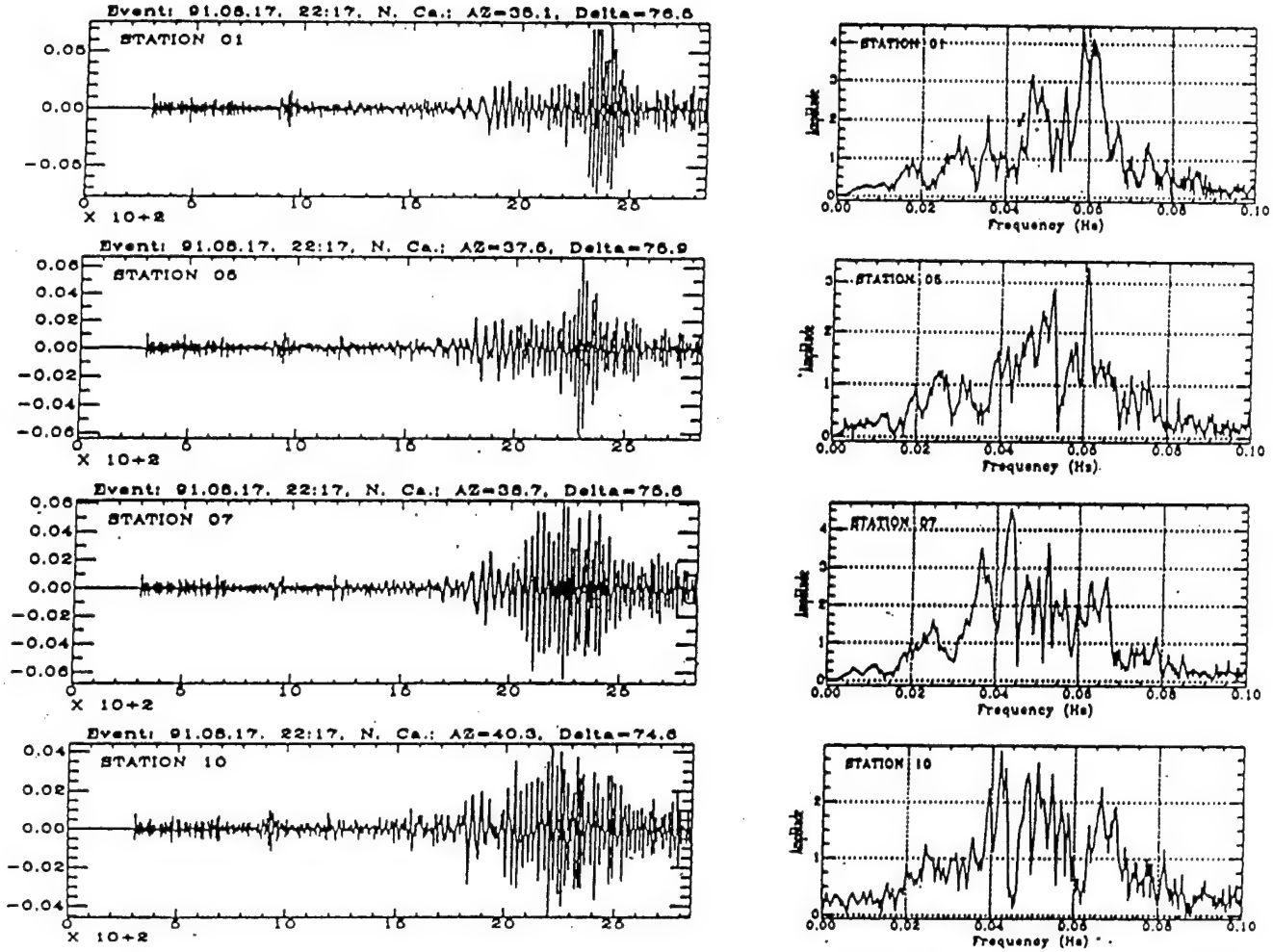
Event: 91.06.17. 22:17. N. Ca.: AZ=36.1, Delta=76.6
STATION 01
Event: 91.06.17. 22:17. N. Ca.: AZ=37.6, Delta=76.9
STATION 05
Event: 91.06.17. 22:17. N. Ca.: AZ=38.7, Delta=76.6
STATION 07
Event: 91.06.17. 22:17. N. Ca.: AZ=40.3, Delta=74.6
STATION 10
X 10+2
STATION 01
STATION 05
STATION 07
STATION 10
Frequency (Hz)

Figure 2.3

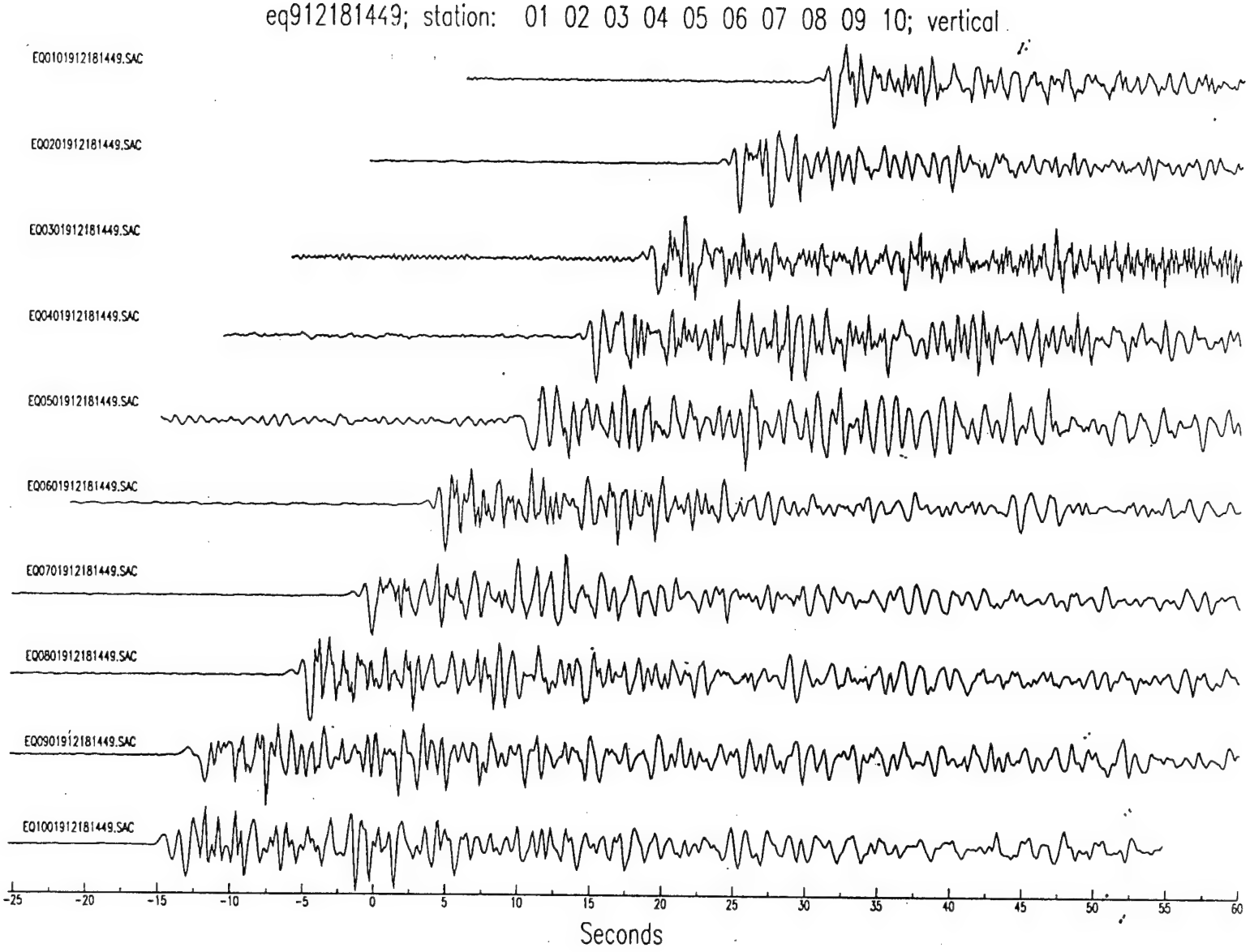
eq912181449; station: 01 02 03 04 05 06 07 08 09 10; vertical
EQ0101912181449.SAC
EQ0201912181449.SAC
EQ0301912181449.SAC
EQ0401912181449.SAC
EQ0501912181449.SAC
EQ0601912181449.SAC
EQ0701912181449.SAC
EQ0801912181449.SAC
EQ0901912181449.SAC
EQ1001912181449.SAC
-25 -20 -15 -10 -5 0 5 10 15 20 25 30 35 40 45 50 55 60
Seconds

Figure 2.4

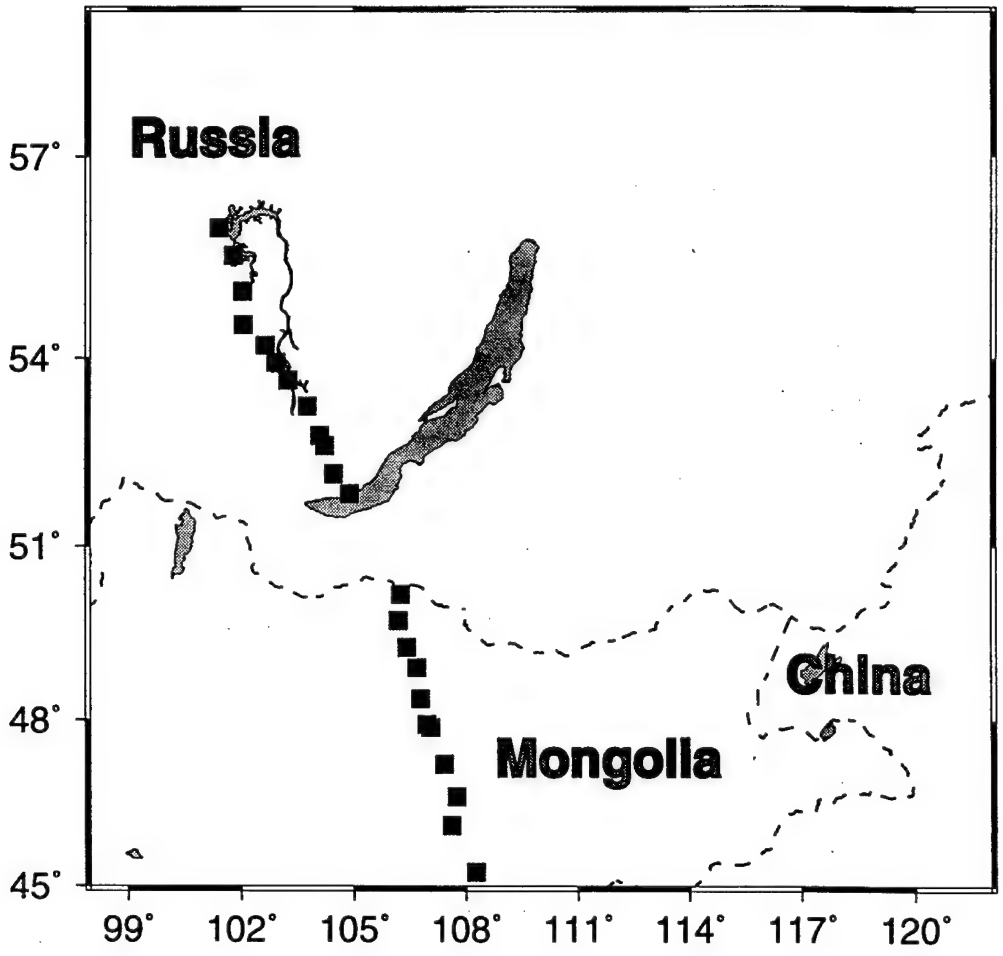
Russia
China
Mongolia
57°
54°
51°
48°
45°
99°
102°
105°
108°
111°
114°
117°
120°

Figure 3.1

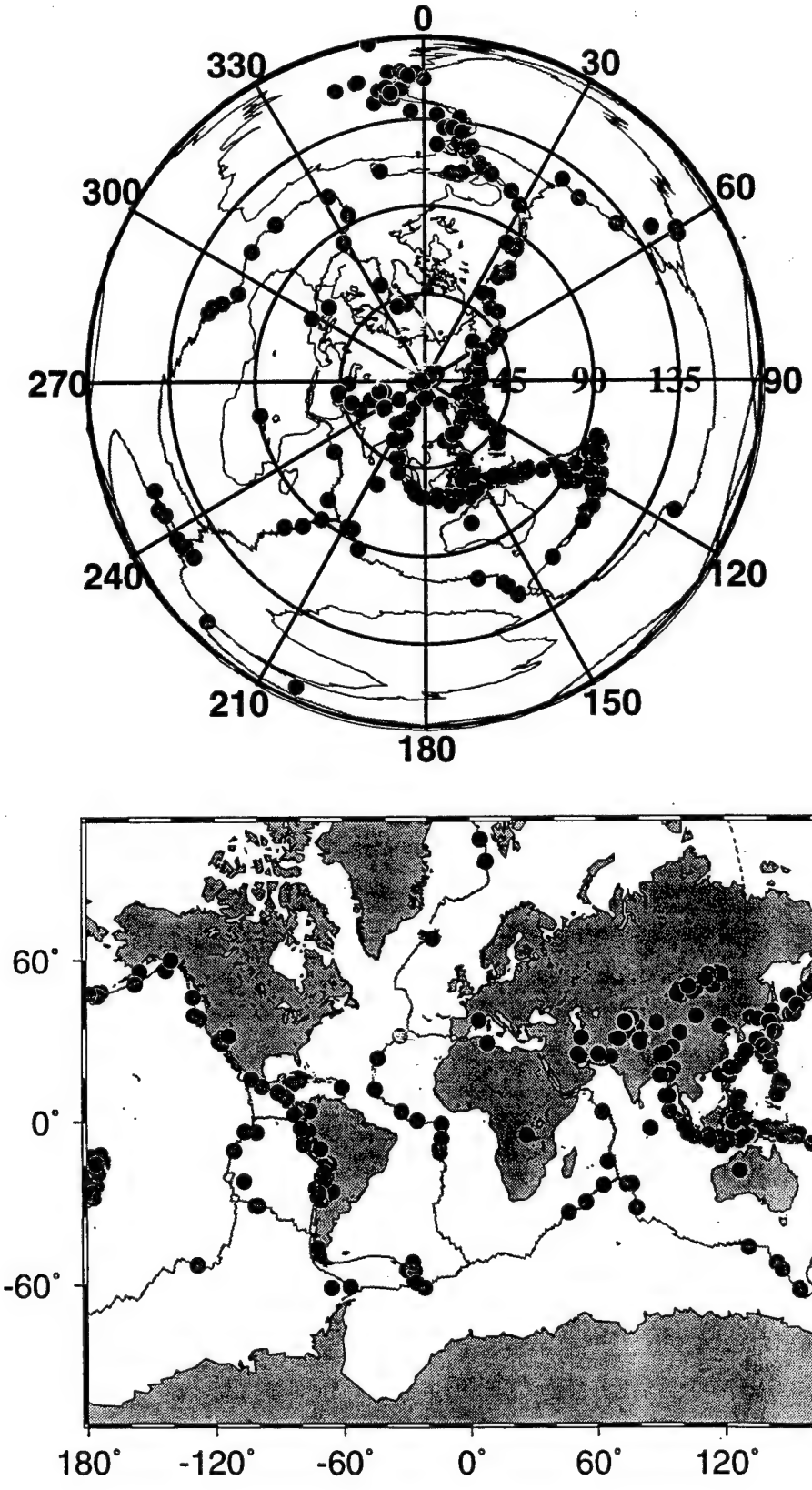
0
30
60
90
120
150
180
210
240
270
300
330
45
90
135
90
60°
0°
-60°
180°
-120°
-60°
0°
60°
120°
180°

Figure 3.2

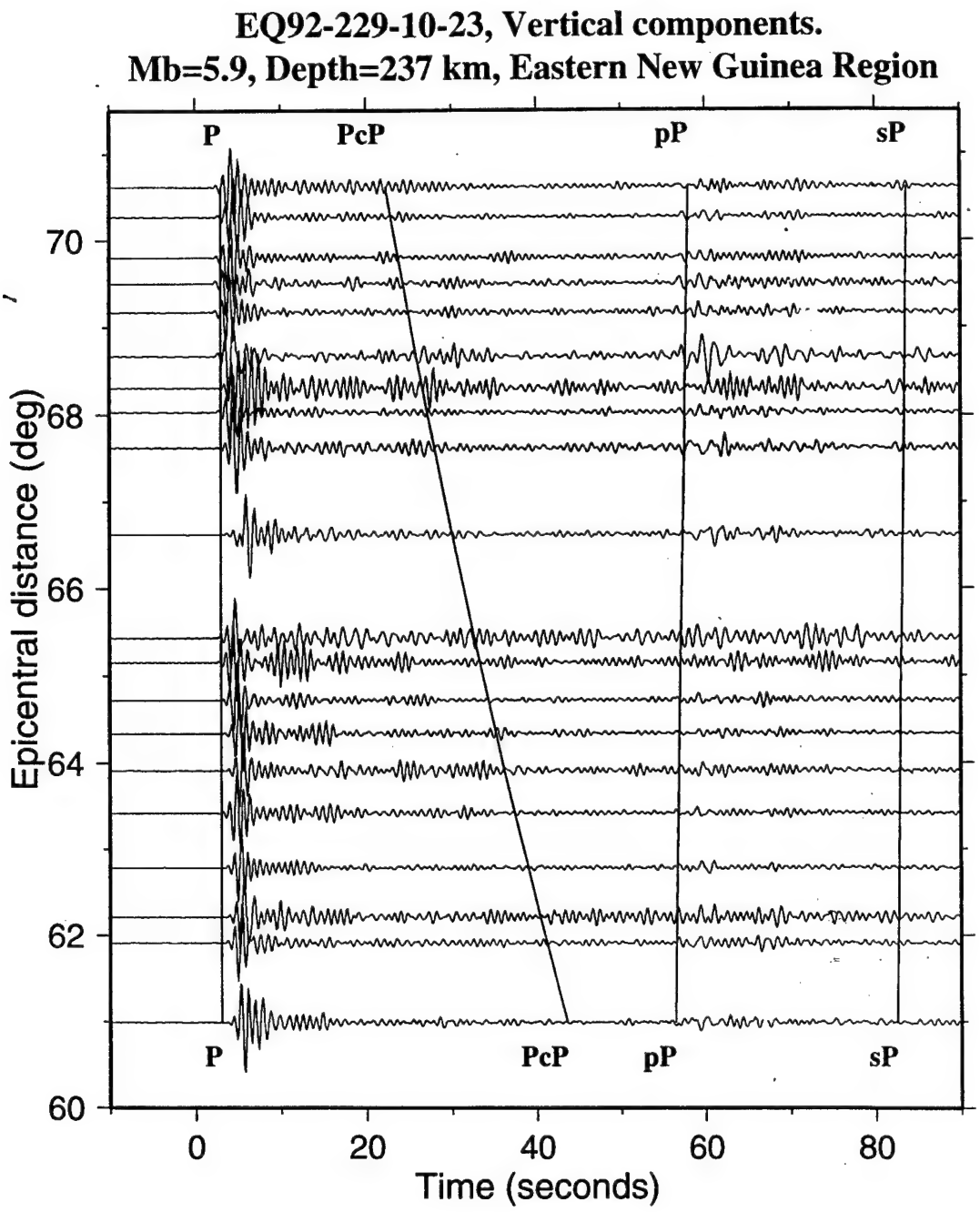
EQ92-229-10-23, Vertical components.
Mb=5.9, Depth=237 km, Eastern New Guinea Region
P
PcP
pP
sP
P
PcP
pP
sP
70
68
66
64
62
60
Epicentral distance (deg)
0
20
40
60
80
Time (seconds)

Figure 3.3

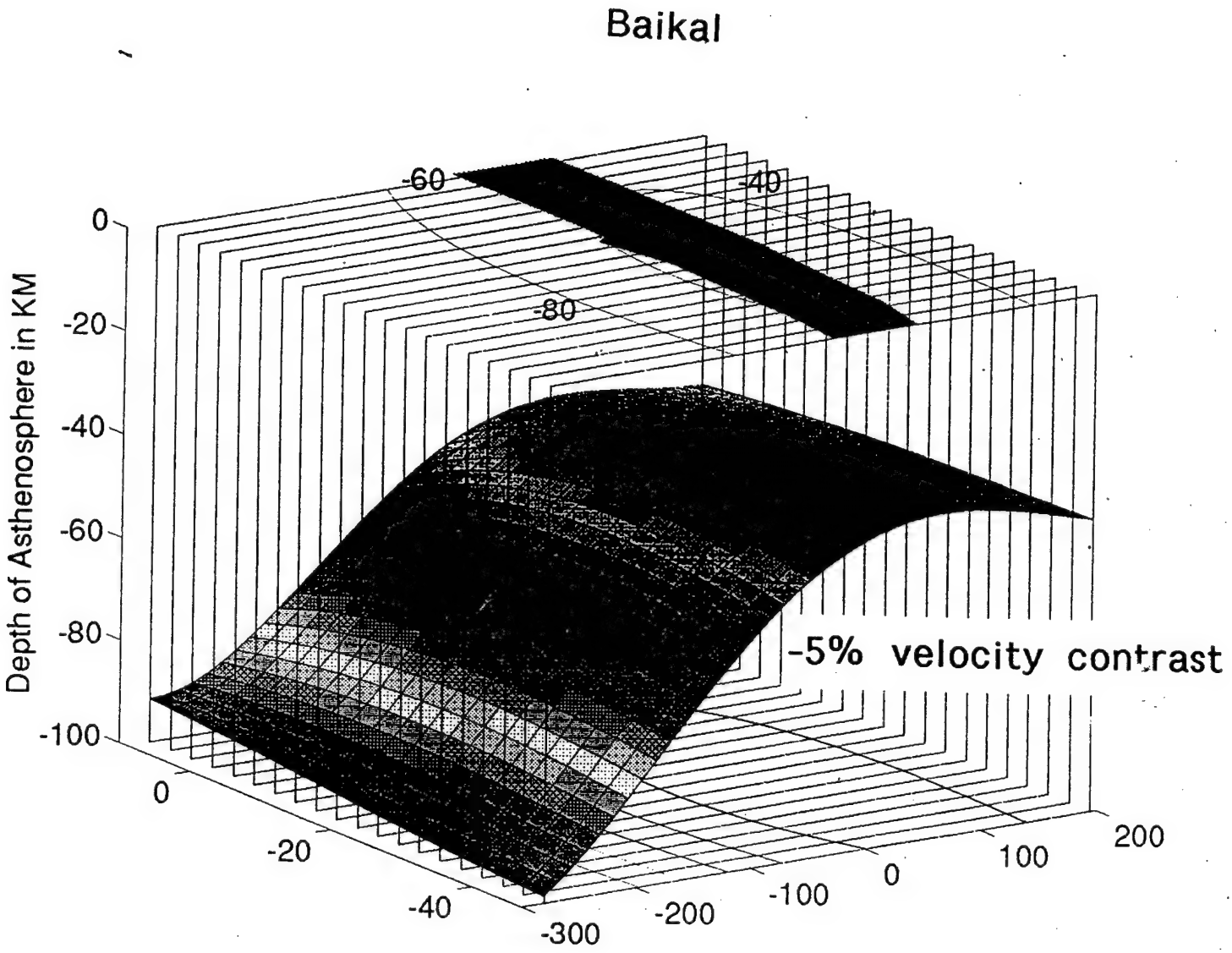
Baikal
-60
-40
-80
0
-20
-40
-60
-80
-100
Depth of Asthenosphere in KM
-5% velocity contrast
0
-20
-40
-300
-200
-100
0
100
200

Figure 4.1a

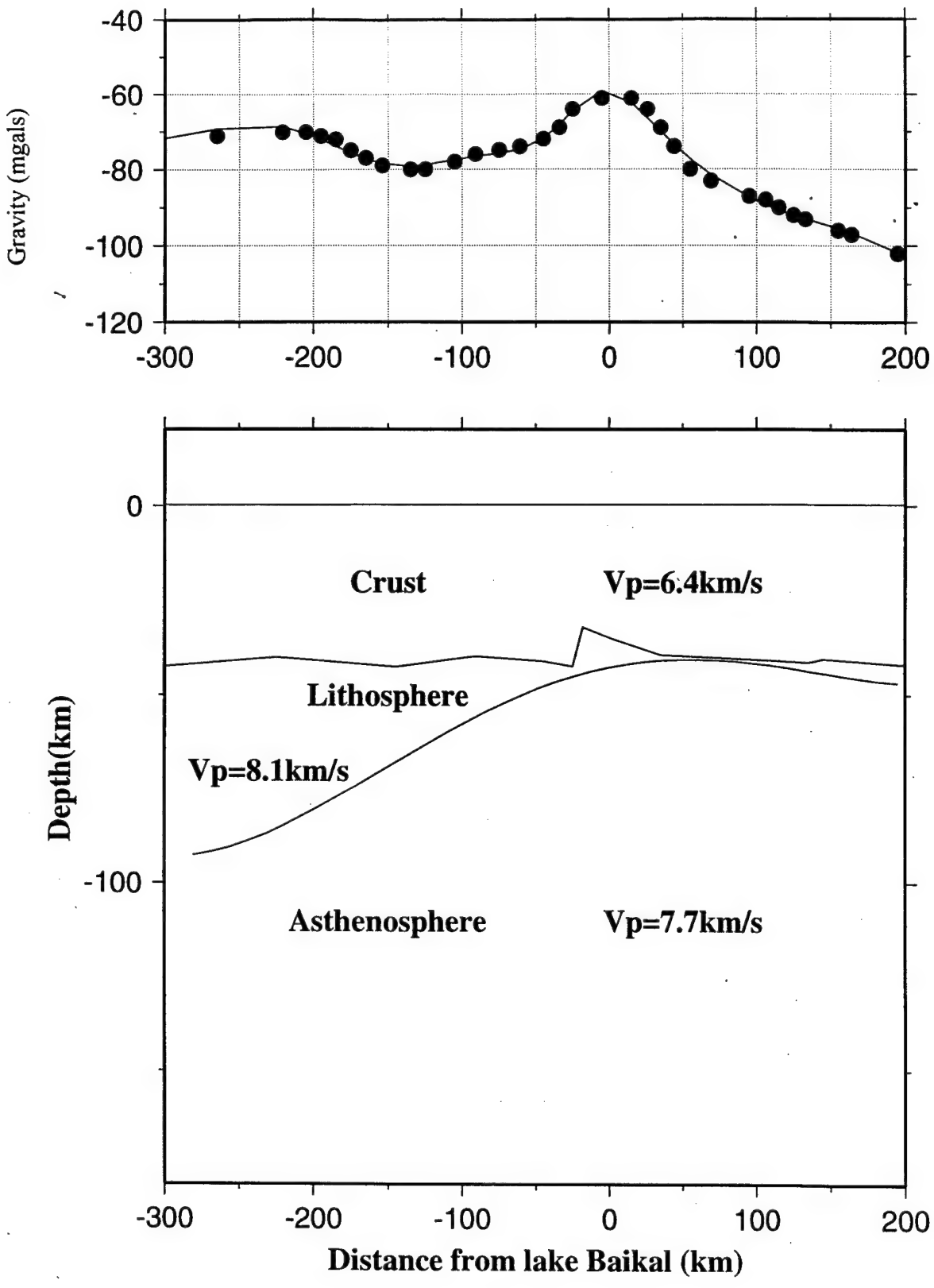
-40
-60
-80
-100
-120
Gravity (mgals)
-300
-200
-100
0
100
200
0
Crust
Vp=6.4km/s
Lithosphere
Vp=8.1km/s
-100
Asthenosphere
Vp=7.7km/s
Depth(km)
-300
-200
-100
0
100
200
Distance from lake Baikal (km)

Figure 4.1b

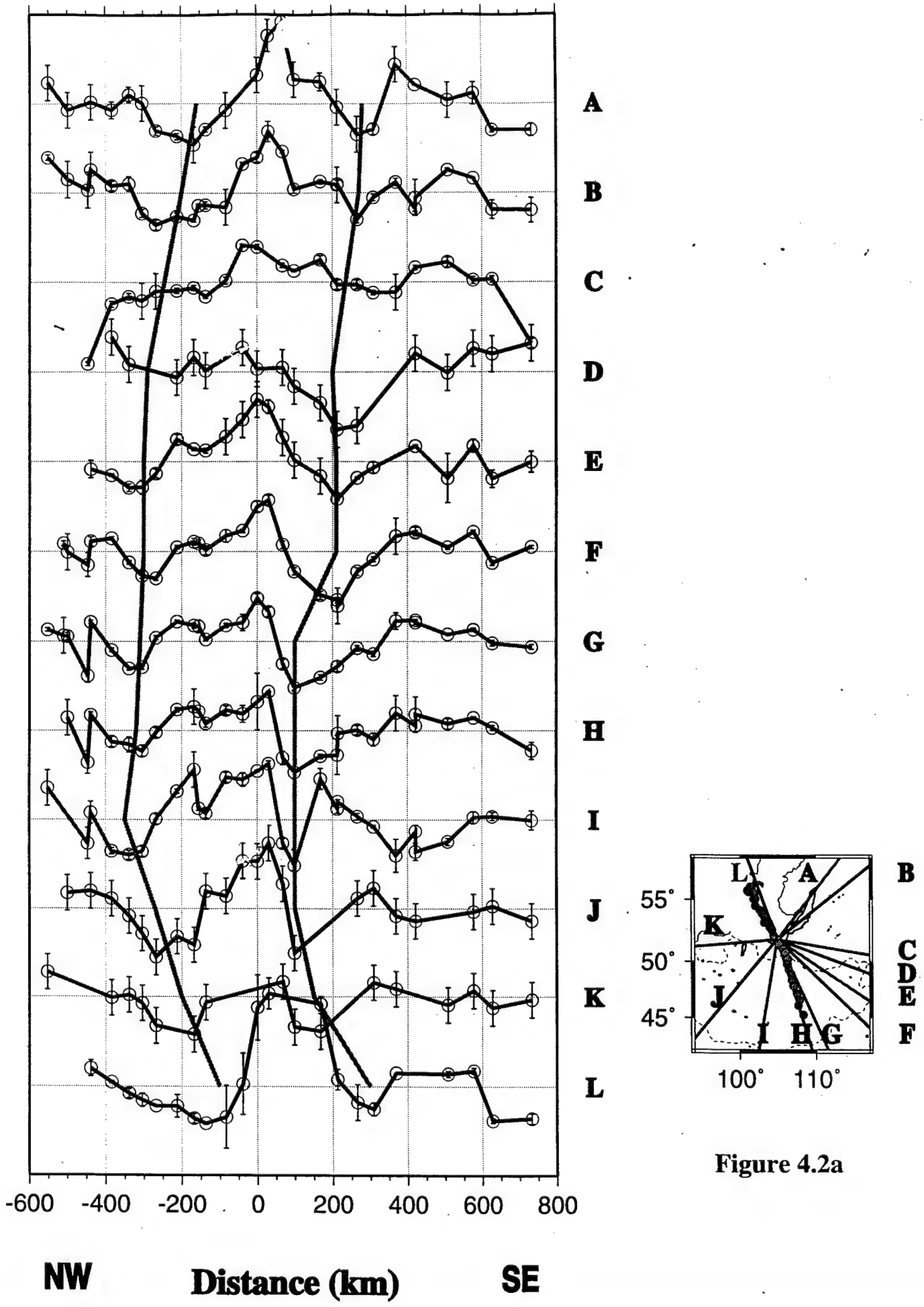
A
B
C
D
E
F
G
H
I
J
K
L
-600
-400
-200
0
200
400
600
800
NW
Distance (km)
SE
L
A
B
55°
K
50°
C
D
E
J
45°
I
H
G
F
100°
110°

Figure 4.2a

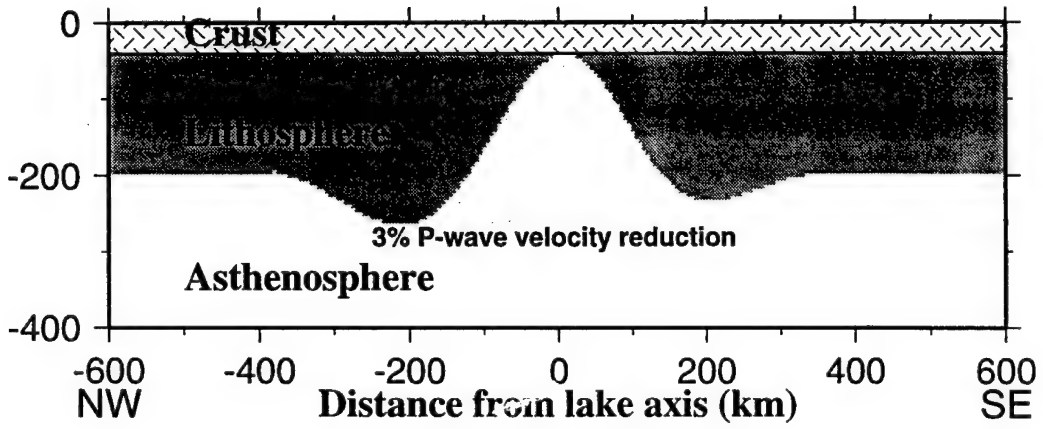
0
-200
-400
Crust
Lithosphere
3% P-wave velocity reduction
Asthenosphere
-600
-400
-200
0
200
400
600
NW
Distance from lake axis (km)
SE

Figure 4.2b

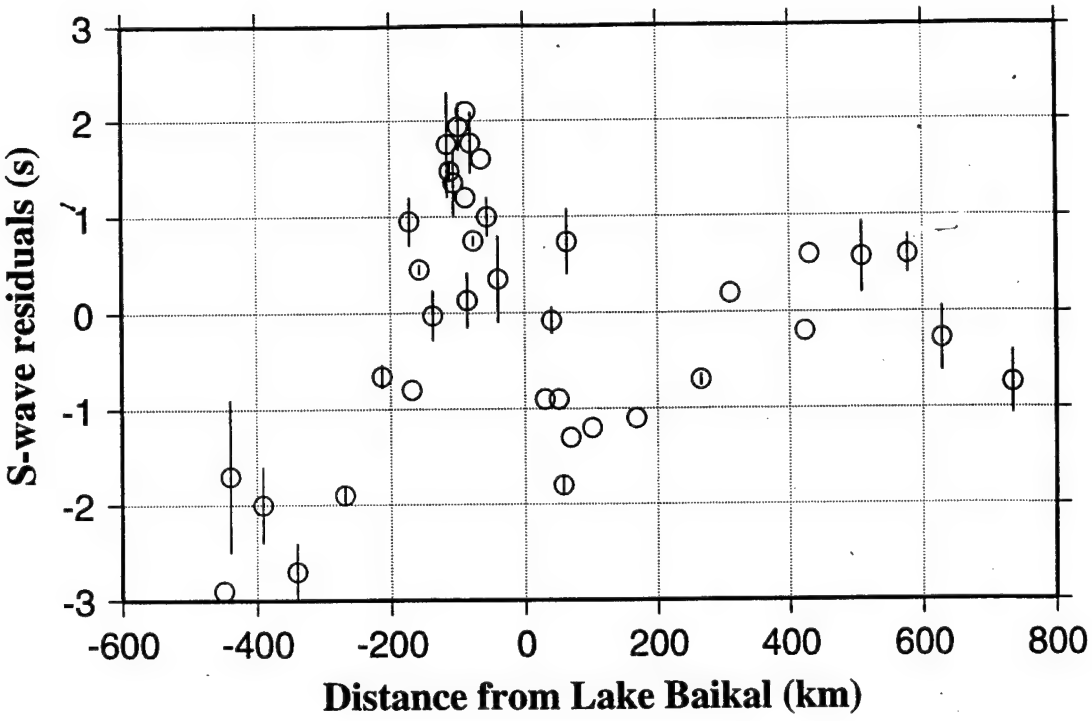
S-wave residuals (s)
3
2
1
0
-1
-2
-3
-600
-400
-200
0
200
400
600
800
Distance from Lake Baikal (km)

Figure 4.2c

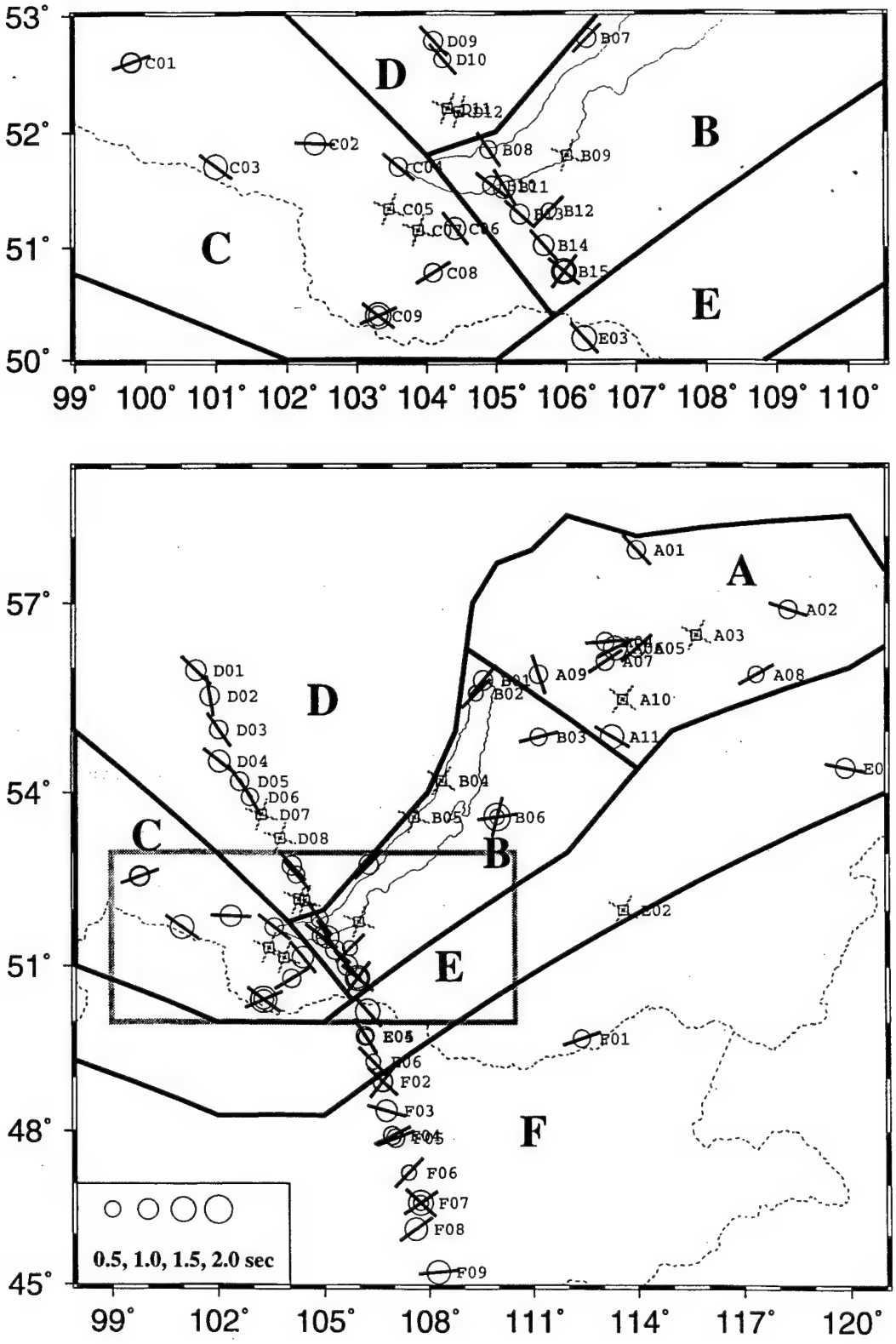
53°
52°
51°
50°
99° 100° 101° 102° 103° 104° 105° 106° 107° 108° 109° 110°
D
B
C
E
C01
C02
C03
C04
C05
C06
C07
C08
C09
D09
D10
D11
D12
B07
B08
B09
B11
B12
B14
B15
E03
57°
54°
51°
48°
45°
99° 102° 105° 108° 111° 114° 117° 120°
A
D
C
B
E
F
A01
A02
A03
A04
A05
A07
A08
A09
A10
A11
B01
B02
B03
B04
B05
B06
D01
D02
D03
D04
D05
D06
D07
D08
E01
E05
E06
F01
F02
F03
F04
F05
F06
F07
F08
F09
0.5, 1.0, 1.5, 2.0 sec

Figure 4.3a

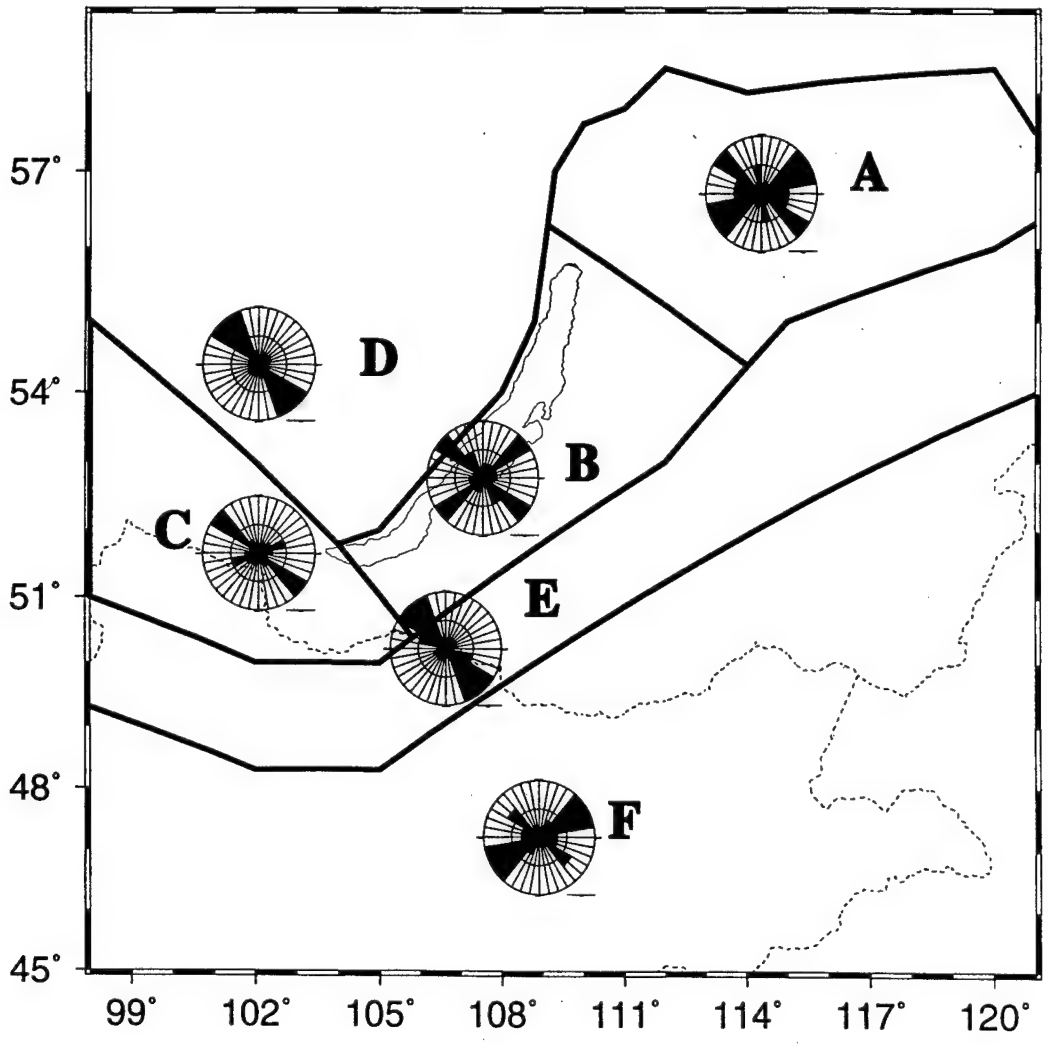

Figure 4.3b

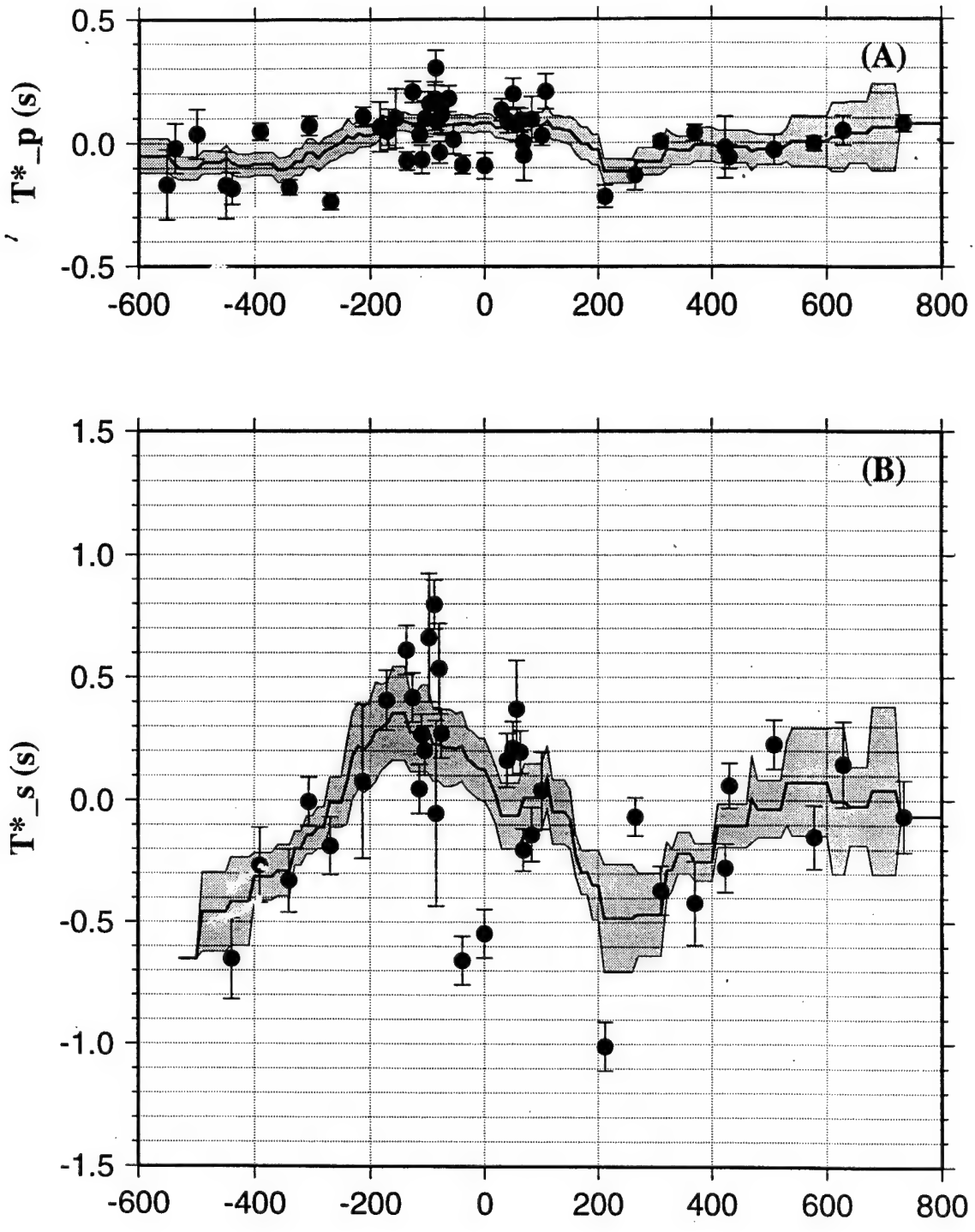
(A)
T*_p (s)
0.5
0.0
-0.5
-600
-400
-200
0
200
400
600
800
(B)
T*_s (s)
1.5
1.0
0.5
0.0
-0.5
-1.0
-1.5
-600
-400
-200
0
200
400
600
800
Distance from Lake Baikal (km)

Figure 4.4

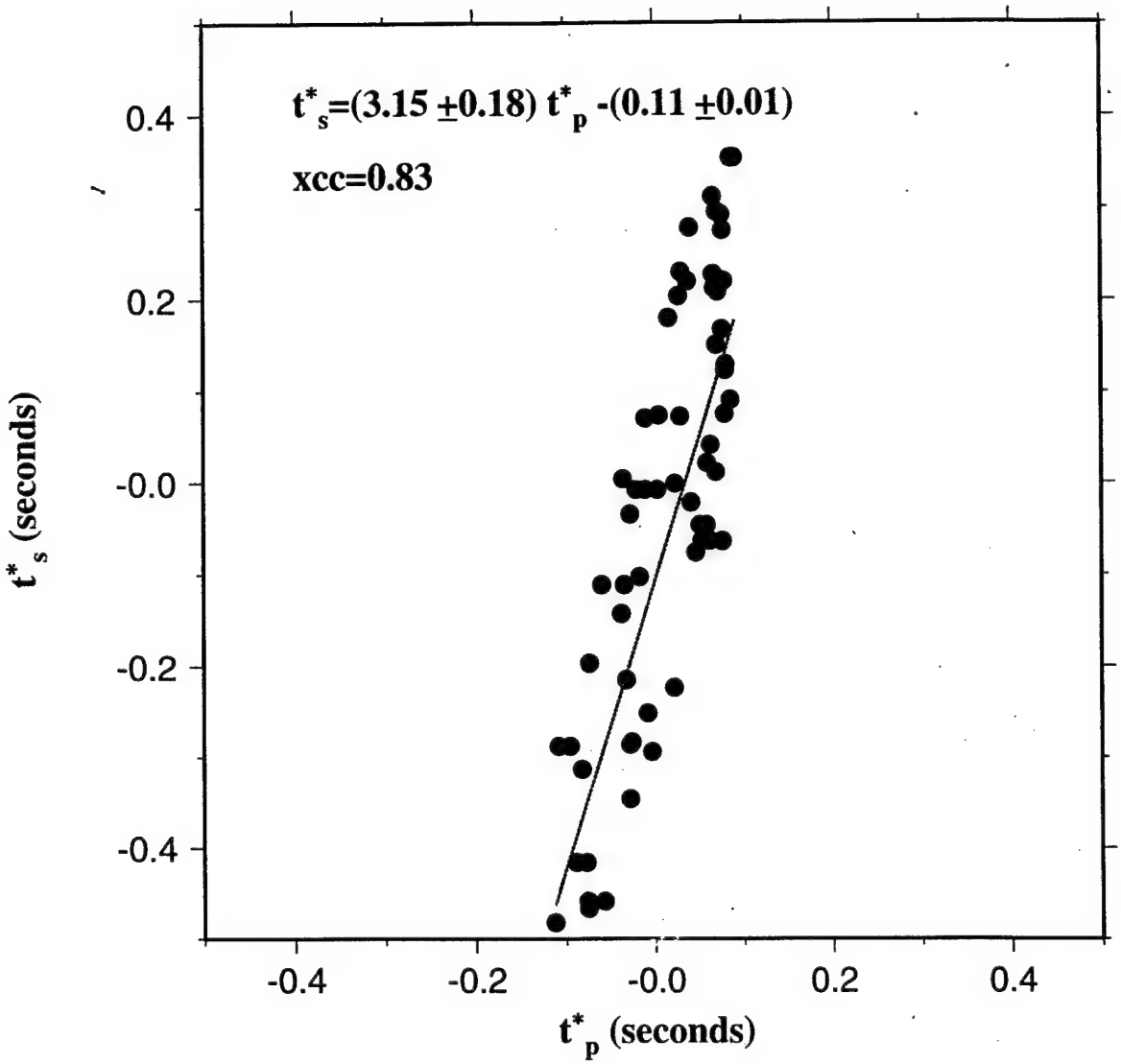
t^*_s=(3.15 ±0.18) t^*_p -(0.11 ±0.01)
xcc=0.83
0.4
0.2
-0.0
-0.2
-0.4
t^*_s (seconds)
-0.4
-0.2
-0.0
0.2
0.4
t^*_p (seconds)

Figure 4.5

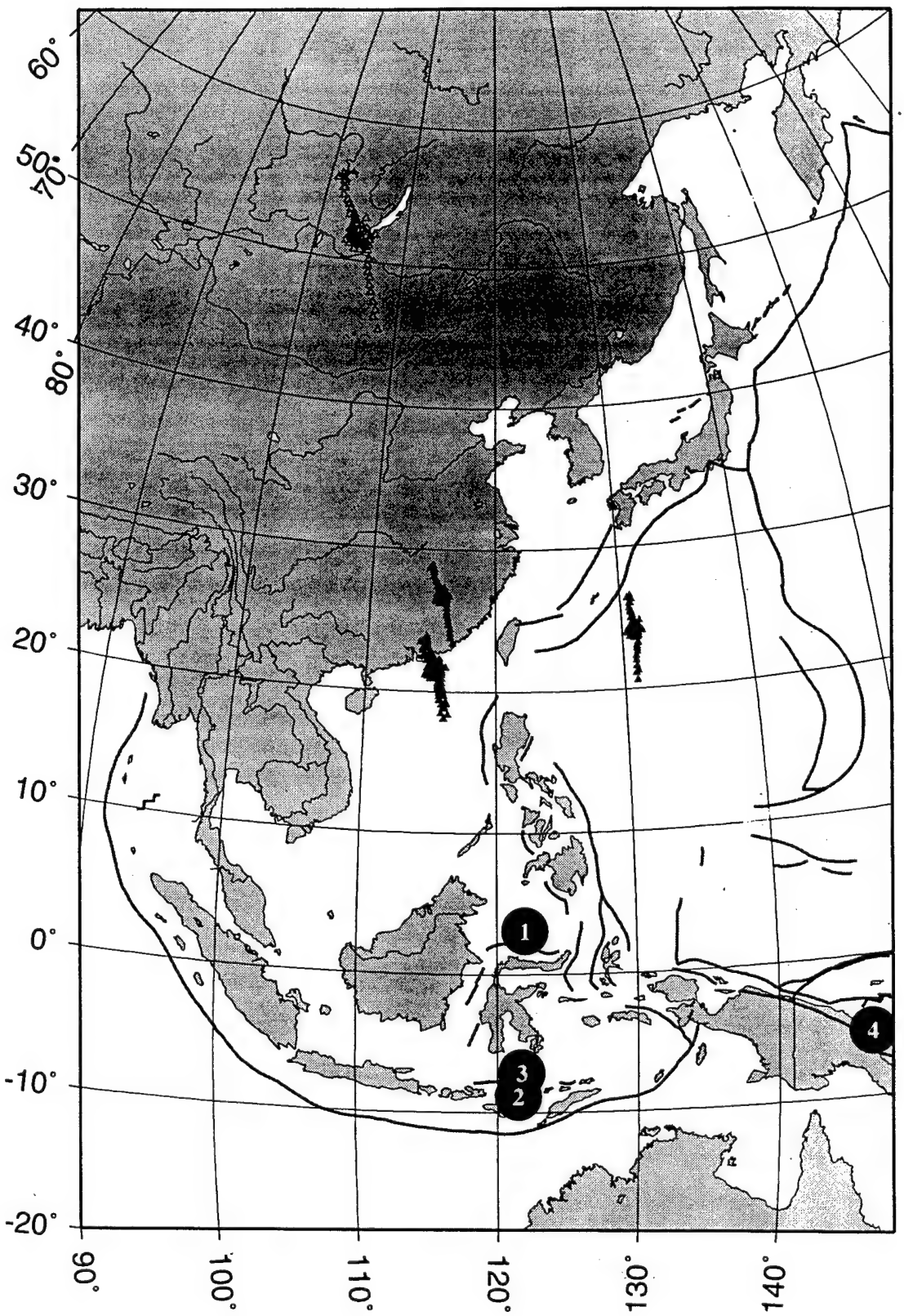

Figure 4.6

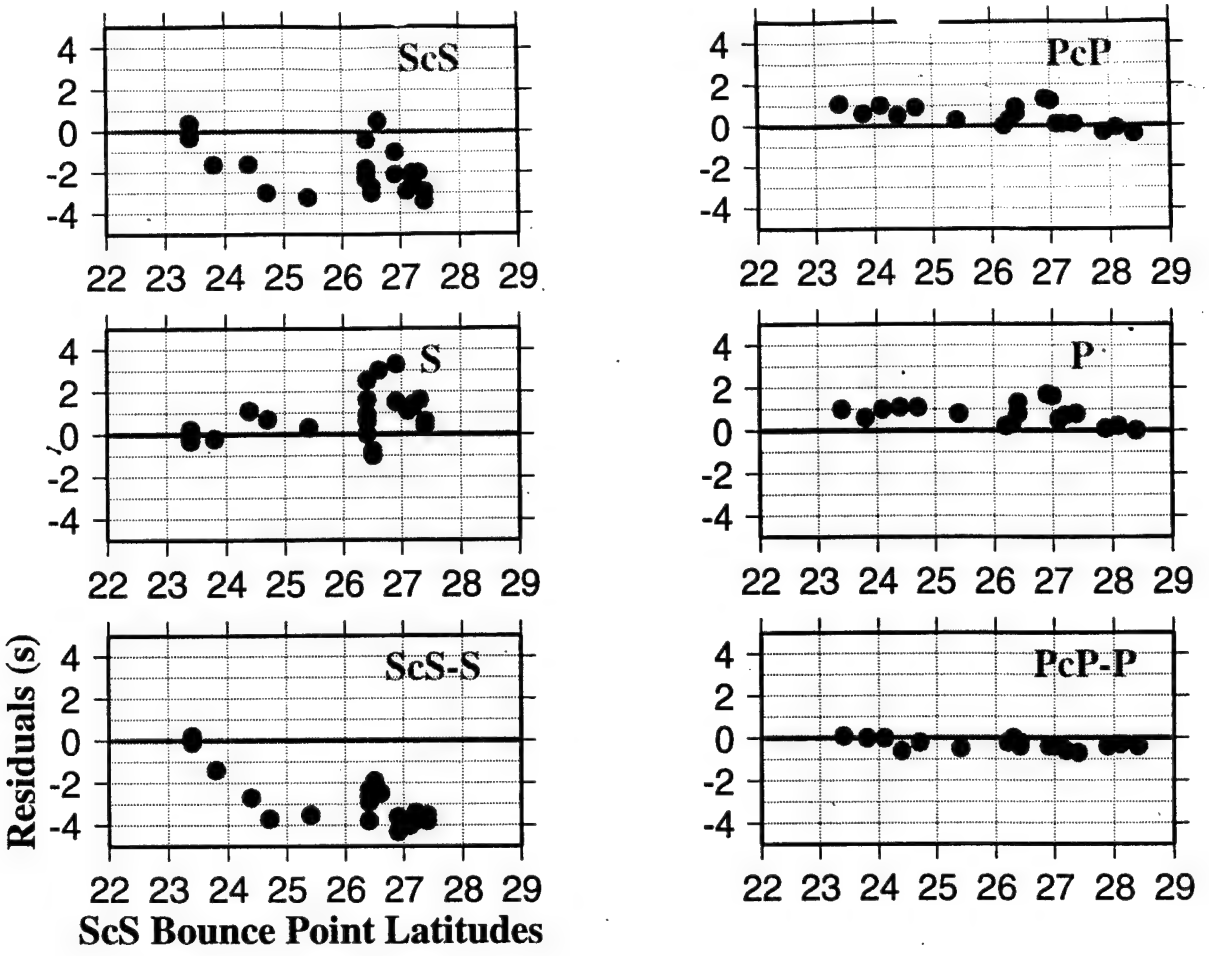
ScS
PcP
S
P
ScS-S
PcP-P
Residuals (s)
ScS Bounce Point Latitudes

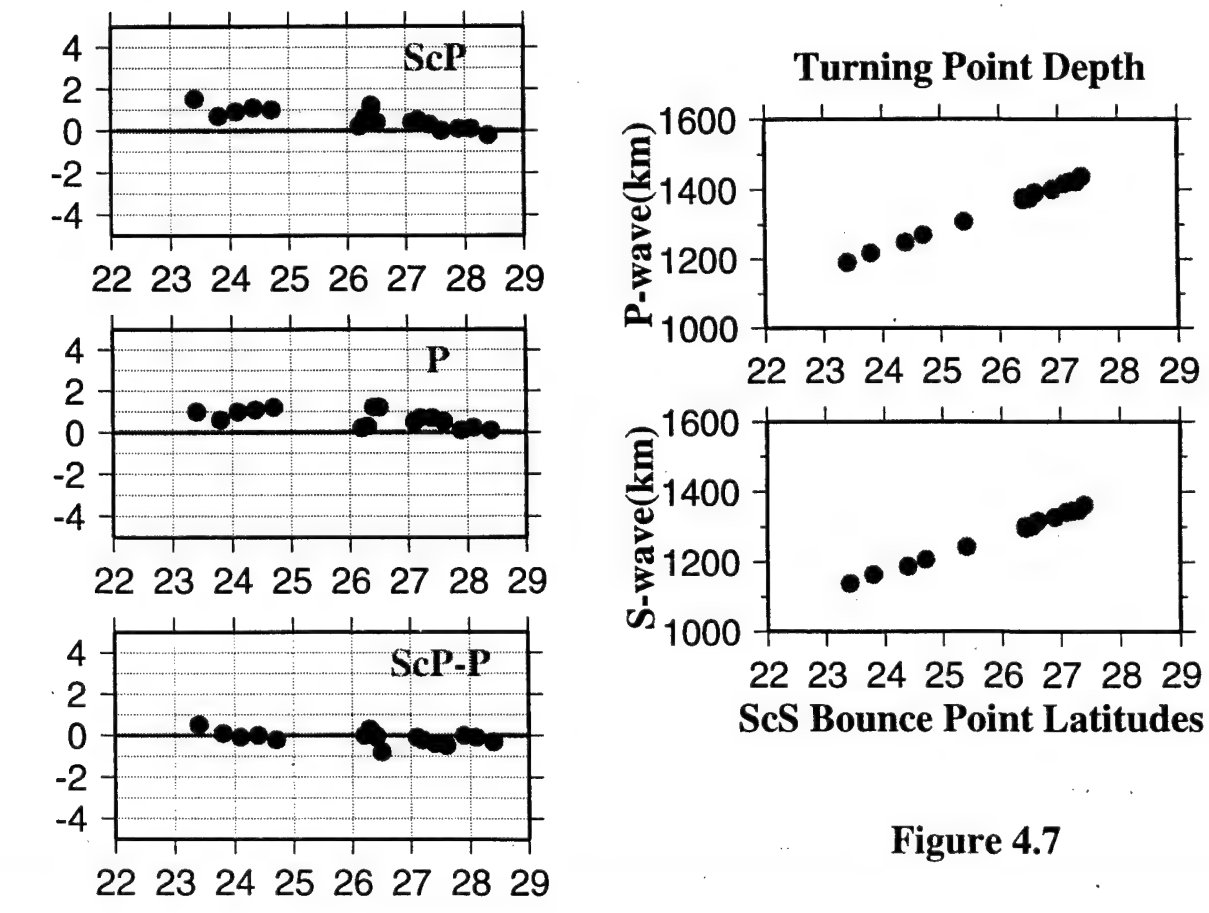
ScP
P
ScP-P
Turning Point Depth
P-wave(km)
S-wave(km)
ScS Bounce Point Latitudes

Figure 4.7

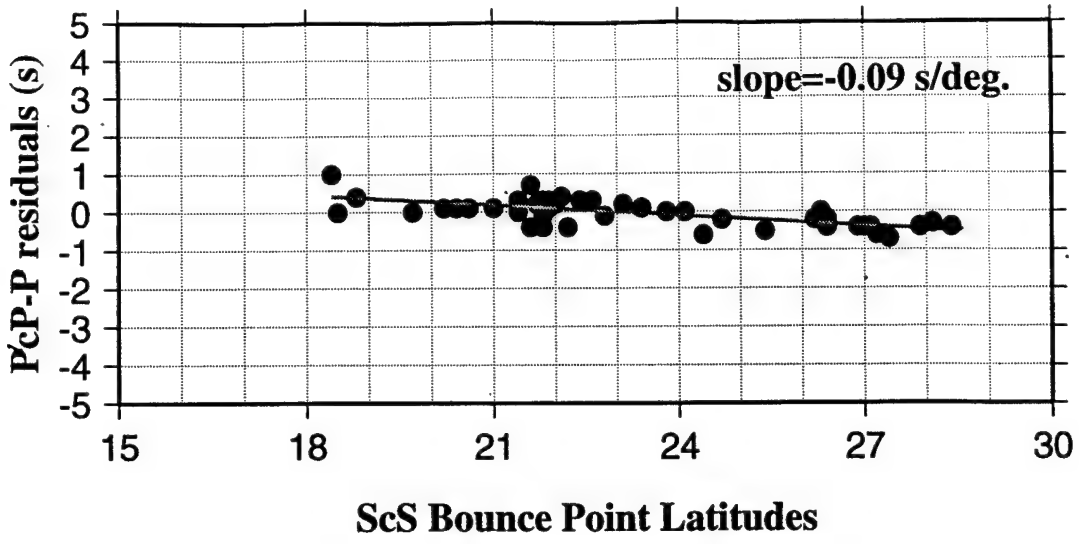
slope=-0.09 s/deg.
PcP-P residuals (s)
5
4
3
2
1
0
-1
-2
-3
-4
-5
15
18
21
24
27
30
ScS Bounce Point Latitudes

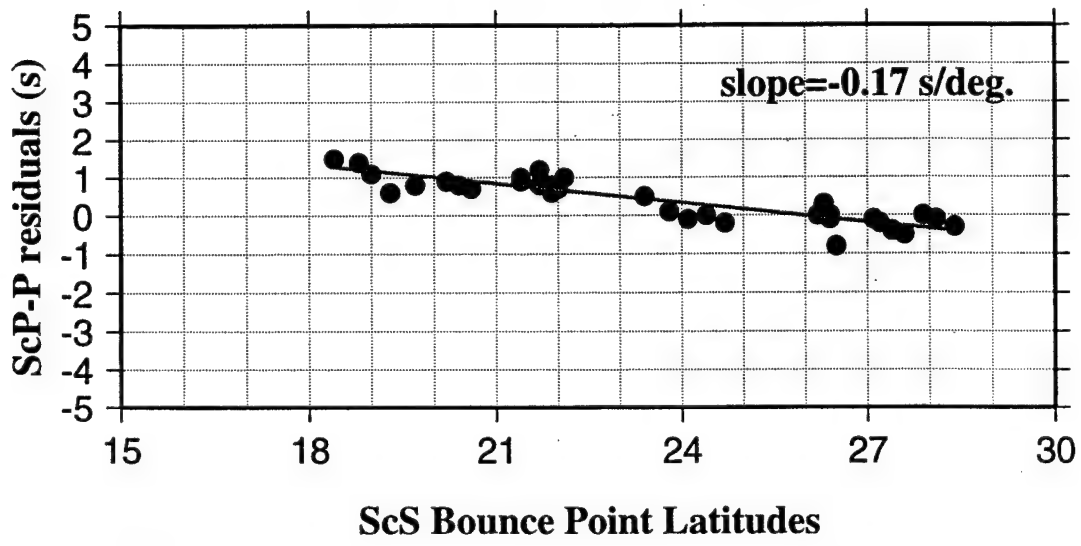
slope=-0.17 s/deg.
ScP-P residuals (s)
5
4
3
2
1
0
-1
-2
-3
-4
-5
15
18
21
24
27
30
ScS Bounce Point Latitudes

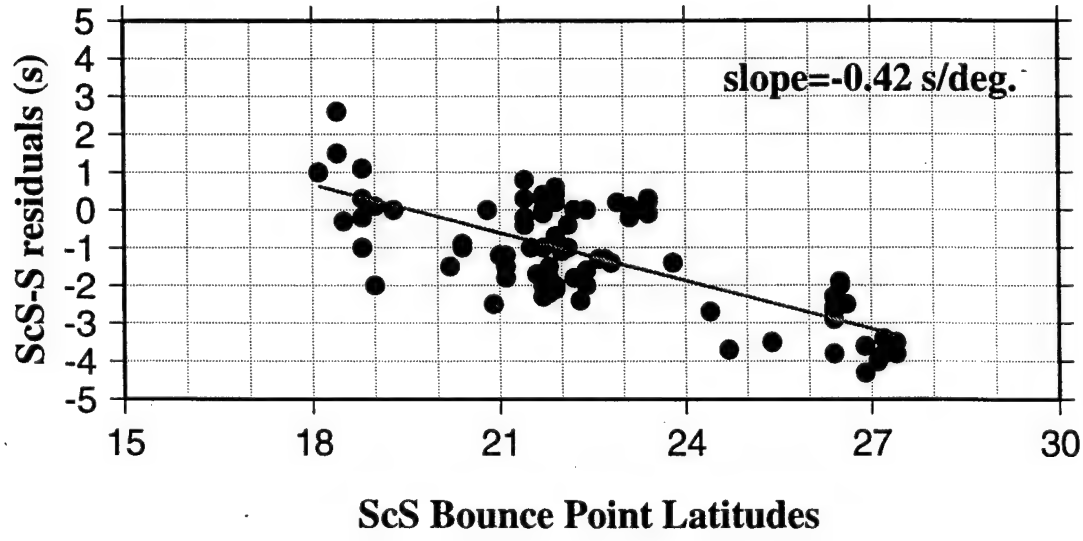
slope=-0.42 s/deg.
ScS-S residuals (s)
5
4
3
2
1
0
-1
-2
-3
-4
-5
15
18
21
24
27
30
ScS Bounce Point Latitudes

Figure 4.8

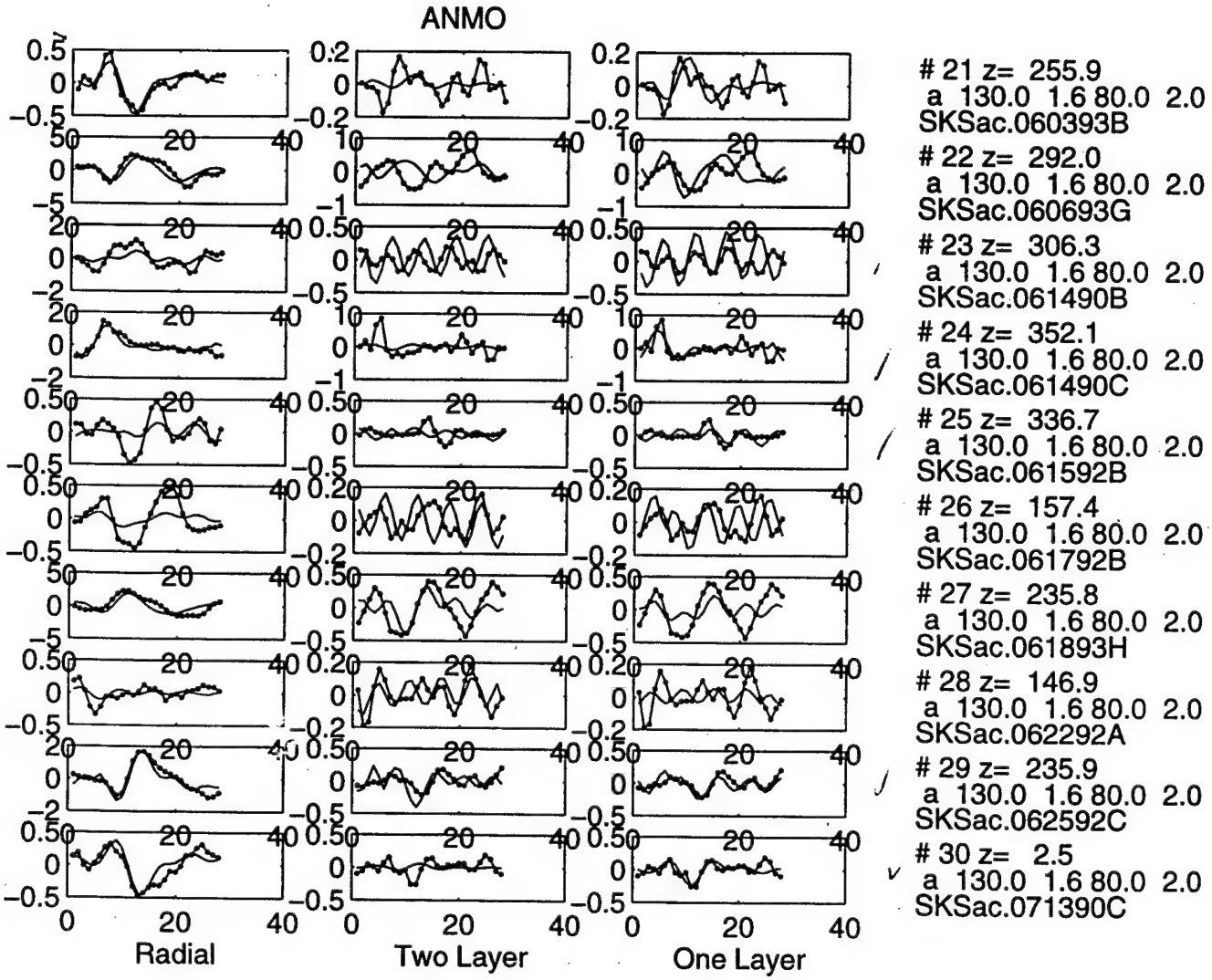

Figure 5.1: SKS waveforms (dotted lines) for GSN station ANMO compared to normal mode synthetics (smooth curves, Woodhouse, 1988). Radial seismograms are on the left. Azimuthal components modelled as a double layer of anisotropy are in the centre and as a single layer on the right. On the far right numbers give; event number, azimuth, fast directions (anticlockwise from north, and delay in seconds for the upper and lower layers, and CMT event name. Note events 21,23,24,29 and 30 are adequately described by a single layer of splitting. However event 27 and possibly 28 are better described by the double layer.

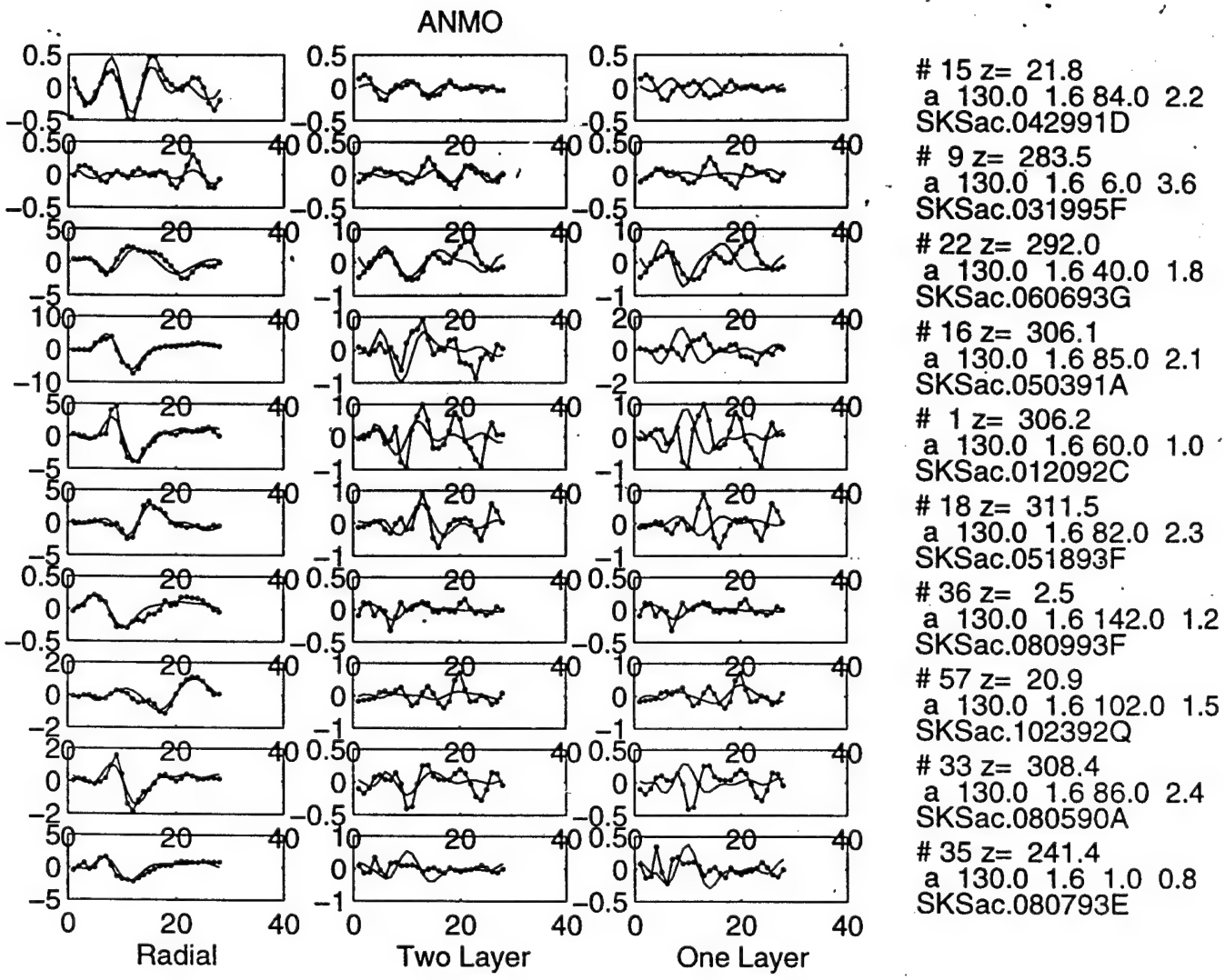

Figure 5.2: SKS waveforms from the 64 analysed at ANMO for which a 2 layer anisotropy is a good or better fit than one layer. The fact that the second layer parameters are different and incident rays close to these did not exhibit second layer effects leads us to believe these effects are coming from deep in the mantle; quite possibly in the D" region of the lowermost mantle.

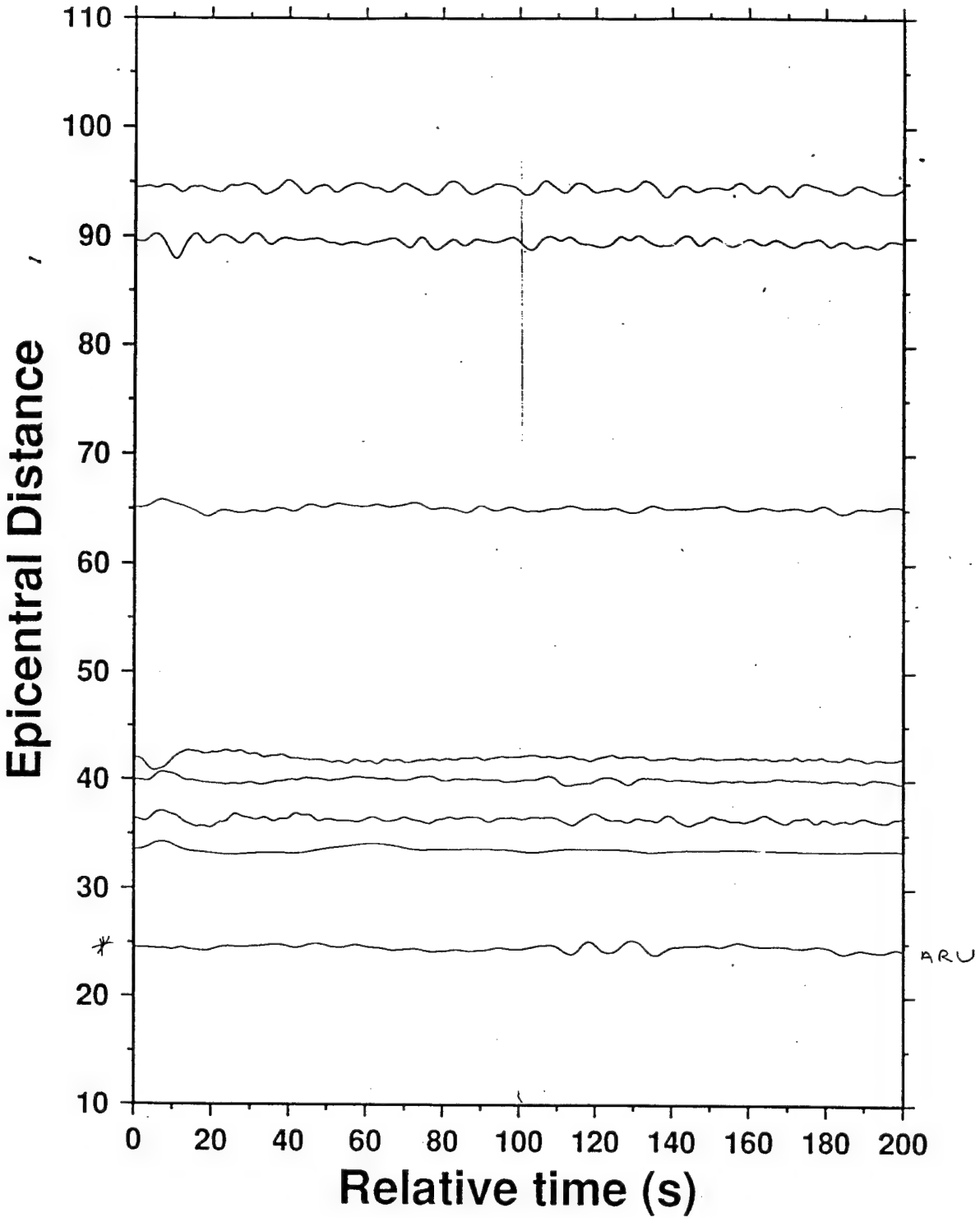

Figure 1. East component of seismograms for explosion 8/16/90 plotted according to epicentral distance. The seismograms had the mean removed and were band-pass filtered with corner frequencies of 0.01 Hz and 0.1 Hz. The line down the middle indicates the expected S wave arrival. A disturbance is noticeable at station ARU.

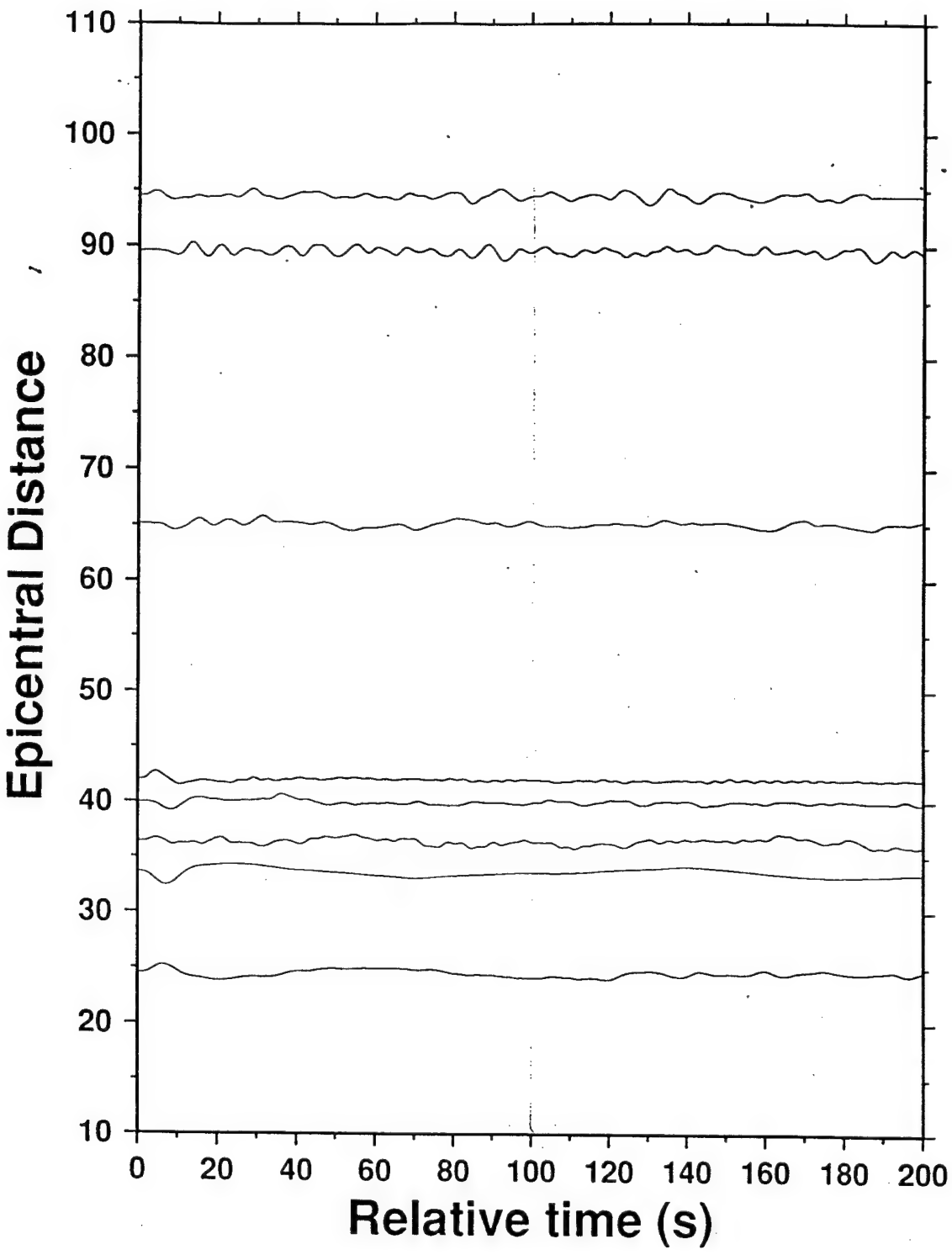

Figure 2. North component of seismograms for explosion 8/16/90 plotted according to epicentral distance. The seismograms had the mean removed and were band-pass filtered with corner frequencies of 0.01 Hz and 0.1 Hz. The line down the middle indicates the expected S wave arrival. No disturbances are noticeable.

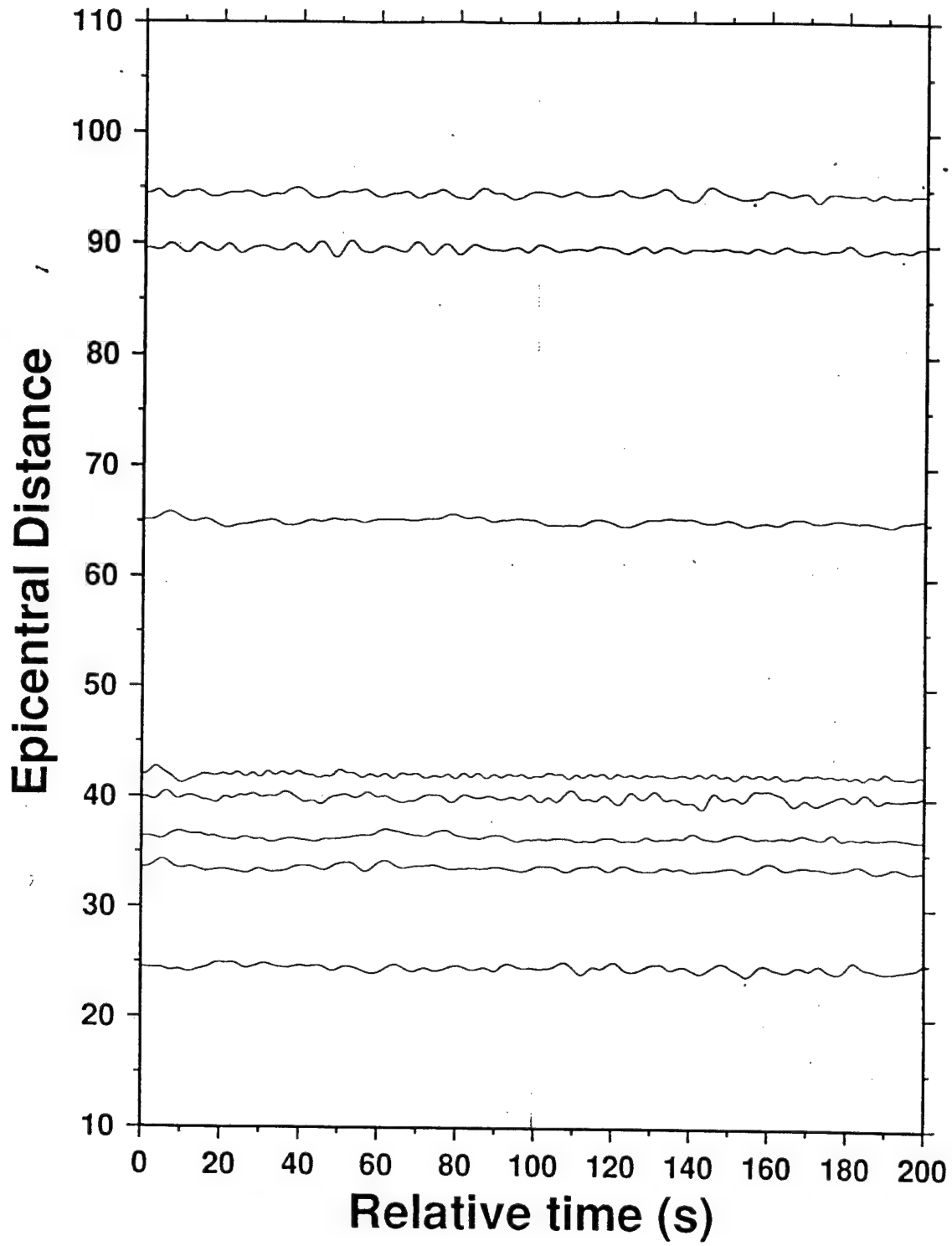

Figure 3. Vertical component of seismograms for explosion 8/16/90 plotted according to epicentral distance. The seismograms had the mean removed and were band-pass filtered with corner frequencies of 0.01 Hz and 0.1 Hz. The line down the middle indicates the expected S wave arrival. No disturbances are noticeable.

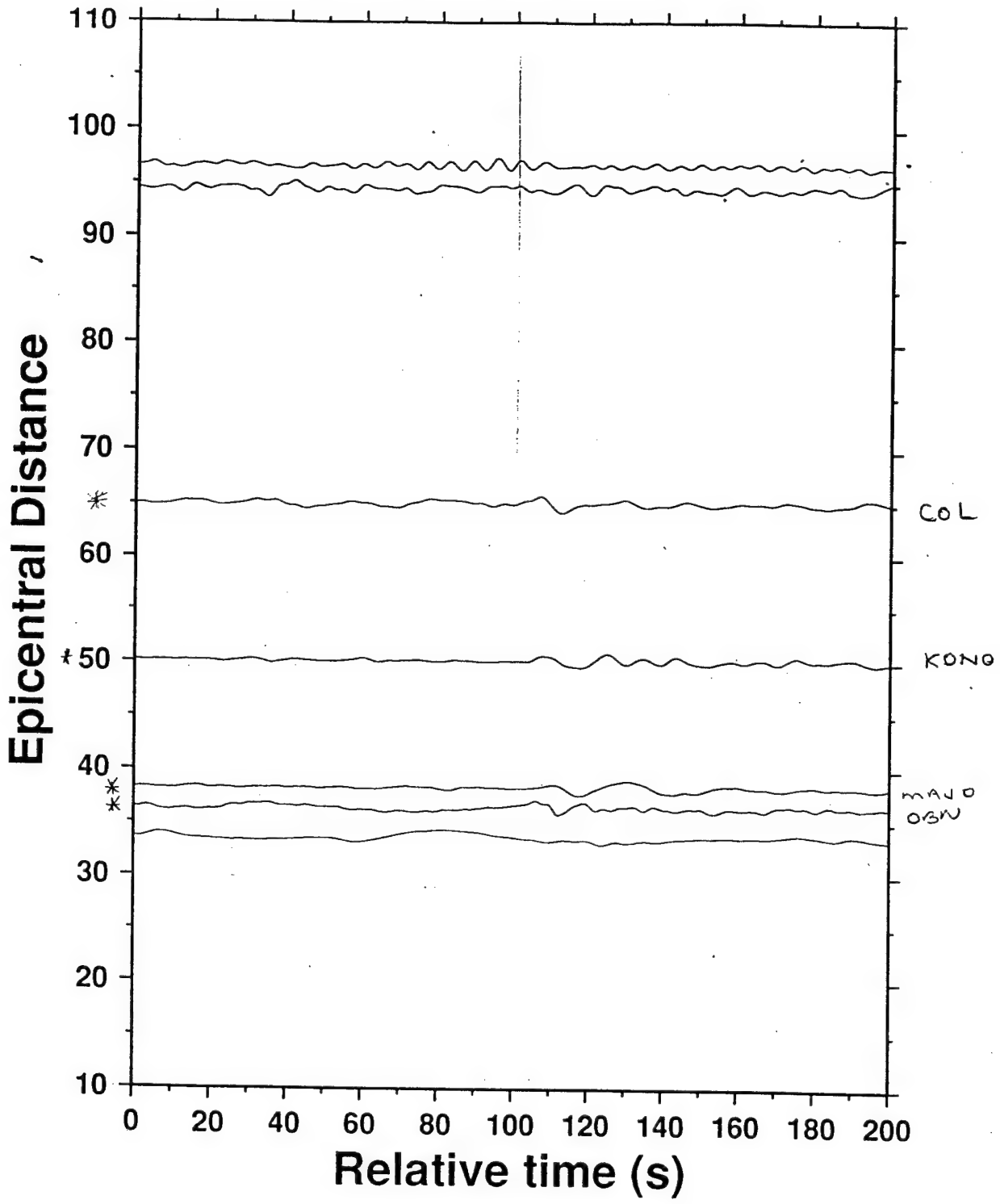

Figure 4. East component of seismograms for explosion 5/21/92 plotted according to epicentral distance. The seismograms had the mean removed and were band-pass filtered with corner frequencies of 0.01 Hz and 0.1 Hz. The line down the middle indicates the expected S wave arrival. A disturbance is noticeable at stations COL, KONO, MAJO, and OBN.

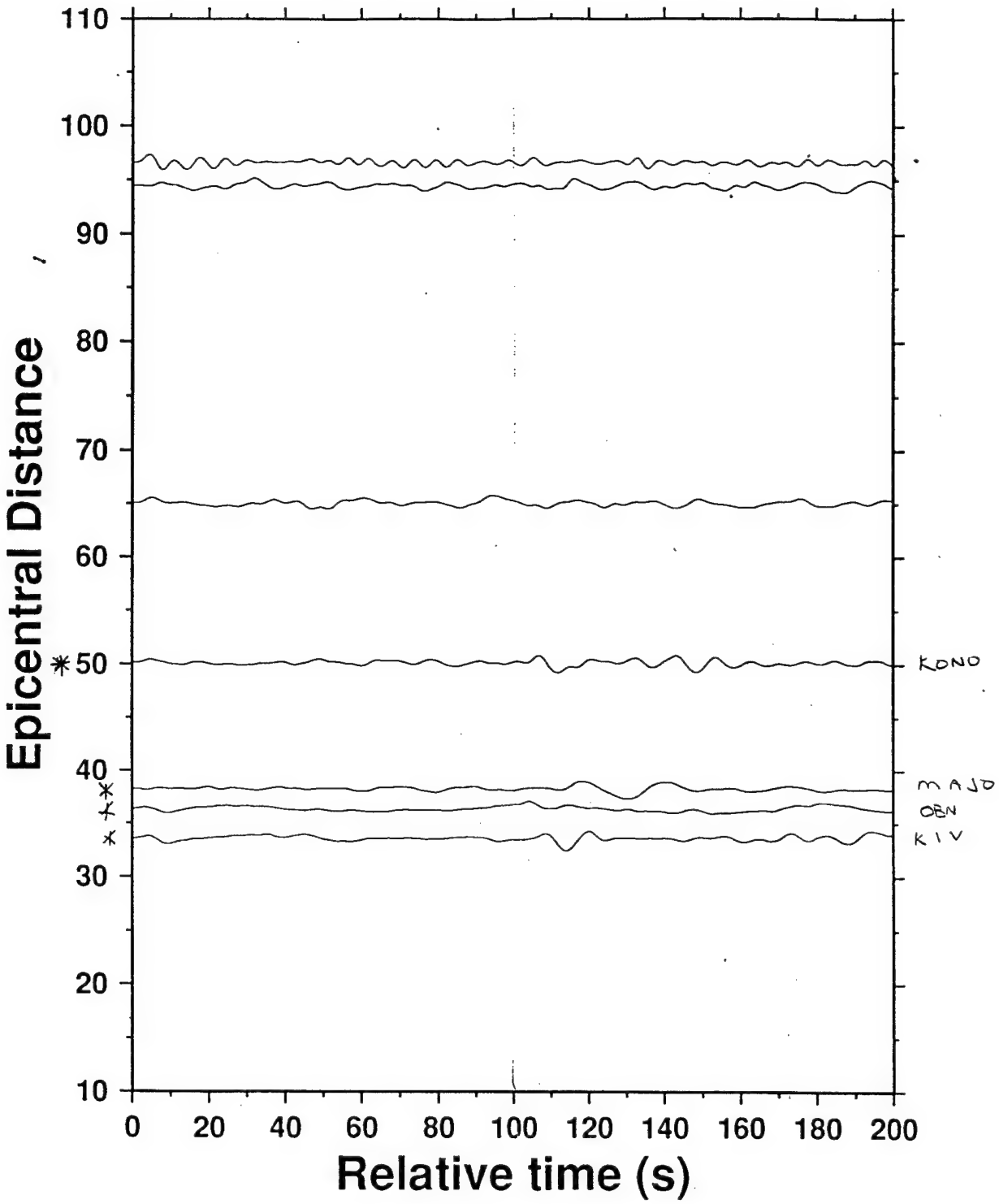

Figure 5. North component of seismograms for explosion 5/21/92 plotted according to epicentral distance. The seismograms had the mean removed and were band-pass filtered with corner frequencies of 0.01 Hz and 0.1 Hz. The line down the middle indicates the expected S wave arrival. A disturbance is noticeable at stations KONO, MAJO, and OBN, and KIV.

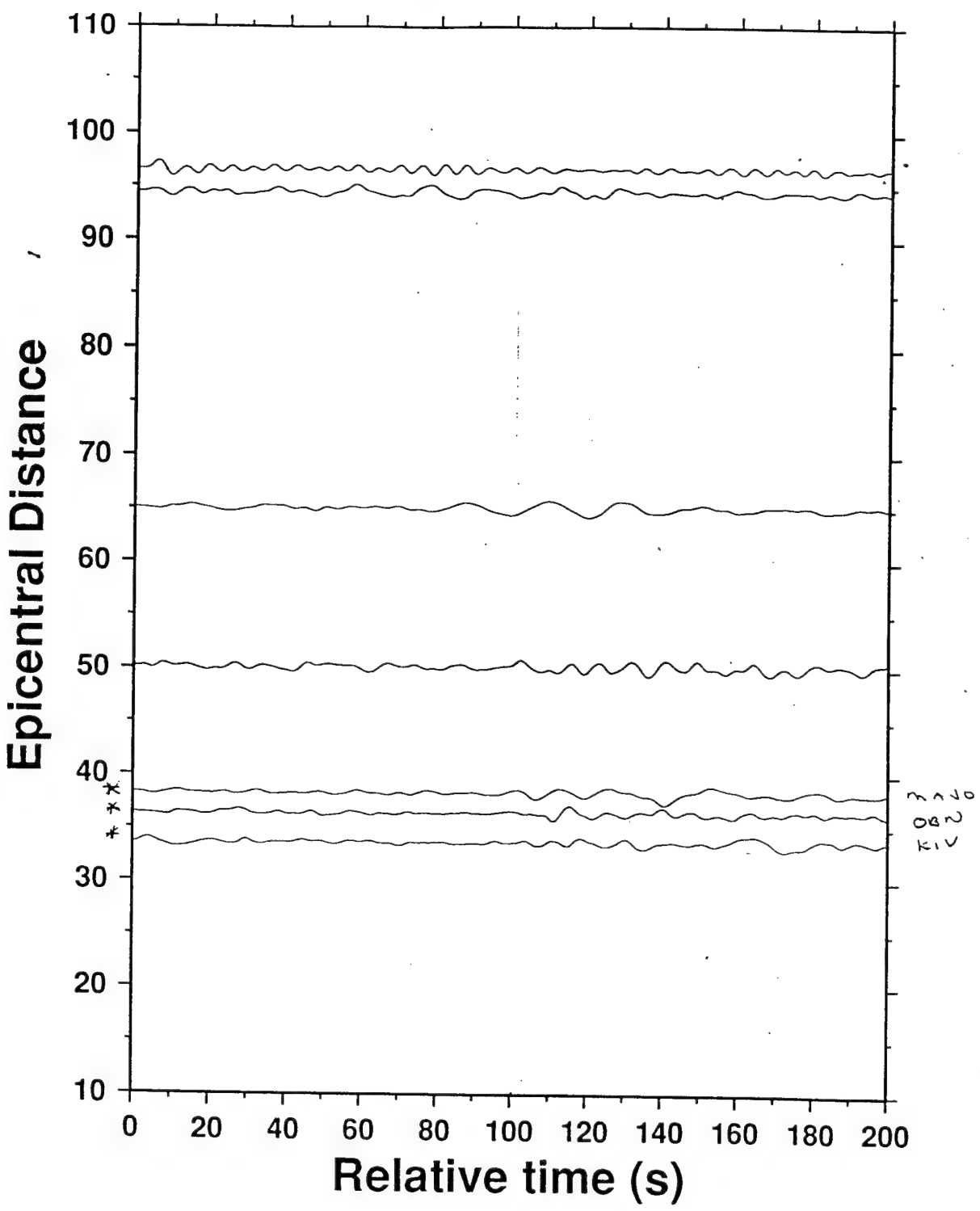

Figure 6. Vertical component of seismograms for explosion 5/21/92 plotted according to epicentral distance. The seismograms had the mean removed and were band-pass filtered with corner frequencies of 0.01 Hz and 0.1 Hz. The line down the middle indicates the expected S wave arrival. A disturbance is noticeable at stations MAJO, and OBN, and KIV.

Figure 6.6

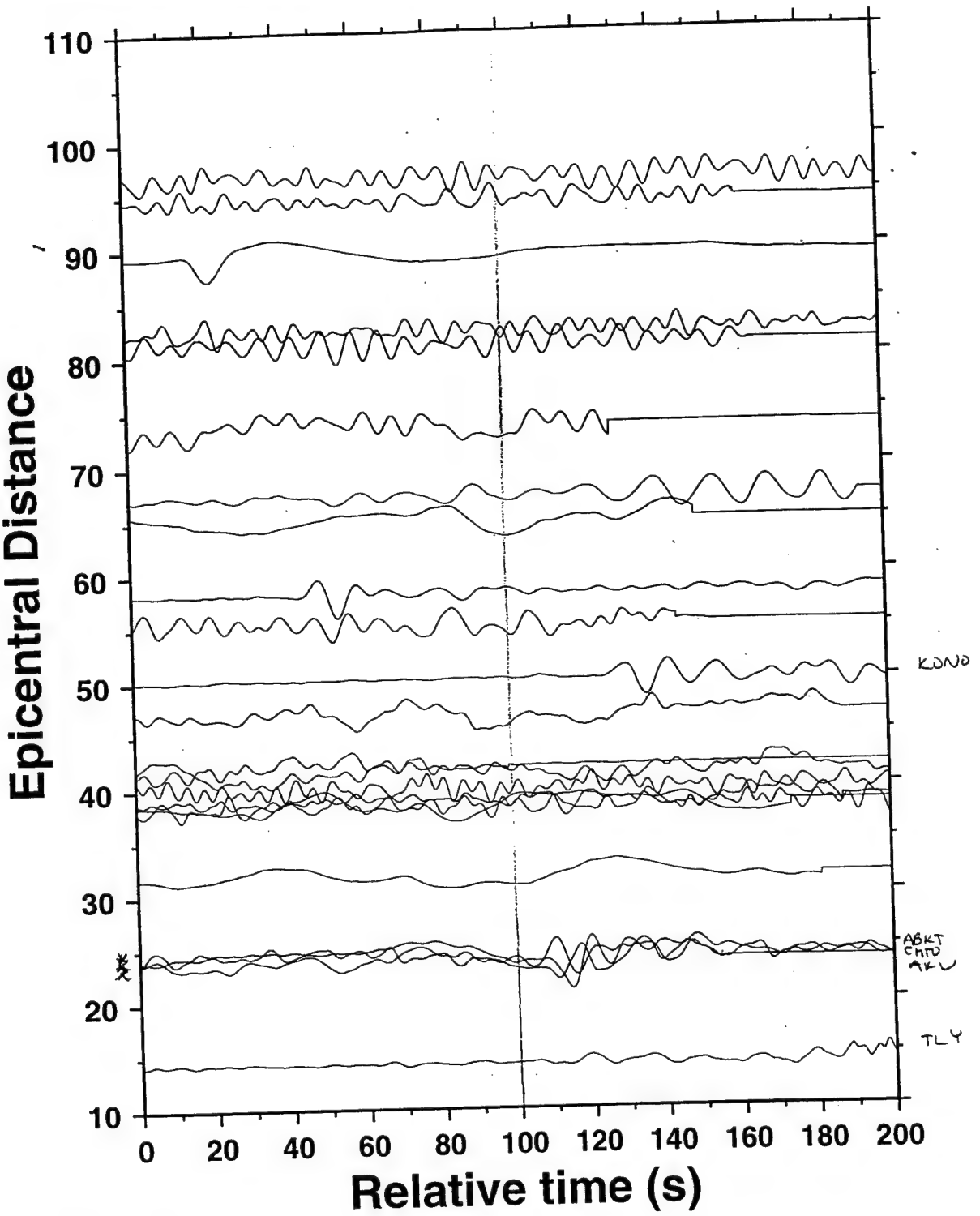

Figure 7. East component of seismograms for explosion 5/15/95 plotted according to epicentral distance. The seismograms had the mean removed and were band-pass filtered with corner frequencies of 0.01 Hz and 0.1 Hz. The line down the middle indicates the expected S wave arrival. A disturbance is noticeable at stations KONO, ABKT, CHTO, ARU, and TLY.

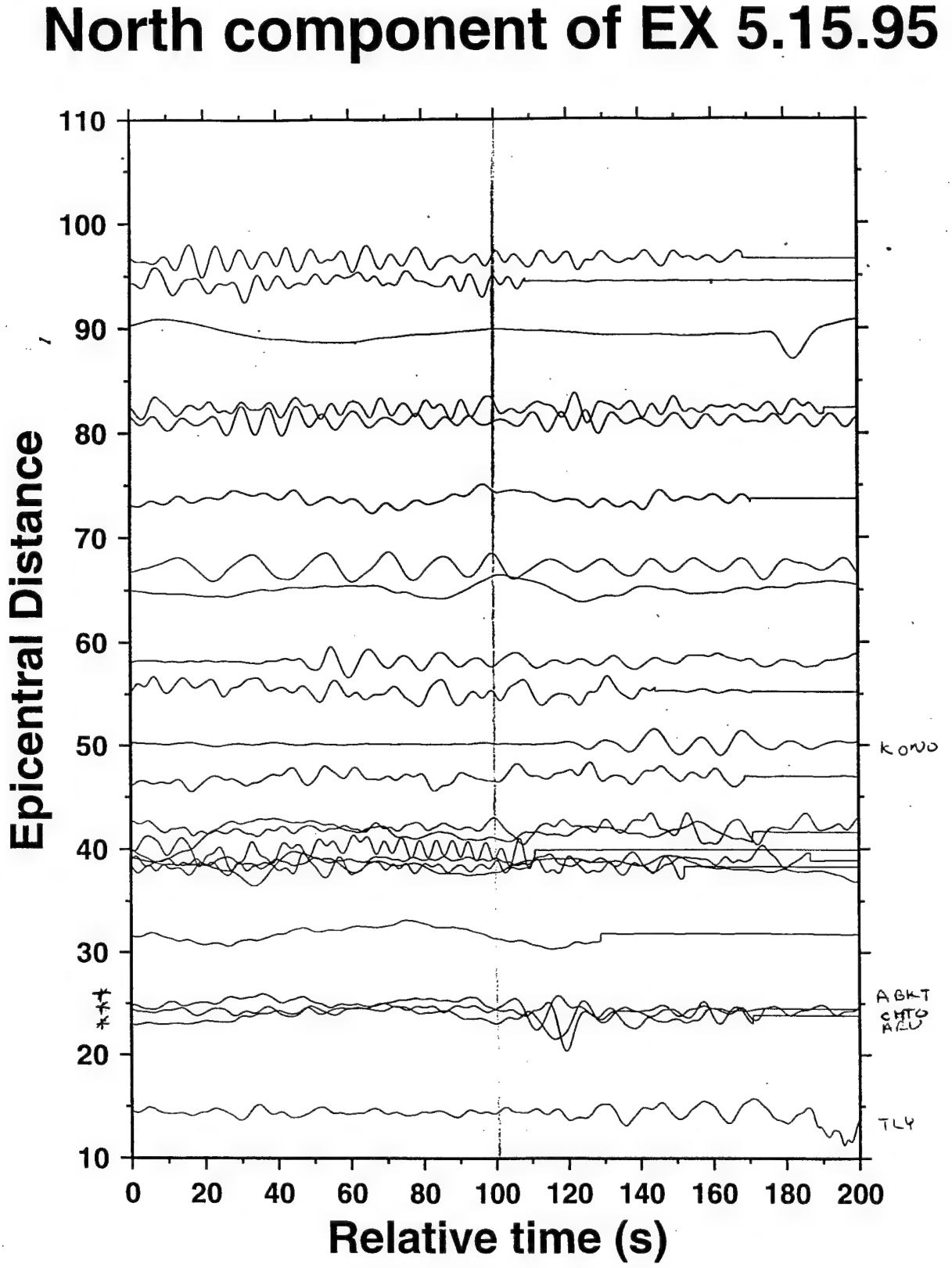

Figure 8. North component of seismograms for explosion 5/15/95 plotted according to epicentral distance. The seismograms had the mean removed and were band-pass filtered with corner frequencies of 0.01 Hz and 0.1 Hz. The line down the middle indicates the expected S wave arrival. A disturbance is noticeable at stations KONO, ABKT, CHTO, ARU, and TLY.

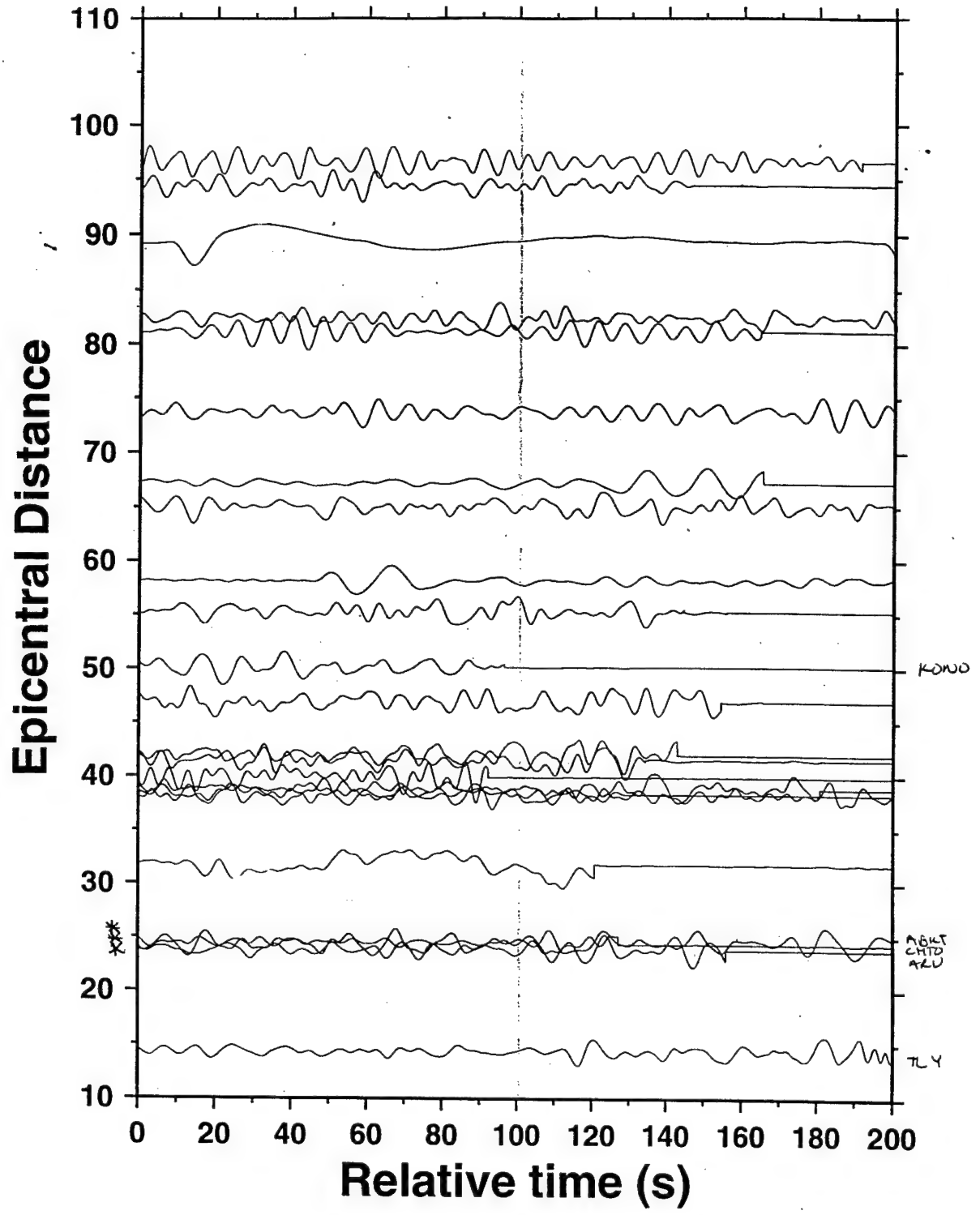

Figure 9. Vertical component of seismograms for explosion 5/15/95 plotted according to epicentral distance. The seismograms had the mean removed and were band-pass filtered with corner frequencies of 0.01 Hz and 0.1 Hz. The line down the middle indicates the expected S wave arrival. A disturbance is noticeable at stations KONO, ABKT, CHTO, ARU, and TLY.

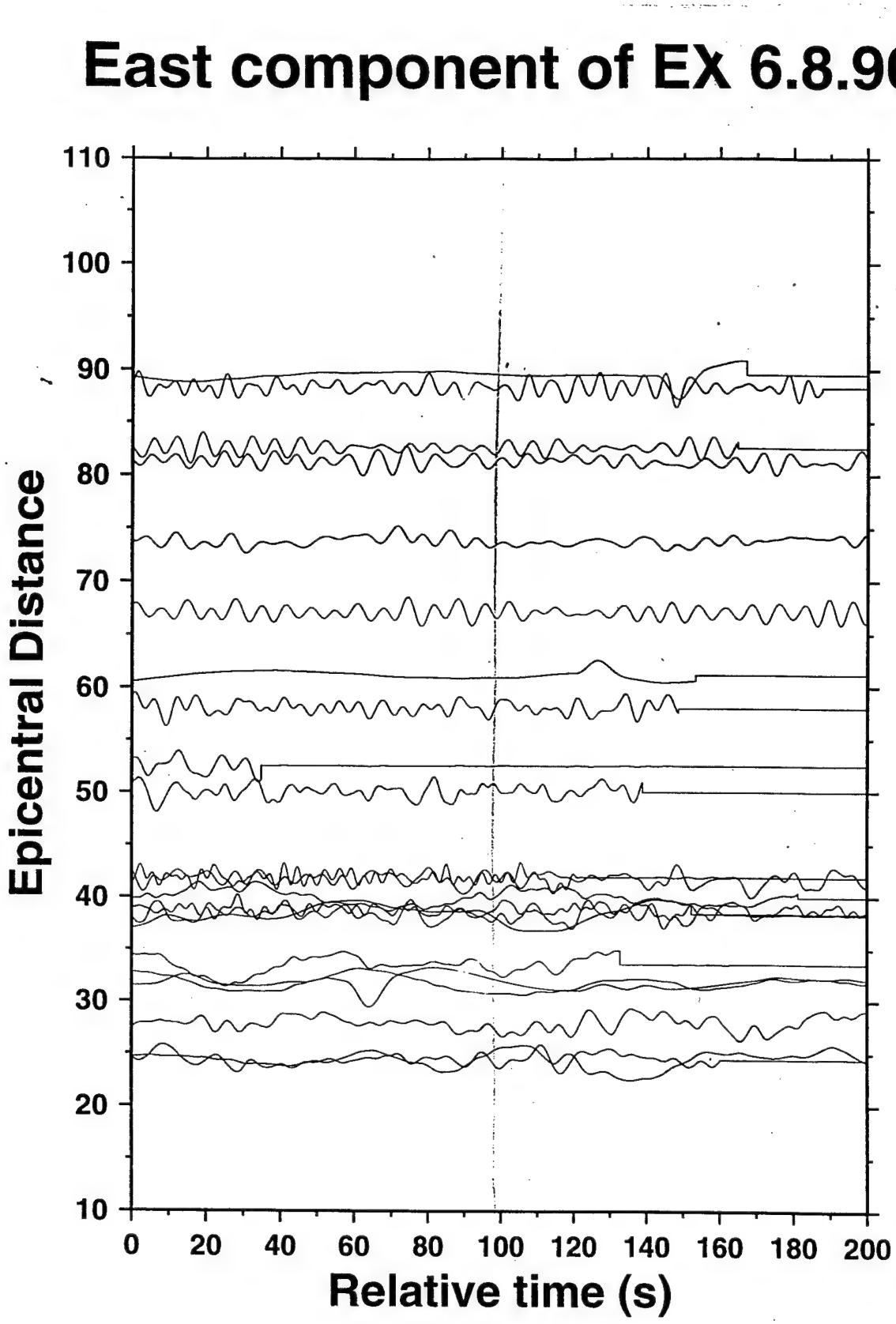

Figure 10. East component of seismograms for explosion 6/8/96 plotted according to epicentral distance. The seismograms had the mean removed and were band-pass filtered with corner frequencies of 0.01 Hz and 0.1 Hz. The line down the middle indicates the expected S wave arrival. No disturbances are noticeable.

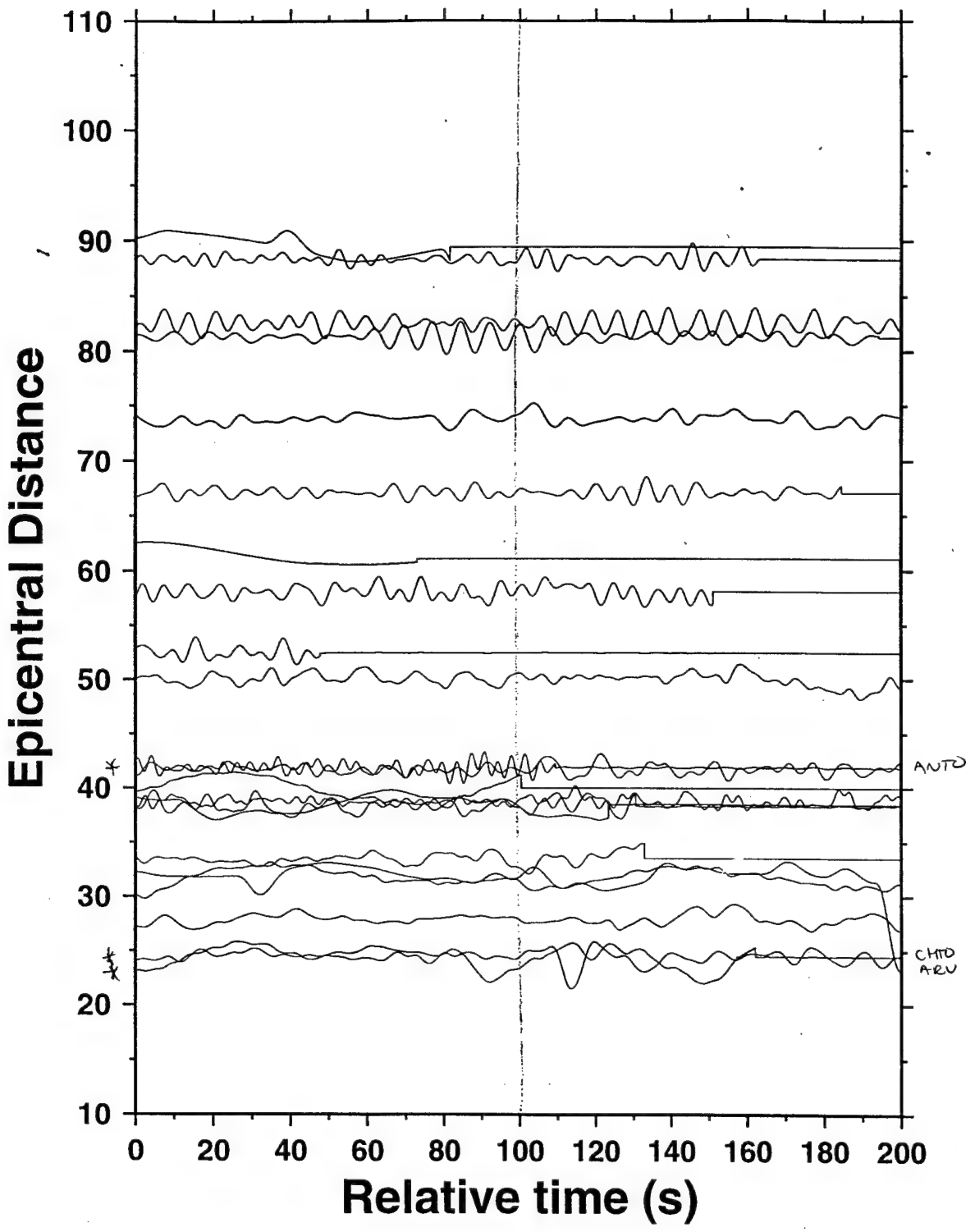

Figure 11. North component of seismograms for explosion 6/8/96 plotted according to epicentral distance. The seismograms had the mean removed and were band-pass filtered with corner frequencies of 0.01 Hz and 0.1 Hz. The line down the middle indicates the expected S wave arrival. A disturbances is noticeable at stations ANTO, CHTO, and ARU.

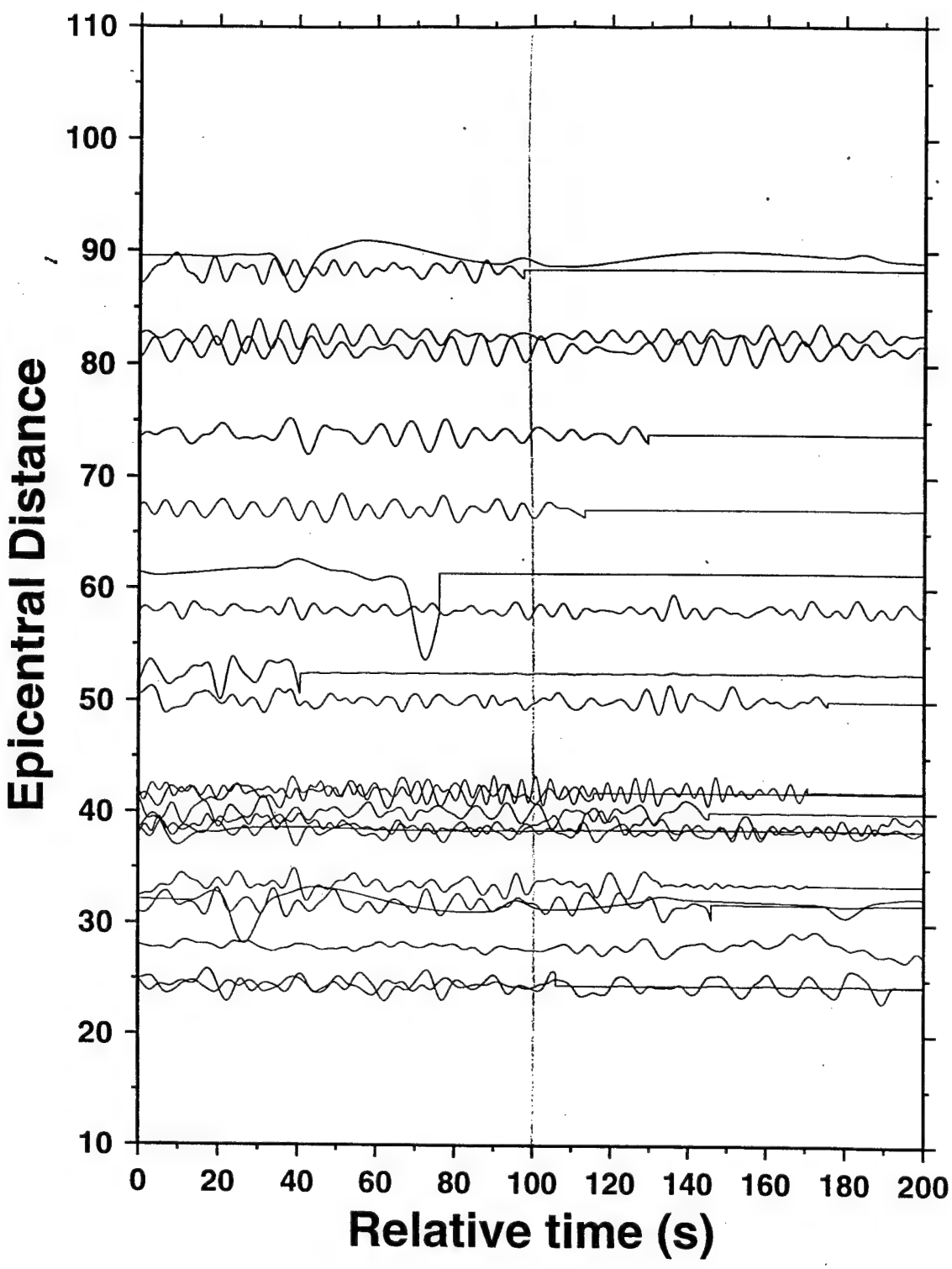

Figure 12. Vertical component of seismograms for explosion 6/8/96 plotted according to epicentral distance. The seismograms had the mean removed and were band-pass filtered with corner frequencies of 0.01 Hz and 0.1 Hz. The line down the middle indicates the expected S wave arrival. No disturbances are noticeable.

Figure 6.13

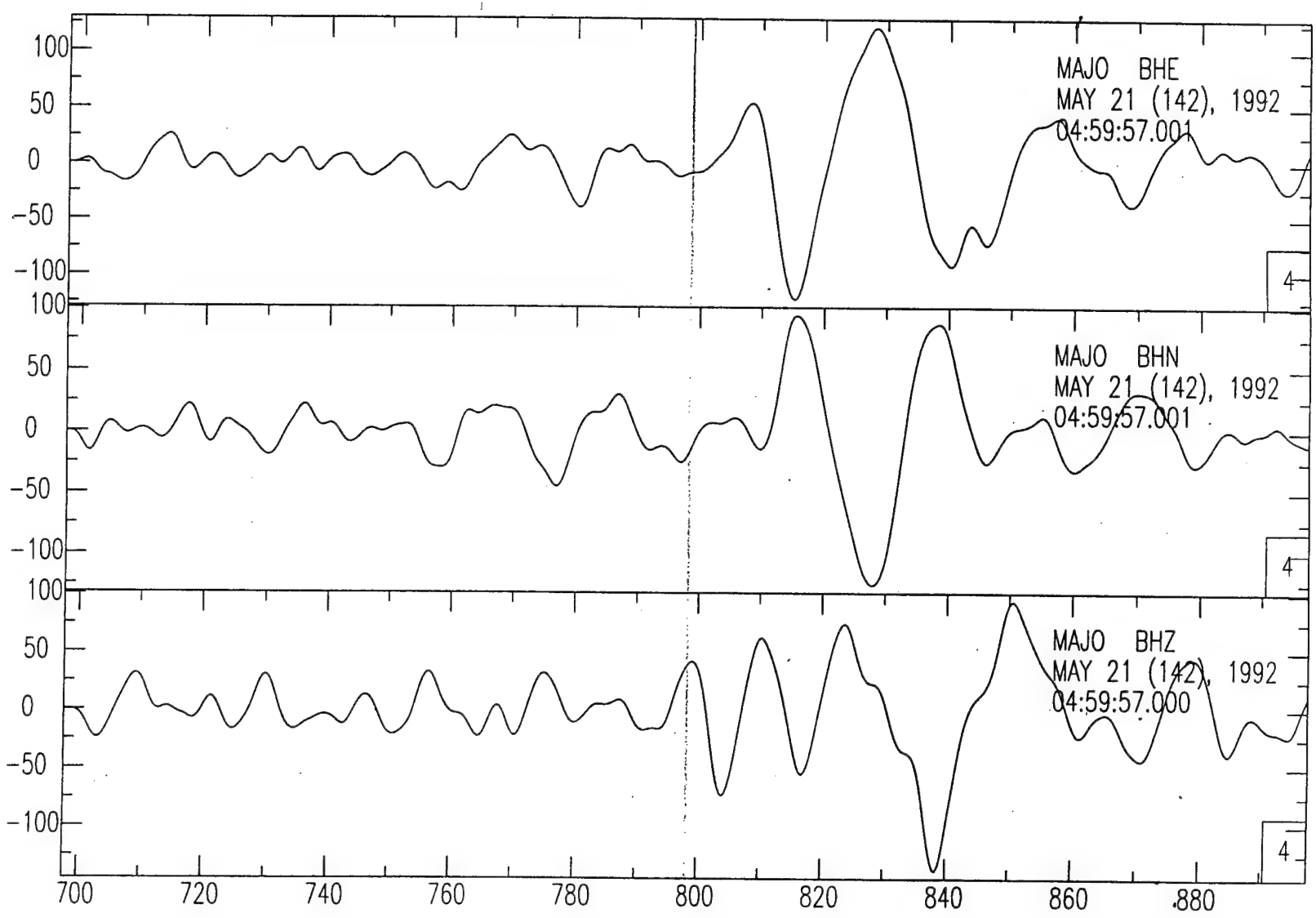

Figure 13. East, north, and vertical components of explosion 5/21/92 recorded at MAJO. The mean was removed from the seismogram and it was band-pass filtered with corner frequencies of 0.01 Hz and 0.1 Hz. This filter may have combined the S and PcS phases. The vertical line indicates the expected S wave arrival. The bottom axis is the time after the arrival in seconds.

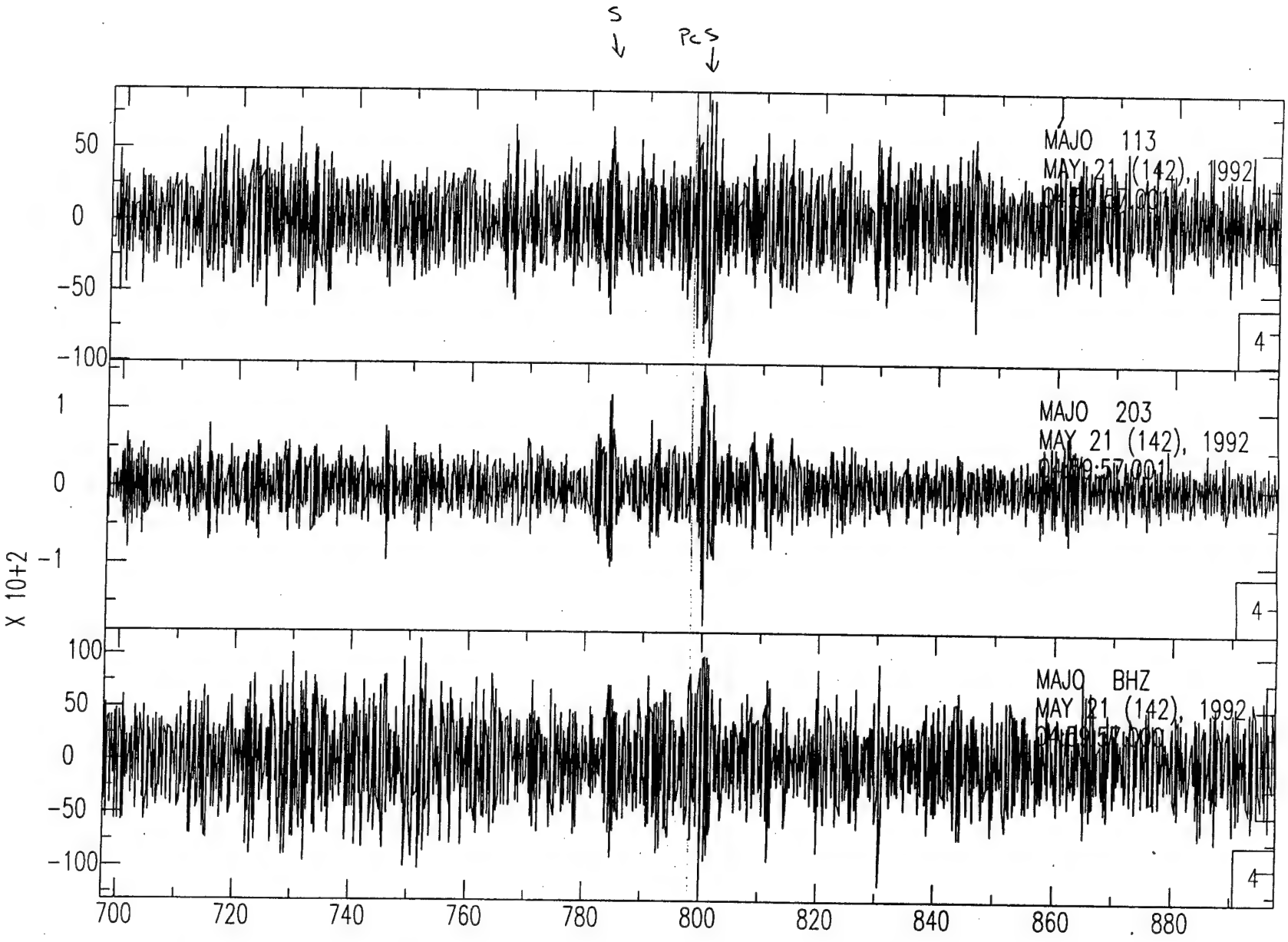

Figure 6.14

Figure 14. Radial, tangential, and vertical components of explosion 5/21/92 recorded at MAJO. The mean was removed from the seismogram and it was high-pass filtered with a corner frequency of 2 Hz. The two marked phases indicate the possible S and PcS arrivals. The vertical line indicates the expected S wave arrival. The bottom axis is the time after the arrival in seconds.

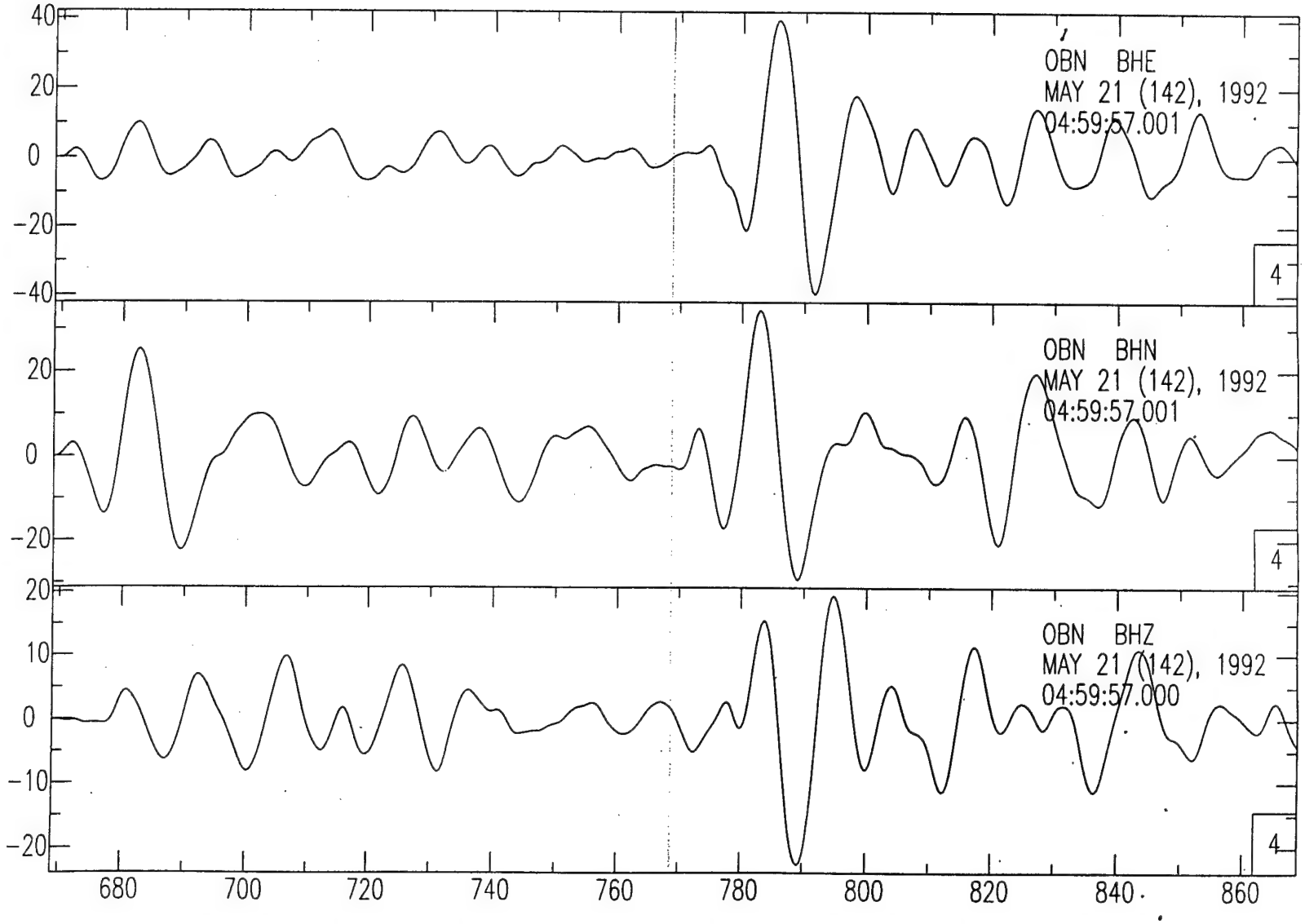

Figure 6.15

Figure 15. East, north, and vertical components of explosion 5/21/92 recorded at OBN. The means was removed from the seismogram and it was band-pass filtered with corner frequencies of 0.04 Hz and 0.1 Hz. This filter may have combined the S and PcS phases. The vertical line indicates the expected S wave arrival. The bottom axis is the time after the arrival in seconds.

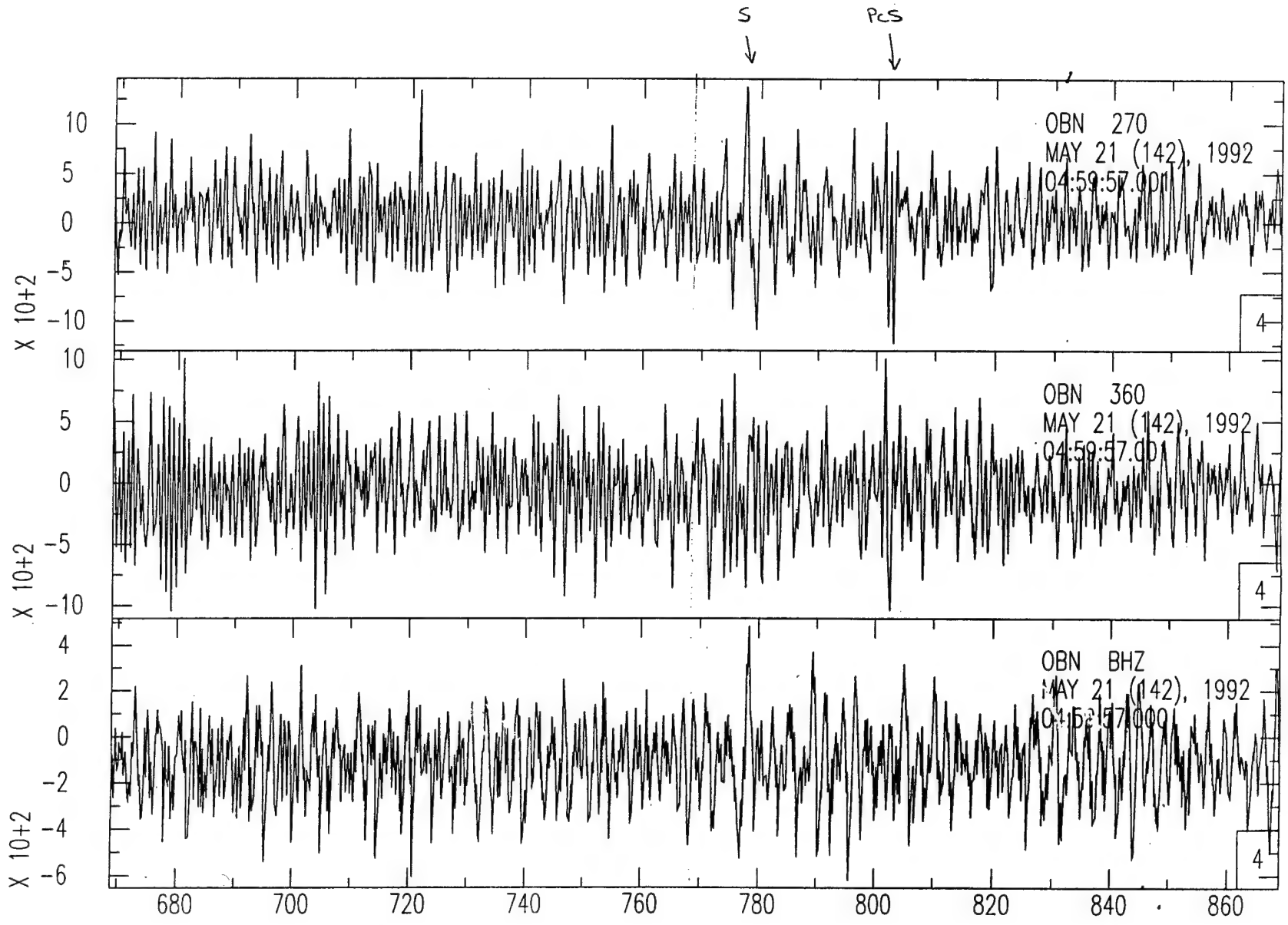

Figure 16. Radial, tangential, and vertical components of explosion 5/21/92 recorded at OBN. The mean was not removed and no filter was applied. The two marked phases indicate the possible S and PcS arrivals. The vertical line indicates the expected S wave arrival. The bottom axis is the time after the arrival in seconds.

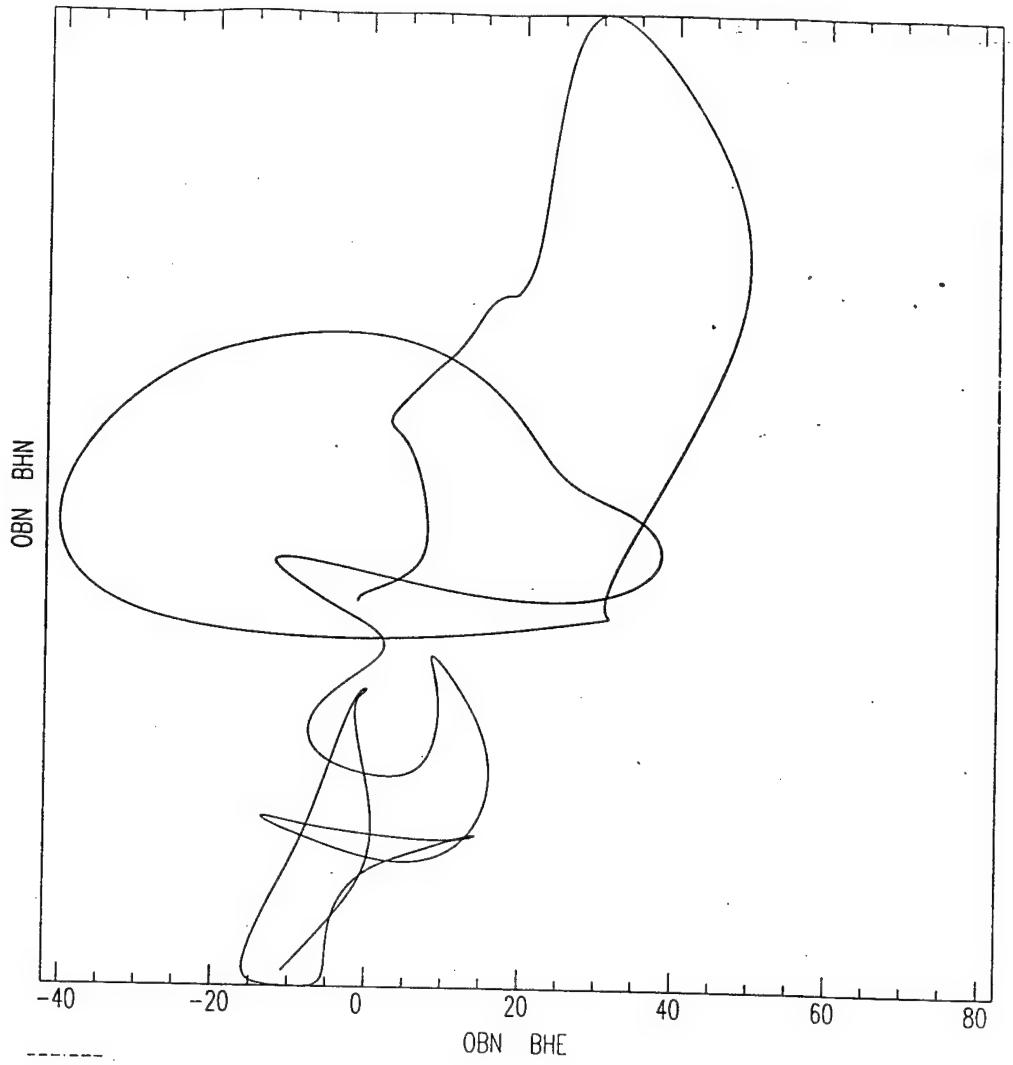

Figure 17. North-south/East-west particle motion of the expected S wave of explosion 5/21/92 recorded at OBN. An elliptical shape would indicate anisotropy. There appears to be none for this phase.

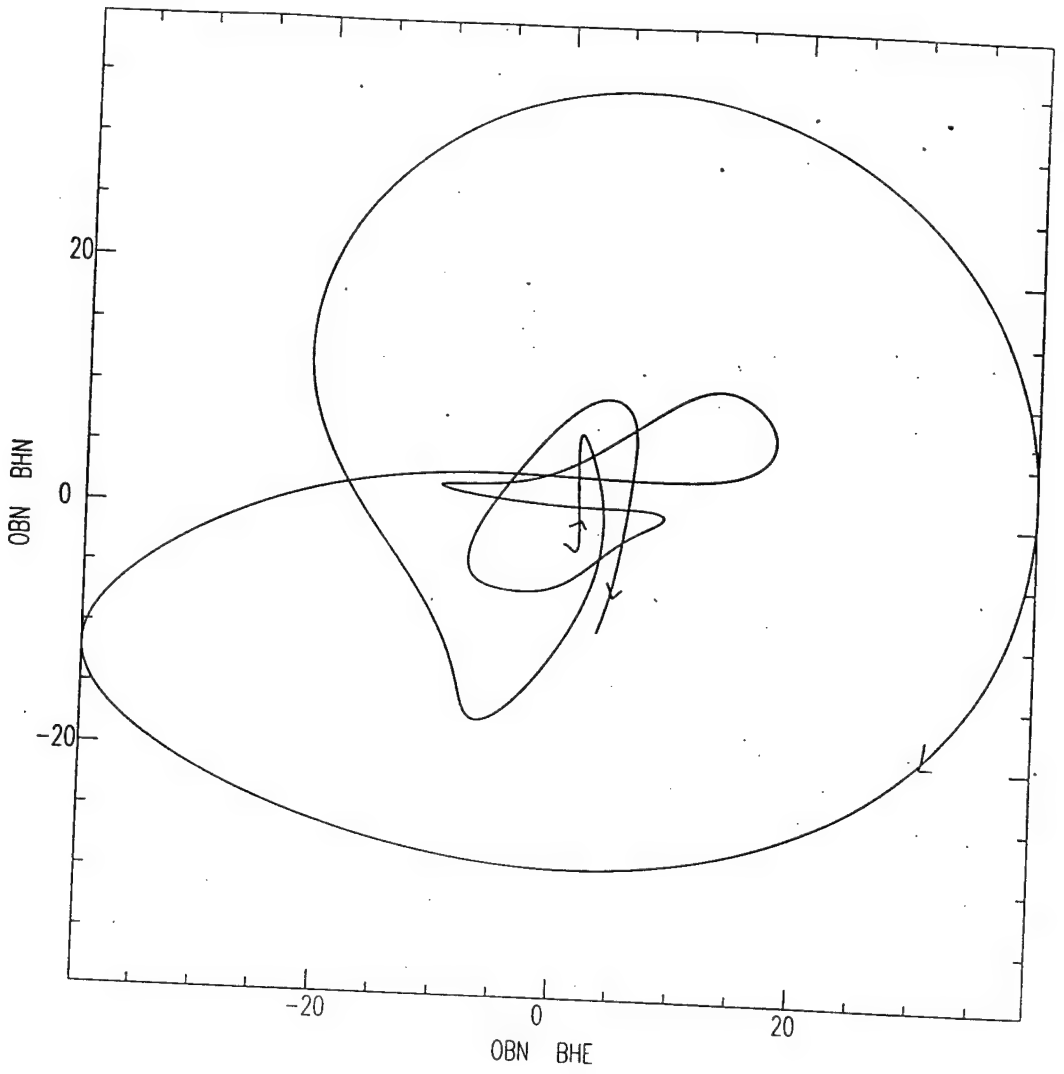

Figure 18. North-south/East-west particle motion of the expected PcS wave of explosion 5/21/92 recorded at OBN. An elliptical shape would indicate anisotropy. The elliptical shape shows there may be some for this phase.

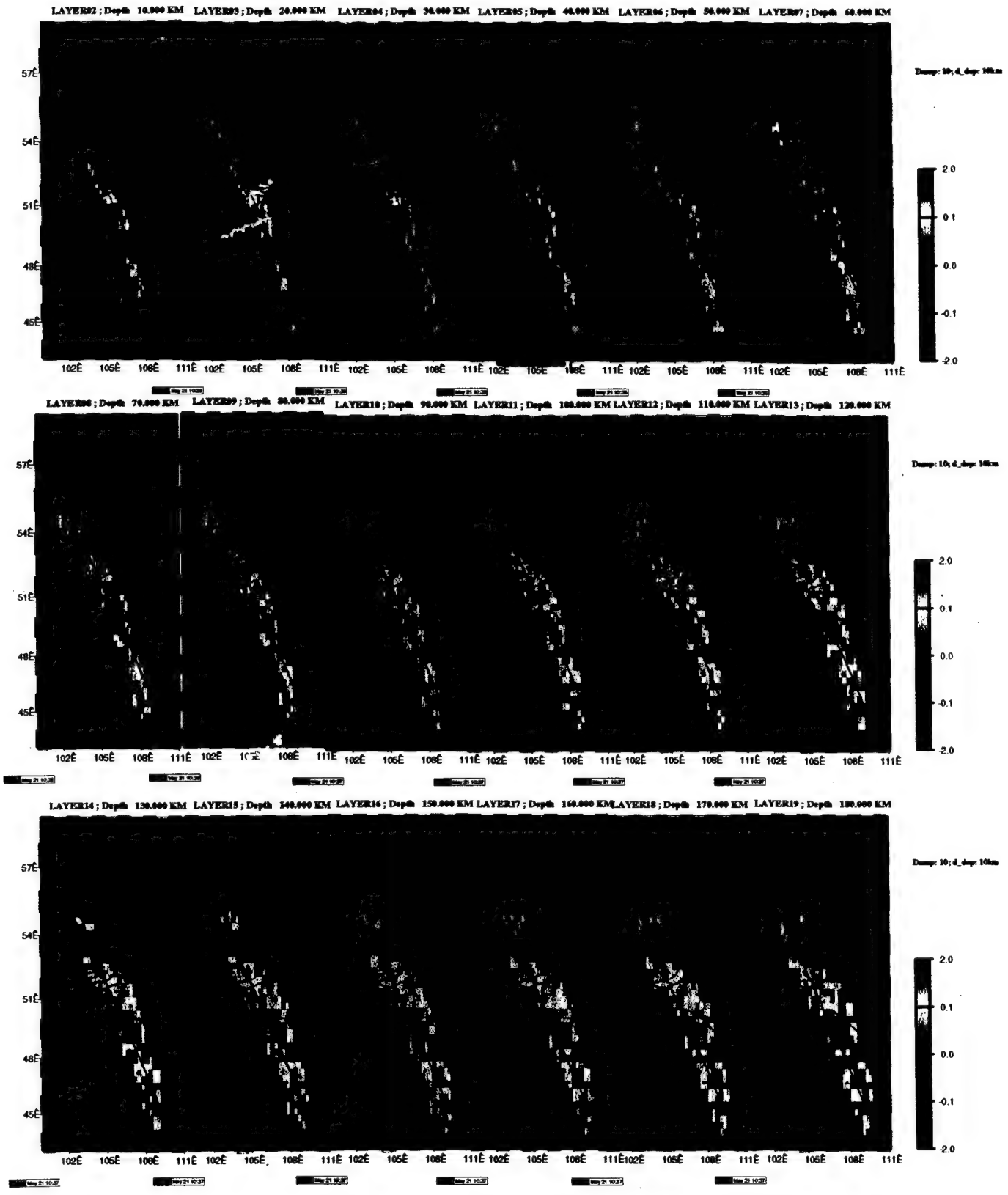
LAYER02 ; Depth 10.000 KM LAYER03 ; Depth 20.000 KM LAYER04 ; Depth 30.000 KM LAYER05 ; Depth 40.000 KM LAYER06 ; Depth 50.000 KM LAYER07 ; Depth 60.000 KM
LAYER08 ; Depth 70.000 KM LAYER09 ; Depth 80.000 KM LAYER10 ; Depth 90.000 KM LAYER11 ; Depth 100.000 KM LAYER12 ; Depth 110.000 KM LAYER13 ; Depth 120.000 KM
LAYER14 ; Depth 130.000 KM LAYER15 ; Depth 140.000 KM LAYER16 ; Depth 150.000 KM LAYER17 ; Depth 160.000 KM LAYER18 ; Depth 170.000 KM LAYER19 ; Depth 180.000 KM
57É
54É
51É
48É
45É
102É 105É 108É 111É
2.0
0.1
0.0
-0.1
-2.0

Figure 7.1

Damping Fac: 10.0; Min_No. Rays: 10; No. of inversion: 1
N_lat: 50; N_lon: 40; N_dep: 20
Lat range: 43 59; Lon range: 100 112; Dep range: 0 200
d_lat: 35.6; d_lon: 33.4; d_dep: 10.0 km

rms travel time residual (sec)= 0.18900

Vp range:-2.78935 to 6.36375

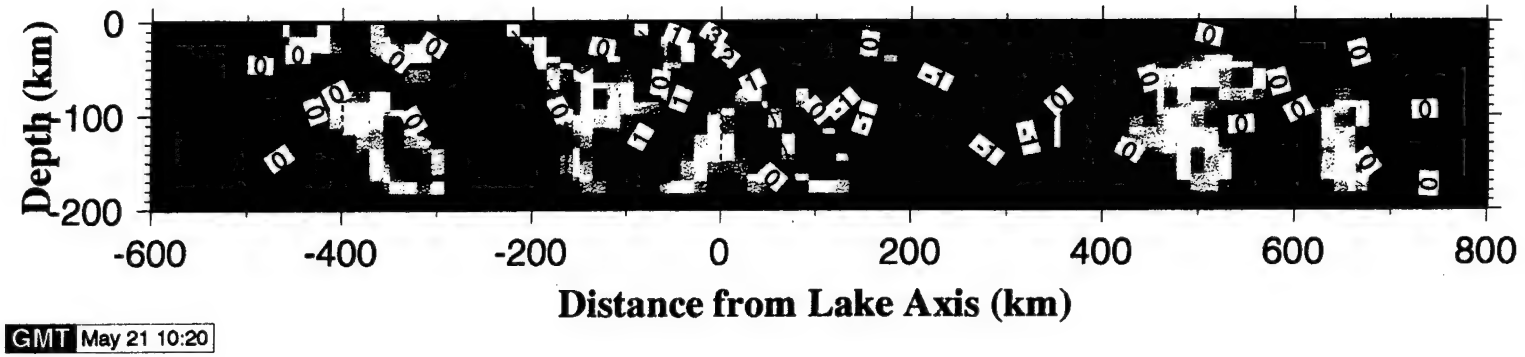

Figure 7.2

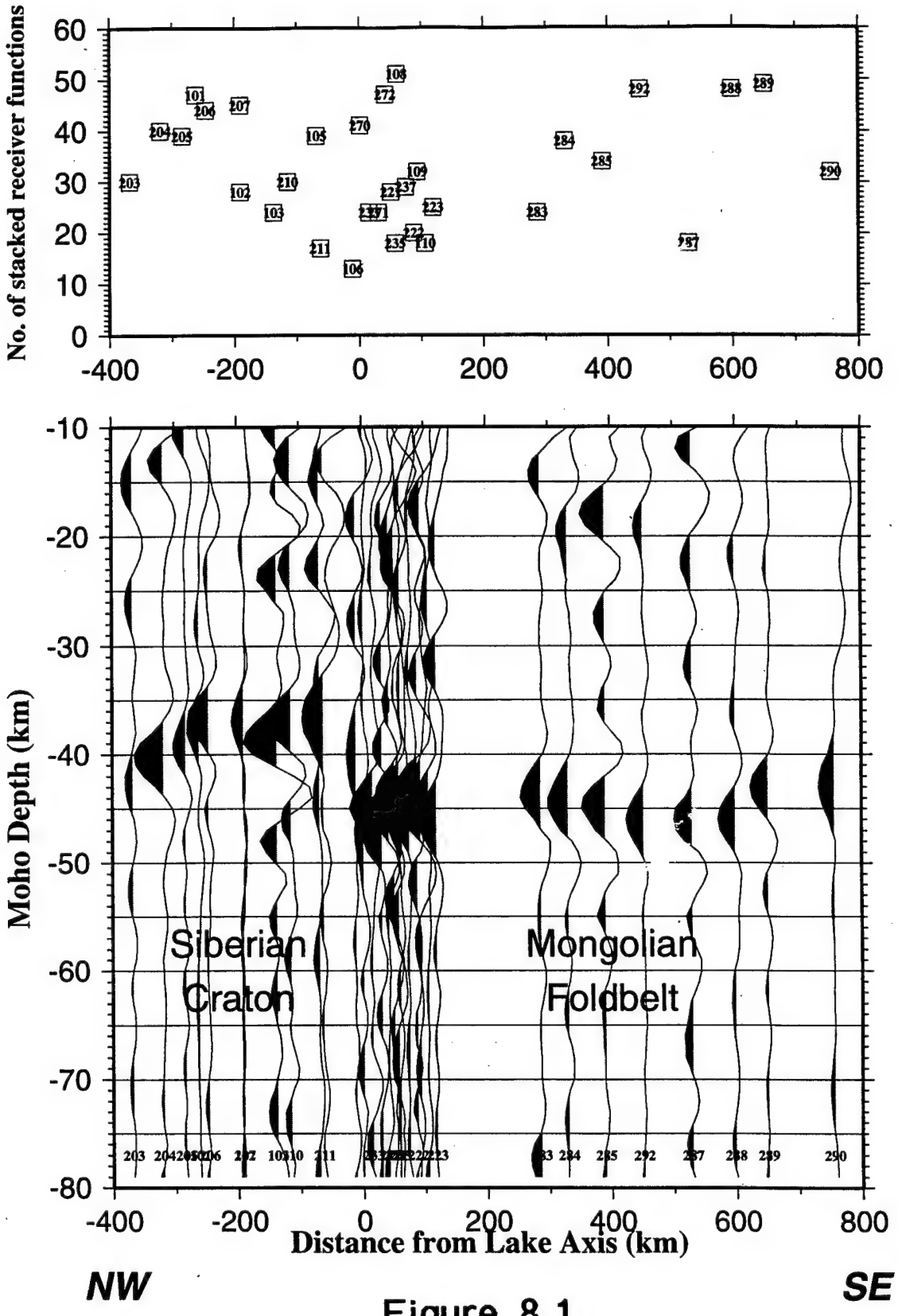
No. of stacked receiver functions
60
50
40
30
20
10
0
-400
-200
0
200
400
600
800
Moho Depth (km)
-10
-20
-30
-40
-50
-60
-70
-80
Siberian
Craton
Mongolian
Foldbelt
Distance from Lake Axis (km)
NW
SE

Figure 8.1

Table 2.1. Baikal 1991 Station Information

Station No.	Station Name	Coordinates		Ele. (m)	Duration	Sensor Type
		Lat	Lon			
01	Novoselova	53.620°N	102.645°E	550	07/12–10/02	L4C+Guralp
02	Suhoy-Zaglik	53.246°N	103.767°E	468	07/11–10/03	L4C
03	Kukunut	52.984°N	104.714°E	610	07/09–10/03	L4C
04	Turgenevka	53.034°N	105.648°E	820	07/08–10/05	L4C
05	Tyrgan	52.767°N	106.345°E	910	07/07–10/05	L4C+Guralp
06	Sakhoya	52.464°N	107.379°E	871	07/19–10/02	L4C+STS2
07	Solonechanyu	52.264°N	108.273°E	830	07/21–10/02	L4C+Guralp
08	Hasurta	52.207°N	109.078°E	810	07/22–10/02	L4C
09	Hovinsk	52.118°N	110.024°E	772	07/30–10/02	L4C
10	Uldurga	52.172°N	110.785°E	994	07/30–10/02	L4C+Guralp

Table 2.2. UCLA Baikal 1991 DAS Movement Chart

Station No.	Duration		DAS No.
	Start	End	
01	193:06	275:10	369
02	192:05	276:03	231
03	189:03	276:10	227
04	189:05	247:08	241
	252:10	267:05	084
	267:06	278:03	115
05	190:00	278:01	338
06	200:08	257:02	346
07	202:00	263:00	380
	263:08	276:00	241
08	203:08	275:08	388
09	210:01	275:04	378
10	211:12	230:22	084
	231:10	264:02	115
	264:03	275:05	380

Table 2.3. Baikal 1991 UCLA Reftek Station Recording Parameters

Data Stream Number	Sample Rate (sps)	Recording length (s)	Data Form (bits)	Stations
01	10	1800	16	ALL
02	50	180	16	ALL
03	1	3600	32	1,5,7,10

Table 2.4. Baikal 1992 Event Statistics

Group No.	Mag (mb)	Delta (deg)	Depth (km)	Number of (Events)	Comments
1	≥5.0	00-180	000-700	314	Medium & Strong events
2	≥5.5	00-180	000-700	54	Strong events
3	≥5.0	30-085	000-700	164	Tele-events with p as first arrivals
4	≥4.0	00-030	000-700	111	Significant regional & local events
5	≥5.0	00-180	100-700	82	Medium & strong deep events

Table 3.1. Baikal 1992 Station Information

Station No.	Station Name	Coordinates		Ele. (m)	Duration	Sensor Type
		Lat	Lon			
00	Bratsk	55.965°N	101.410°E	376	08/17–10/03	L4C+STS2
01	Pokosnoe	55.678°N	100.990°E	453	06/27–08/16	L4C+STS2
02	Naratay	55.052°N	101.850°E	346	06/25–07/21	S13
03	Ust-kada	54.516°N	102.070°E	433	06/23–10/01	L4C
04	Sborniy	54.193°N	102.649°E	624	06/22–10/01	S13
05	Konovalova	53.929°N	102.934°E	386	06/21–09/30	L4C
06	Melchituy	53.649°N	103.255°E	355	06/20–09/30	S13+Guralp
07	Suhoy-zaglik	53.243°N	103.767°E	719	06/18–09/29	L4C
08	Zacharovska	52.993°N	103.927°E	480	07/02–08/11	HS10
09	Baroy	52.778°N	104.105°E	518	06/17–07/17	L4C
10	Goryashina	52.622°N	104.234°E	524	06/14–09/29	HS10
11	Patrony	52.169°N	104.469°E	619	06/13–09/16	L4C+STS2
12	Listvyanka	51.847°N	104.893°E	600	06/11–10/05	S13
13	Naratay	55.022°N	102.055°E	388	07/21–10/01	S13
14	Stepanovka	52.854°N	103.966°E	619	07/17–09/29	L4C
15	Klyuchi-bulak	55.560°N	101.803°E	400	08/18–10/03	L22+Guralp
16	Patrony2	52.162°N	104.464°E	419	09/19–10/05	L4C+STS2
80	Suha-bator2	50.193°N	106.254°E	608	07/17–10/02	L4C+Guralp
81	Suha-bator	50.242°N	106.240°E	750	06/15–06/17	L22+STS2
82	Yoroo	49.738°N	106.202°E	682	06/16–07/17	S13
83	Sharingol	49.288°N	106.412°E	974	06/17–10/02	L4C
84	Hara	48.931°N	106.682°E	949	06/17–10/02	S13+Guralp
85	Tunhe	48.383°N	106.783°E	1122	06/21–10/01	L4C
86	Ulan-bator	47.921°N	106.954°E	1284	06/20–07/21	S13
87	Bayan-suma	47.209°N	107.422°E	1320	07/09–09/26	L22+Guralp
88	Sumber-suma	46.635°N	107.758°E	1265	07/10–09/26	S13
89	Bayan-argalan	46.115°N	107.619°E	1477	07/10–09/25	L4C
90	Endershil	45.262°N	108.260°E	1232	07/11–09/25	L22+STS2
91	Yoroo2	49.747°N	106.188°E	629	07/17–10/02	S13
92	Ulan-bator2	47.921°N	106.954°E	1284	07/21–09/28	S13

Table 3.2. UCLA Baikal 1992 DAS Movement Chart

Station No.	Duration		DAS No.
	Start	End	
00	230	276	119
01	179	229	119
02	177	203	373
03	175	275	376
04	174	275	395
05	173	274	099
06	172	274	369
07	170	273	378
08	184	200	345
09	169	199	363
10	166	273	347
11	165	260	359
12	163	260	367
	260	261	153
	261	266	359
13	203	275	373
14	199	273	363
15	231	276	342
16	263	273	367
80	199	276	147
81	167	168	239
82	168	199	152
83	169	276	361
84	169	276	339
85	173	275	388
86	172	203	346
87	191	270	374
88	192	270	231
89	192	269	154
90	193	269	341
91	199	276	152
92	203	272	346

Table 3.3. Baikal 1992 UCLA Reftek Station Recording Parameters

Data Stream Number	Sample Rate (sps)	Recording length (s)	Data Form (bits)	Stations
01	10	1800	16	ALL
02	25	180	16	STS2
	50	180	16	Guralp; short period
03	1	1800	32	Guralp; STS2

Table 3.4. Baikal 1992 Event Statistics

Group No.	Mag (mb)	Delta (deg)	Depth (km)	Number of (Events)	Comments
1	≥5.0	000-180	000-700	464	Medium & Strong events
2	≥5.5	000-180	000-700	113	Strong events
3	≥5.0	300-085	000-700	217	Tele-events with p as first arrivals
4	≥4.0	000-030	000-700	191	Significant regional & local events
5	≥5.0	000-180	100-700	81	Medium & strong deep events